



Terms and Conditions of Use of Digitised Theses from Trinity College Library Dublin

Copyright statement

All material supplied by Trinity College Library is protected by copyright (under the Copyright and Related Rights Act, 2000 as amended) and other relevant Intellectual Property Rights. By accessing and using a Digitised Thesis from Trinity College Library you acknowledge that all Intellectual Property Rights in any Works supplied are the sole and exclusive property of the copyright and/or other IPR holder. Specific copyright holders may not be explicitly identified. Use of materials from other sources within a thesis should not be construed as a claim over them.

A non-exclusive, non-transferable licence is hereby granted to those using or reproducing, in whole or in part, the material for valid purposes, providing the copyright owners are acknowledged using the normal conventions. Where specific permission to use material is required, this is identified and such permission must be sought from the copyright holder or agency cited.

Liability statement

By using a Digitised Thesis, I accept that Trinity College Dublin bears no legal responsibility for the accuracy, legality or comprehensiveness of materials contained within the thesis, and that Trinity College Dublin accepts no liability for indirect, consequential, or incidental, damages or losses arising from use of the thesis for whatever reason. Information located in a thesis may be subject to specific use constraints, details of which may not be explicitly described. It is the responsibility of potential and actual users to be aware of such constraints and to abide by them. By making use of material from a digitised thesis, you accept these copyright and disclaimer provisions. Where it is brought to the attention of Trinity College Library that there may be a breach of copyright or other restraint, it is the policy to withdraw or take down access to a thesis while the issue is being resolved.

Access Agreement

By using a Digitised Thesis from Trinity College Library you are bound by the following Terms & Conditions. Please read them carefully.

I have read and I understand the following statement: All material supplied via a Digitised Thesis from Trinity College Library is protected by copyright and other intellectual property rights, and duplication or sale of all or part of any of a thesis is not permitted, except that material may be duplicated by you for your research use or for educational purposes in electronic or print form providing the copyright owners are acknowledged using the normal conventions. You must obtain permission for any other use. Electronic or print copies may not be offered, whether for sale or otherwise to anyone. This copy has been supplied on the understanding that it is copyright material and that no quotation from the thesis may be published without proper acknowledgement.

THE INFLUENCE OF CHEVRONS ON
THE TURBULENT CHARACTERISTICS
OF JETS

JOHN KENNEDY

Department of Mechanical & Manufacturing Engineering

Parsons Building

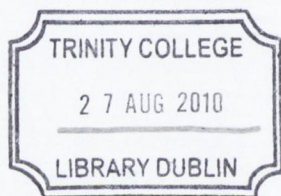
Trinity College

Dublin 2

Ireland

April 2010

A thesis submitted to the University of Dublin in partial
fulfillment of the requirements for the degree of Ph.D.



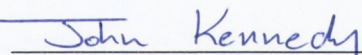
THEOIS.
8930

Handwritten text in cursive script, consisting of two lines: "THEOIS." and "8930".

Declaration

I declare that I am the author of this thesis and that all work described herein is my own, unless otherwise referenced. Furthermore, this work has not been submitted, in whole or part, to any other university or college for any degree or qualification.

I authorize the library of Trinity College, Dublin to lend or copy this thesis.



John Kennedy, April 2010

Declaration

I, the undersigned, do hereby declare that the information provided in this document is true and correct to the best of my knowledge and belief.

Signature: _____
Date: _____

Abstract

To minimize the significant environmental impact of air travel a reduction in noise pollution from jet engines is required. This has led to a renewed focus on active and passive techniques which modify the turbulence characteristics and hence the noise production mechanisms in the jet. One of the most prominent technologies of this type about to be implemented on commercial aircraft are chevron nozzles. It has been shown that this technology can provide noise reductions without significant thrust penalties. However chevron nozzles suffer from a high frequency noise penalty that has been attributed to increased mixing in the near nozzle region. Current noise prediction methods can not handle the complex changes to the turbulence properties of the jet. While the effects on the far field sound and on the jet structure have been well documented more fundamental research is required on how chevrons affect the turbulence properties in order to improve the current noise prediction capabilities.

A detailed investigation has been carried out comparing three chevron nozzles to a baseline single jet in which extensive measurements have been performed to determine the turbulent characteristics of the flows. The investigation is primarily concerned with the affects of chevron immersion on the flow.

A whole flow field investigation has been under taken using PIV to examine the effects of the chevrons on both jet structure and the basic turbulence properties. In terms of jet structure the primary quantities of interest are potential core length and shear layer growth. It was found that chevron nozzles significantly alter the growth of the shear layer and the ratio of the turbulence components. In addition chevron immersion was identified as the significant factor in altering the potential core length.

A more intensive investigation of the turbulent length scales was then undertaken.

Two point, two component LDA and cross hot wire measurements were taken to determine the length scales associated with both the turbulence and shear stresses for the different configurations. These statistics are directly related to the noise source mechanisms and are used in the principle noise source models.

Through the use of frequency dependent length scales this investigation has clearly shown that the different scales of the turbulence respond very differently to the addition of chevrons to a nozzle. This has clearly demonstrated that without the use of a frequency dependent length scale no model is capable of capturing the altered flow properties produced by chevrons. It is suggested that any model wishing to capture the physics of the noise production must now include frequency dependent length and time scales.

Acknowledgments

I would like to thank my supervisor, Professor John Fitzpatrick, for his help and guidance over the course of this project. He kept me focused while also providing the freedom to create and explore. In addition I'd like to thank the other academic staff and researchers that I've had the pleasure of working with over the past three years in particular Dr. Franck Keherve, Dr. Gareth Bennett and Dr. Craig Meskell.

I have received enormous help from the administrative and technical staff of the department. In particular I would like to thank Mick Reilly, Joan Gillen, Gerry Byrne and JJ Ryan for the assistance and time they have freely given over the course of this research.

To my colleagues and friends in the fluids lab who have made the last three years more enjoyable than I could have hoped for. In particular John, Shane, Cathal, Eoin, Steve and Ciaran for their help and insight throughout this research.

To my family who have provided constant support and encouragement over the years. Without all of you I would not have made it to where I am today.

To Jen, your patience and encouragement have helped me from beginning to end of this work and it was completed, in no small way, due to your help.

Contents

1	Introduction	1
1.1	Objectives and Overview	2
2	Turbulence and Aeroacoustics	5
2.1	Turbulence	5
2.2	Computational Fluid Dynamics	8
2.2.1	Reynolds Averaged Navier Stokes	8
2.2.2	Large Eddy Simulation	9
2.3	Computational Aero-Acoustics	9
2.3.1	The Acoustic Analogy	9
2.3.2	The Tam-Auriault Model	11
2.4	The Turbulent Jet	12
3	Turbulence Statistics	15
3.1	Spatial and Temporal Correlations	16
3.2	Frequency Dependent Statistics	20
4	Noise Reduction Technologies	29
4.1	Chevron Nozzles	30
4.2	Summary	34
5	Experimental Facilities and Instrumentation	37
5.1	Small Scale Jet Rig	37
5.2	Nozzle Designs	38
5.3	Seeding Particle Generation	40

CONTENTS

5.4	Particle Image Velocimetry	40
5.5	Laser Doppler Anemometry	42
5.6	Constant Temperature Anemometry	43
5.6.1	Hot Wire Probe Calibration	45
5.7	Data Acquisition and Error Analysis	47
5.7.1	PIV	47
5.7.2	LDA	50
5.7.3	X-Wire	52
5.7.4	DAQ System	54
5.7.5	Test Matrix	54
6	Nozzle Characterisation	57
6.1	Jet Structure	57
6.2	Turbulence Properties	64
6.2.1	Ratio of Radial to Axial Turbulence Intensity	68
6.2.2	Reynolds Stresses	70
6.3	Discussion	77
7	Two Point Statistics	79
7.1	Bulk Length Scales	80
7.1.1	u' and v' Length Scales	80
7.1.2	u'^2 and v'^2 Length Scales	83
7.1.3	$u'v'$ Length Scales	85
7.2	Frequency Dependent Length Scales	87
7.2.1	u' Moving Axis Length Scale	87
7.2.2	v' Moving Axis Length Scale	91
7.2.3	u'^2 Moving Axis Length Scale	95
7.2.4	v'^2 Moving Axis Length Scales	99
7.2.5	$u'v'$ Moving Axis Length Scale	103
7.2.6	u' Fixed Axis Length Scale	107
7.2.7	v' Fixed Axis Length Scale	111
7.2.8	u'^2 Fixed Axis Length Scale	115

7.2.9	v'^2 Fixed Axis Length Scale	119
7.2.10	$u'v'$ Fixed Axis Length Scale	123
7.3	Comparison of u' and v' Length Scales	127
7.4	Local Strouhal Number	130
7.5	Discussion	134
8	Implications for Noise Source Modeling	139
8.1	Future Work	143
A	Frequency Dependent Length Scales $75\%L_c$	151

CONTENTS

List of Figures

2.1	Structure of a Jet	12
3.1	Spatial and Temporal Statistics u' Baseline Nozzle $0.5lc$	19
3.2	Example Curve Shapes for Fixed and Moving Axis Length Scales	22
3.3	Frequency Dependent Moving Axis Length Scale u' Baseline Nozzle $0.5lc$	23
3.4	Frequency Dependent Fixed Axis Length Scale u' Baseline Nozzle $0.5lc$	24
3.5	Cross Coherence Function Phase	26
3.6	Frequency Dependent Convection Speeds	27
4.1	NASA Nozzle Designs	32
4.2	Boeing 777-300ER with Chevron Nozzle	33
5.1	Subsonic Open Jet Facility and Nozzle Close Up	38
5.2	Four Degree Chevron Nozzle Profile and Model	39
5.3	PIV Experimental Setup	41
5.4	PIV Calculation Example	42
5.5	LDA Experimental Setup	43
5.6	Dantec Dynamics Hot Wire System	44
5.7	Calibration Facility	45
5.8	Dantec Dynamics 55P61 X-WireProbe	46
5.9	Calibration Map Dantec 55P61 X-Wire Probe	47
5.10	Pixel Displacement Histograms (a) Peak Locking Example (b) Measurement Example	49
5.11	LDA and Hot Wire Signals	52
5.12	Comparision of LDA and Hot Wire Spectra Baseline Nozzle $0.5lc$	53

LIST OF FIGURES

6.1	Measurement Positions	58
6.2	\bar{u}/u_j Profiles 1 – 8D	60
6.3	Momentum Integral Thickness θ/D	62
6.4	Hot Wire Spectra	63
6.5	u'/u_j Tip and Trough Regions	65
6.6	v'/u_j Tip and Trough Regions	66
6.7	u'/u_j Profiles 1 – 8D	67
6.8	v'/u_j Profiles 1 – 8D	67
6.9	Ratio of Radial to Axial Turbulence Intensities v'/u'	69
6.10	u'^2/u_j^2 Profiles 1 – 8D	71
6.11	v'^2/u_j^2 Profiles 1 – 8D	71
6.12	Ratio of Reynolds Stresses v'^2/u'^2	72
6.13	$u'v'/u_j^2$ Profiles 1 – 8D	73
6.14	Ratio of Reynolds Stresses $u'v'/u'^2$	75
6.15	Vorticity Tip Regions	76
6.16	Vorticity Trough Regions	76
7.1	Two Point Measurement Positions Baseline Nozzle	80
7.2	Frequency Dependent Moving Axis Length Scale u' 50% L_c	89
7.3	Frequency Dependent Moving Axis Length Scale u' 100% L_c	90
7.4	Frequency Dependent Moving Axis Length Scale v' 50% L_c	93
7.5	Frequency Dependent Moving Axis Length Scale v' 100% L_c	94
7.6	Frequency Dependent Moving Axis Length Scale u'^2 50% L_c	97
7.7	Frequency Dependent Moving Axis Length Scale u'^2 100% L_c	98
7.8	Frequency Dependent Moving Axis Length Scale v'^2 50% L_c	101
7.9	Frequency Dependent Moving Axis Length Scale v'^2 100% L_c	102
7.10	Frequency Dependent Moving Axis Length Scale $u'v'$ 50% L_c	105
7.11	Frequency Dependent Moving Axis Length Scale $u'v'$ 100% L_c	106
7.12	Frequency Dependent Fixed Axis Length Scale u' 50% L_c	109
7.13	Frequency Dependent Fixed Axis Length Scale u' 100% L_c	110
7.14	Frequency Dependent Fixed Axis Length Scale v' 50% L_c	113

7.15 Frequency Dependent Fixed Axis Length Scale v' 100% L_c	114
7.16 Frequency Dependent Fixed Axis Length Scale u'^2 50% L_c	117
7.17 Frequency Dependent Fixed Axis Length Scale u'^2 100% L_c	118
7.18 Frequency Dependent Fixed Axis Length Scale v'^2 50% L_c	121
7.19 Frequency Dependent Fixed Axis Length Scale v'^2 100% L_c	122
7.20 Frequency Dependent Fixed Axis Length Scale $u'v'$ 50% L_c	125
7.21 Frequency Dependent Fixed Axis Length Scale $u'v'$ 100% L_c	126
7.22 Moving Axis Length Scale u' to v' Comparison: Single Jet	128
7.23 Moving Axis Length Scale u' to v' Comparison: 0° Nozzle	129
7.24 Fixed Axis Frequency Dependent Length Scale: Local Strouhal Number	132
7.25 Moving Axis Frequency Dependent Length Scale: Local Strouhal Number	133
A.1 Frequency Dependent Moving Axis Length Scale u' 75% L_c	152
A.2 Frequency Dependent Moving Axis Length Scale v' 75% L_c	153
A.3 Frequency Dependent Moving Axis Length Scale u'^2 75% L_c	154
A.4 Frequency Dependent Moving Axis Length Scale v'^2 75% L_c	155
A.5 Frequency Dependent Moving Axis Length Scale $u'v'$ 75% L_c	156
A.6 Frequency Dependent Fixed Axis Length Scale u' 75% L_c	157
A.7 Frequency Dependent Fixed Axis Length Scale v' 75% L_c	158
A.8 Frequency Dependent Fixed Axis Length Scale u'^2 75% L_c	159
A.9 Frequency Dependent Fixed Axis Length Scale v'^2 75% L_c	160
A.10 Frequency Dependent Fixed Axis Length Scale $u'v'$ 75% L_c	161

LIST OF FIGURES

List of Tables

5.1	Nozzle Parameters	39
5.2	PIV Test Matrix	55
5.3	LDA and X-wire Test Matrix	55
6.1	Nozzle Configurations	59
6.2	Potential Core Length	59
7.1	u' and v' Length Scales and Convection Speed $0.5L_c$	82
7.2	u' and v' Length Scales and Convection Speed $0.75L_c$	82
7.3	u' and v' Length Scales and Convection Speed $1.0L_c$	82
7.4	u'^2 and v'^2 Length Scales and Convection Speed $0.5L_c$	84
7.5	u'^2 and v'^2 Length Scales and Convection Speed $0.75L_c$	84
7.6	u'^2 and v'^2 Length Scales and Convection Speed $1.0L_c$	84
7.7	$u'v'$ Length Scales and Convection Speed $0.5L_c$	86
7.8	$u'v'$ Length Scales and Convection Speed $0.75L_c$	86
7.9	$u'v'$ Length Scales and Convection Speed $1.0L_c$	86
8.1	Nozzle Parameters	140

Chapter 1

Introduction

The commercial airline industry is today one of the largest global industries and one that effects many aspects of daily life. The airline industry has a significant environmental impact and a key element of this is jet noise. Many airports have now expanded into residential areas which has led to the introduction of strict legislation regarding noise pollution. In order to meet these challenges the airline industry has placed a huge demand on research to provide efficient noise reduction technologies. As a result the field of aeroacoustics is today perhaps more vibrant than ever and consists equally of experimental, theoretical and numerical research.

Many of the key revolutions in jet noise research began with Lighthill's work in the 1950s which opened the door to understanding how a turbulent flow produces noise for the first time. From here advances in measurement technologies led to detailed experimental studies through the 1970s and 80s. This work produced massive empirical databases from which predictions of jet noise could be drawn. Combined with the revolution in computing power through the 1990s these empirical databases were used to provide fast rough and ready predictions of aircraft noise. This led to the birth of Computation Aero-Acoustics (CAA) and a vast amount of research time is still spent developing these prediction technologies. Many jet noise prediction codes still rely on the original empirical data provided by the earlier research to validate their results. Many of the most successful prediction codes still rely heavily on empirical constants to correct or normalize their results. It is not sufficient to rely on empirical

data to provide an accurate answer for jet noise prediction and a true understanding of the physics of the problem is required. We now have the computational power and prediction methodologies available to begin including more of the real physics of the problem of jet noise in the prediction codes.

Perhaps the strongest reason to move away from empirically based prediction techniques is the increasing complexity of jet engine design. Many of the most recent noise reduction technologies rely on changing the fundamental flow structure of the jet. Two of the most prominent technologies of this type to emerge from new research are chevrons and microjets. The latest designs for these technologies can provide significant noise reductions without significant thrust penalties [1]. However since the fundamental physics of the flow have been changed evidence is emerging that the traditional scaling laws probably no longer apply [2]. The airline industry has come to rely heavily on computer prediction technologies as an alternative to expensive wind tunnel testing. Now that these noise reduction technologies are being realised on commercial aircraft designs the challenge will be to update our prediction capabilities to handle the new physics.

This is particularly relevant since this year, 2009, will see the release of the first commercial aircraft to feature chevrons as a noise reduction technology: the Boeing 787 Dreamliner. This aircraft has been designed with the pressures of fuel economy and environmental impact in mind and these factors will continue to be a driving force in design for some time to come.

1.1 Objectives and Overview

The purpose of this investigation is to provide a parametric study of the effects of chevron geometries on flow physics. Keeping the requirements of noise prediction technologies in mind this study had a number of objectives:

- To design a series of chevron nozzle geometries that represent the action of full scale aircraft designs. This is achieved through the design of a parametric series of nozzles focused on the feature of chevron immersion into the flow.

- To quantify the changes in flow structure resulting from the addition of chevrons to nozzle designs. This is achieved by a full flow field comparison with a baseline nozzle. In addition this process identified areas of interest for further tests.
- To provide in depth turbulence statistics of the type used for aeroacoustic prediction codes. This is achieved through two point measurements of the frequency dependent turbulence properties and Reynolds stresses.
- To examine the change in the turbulence properties with a view to explaining the changes in jet noise produced by chevron designs.

The contents of this thesis are organized as follows. Chapter 2 outlines the difficulties turbulence presents the researcher and gives a brief outline of the main theories used to predict the noise it generates.

Chapter 3 describes the theory required for calculating turbulence statistics and their frequency dependence.

Chapter 4 gives an overview of the research into the effects of chevron nozzles as a noise reduction technology and describes the state of the art technology soon to be found on commercial aircraft.

Chapter 5 describes the experimental facilities and instrumentation used for this investigation and quantifies the experimental error associated with such techniques.

The results of the preliminary PIV investigation are given in chapter 6 and are used to characterize the chevron nozzles and their changes from a baseline single jet.

The results for the turbulence statistics and their frequency dependence are given in chapter 7 with a discussion of the general effects of chevrons and their immersion into the flow.

Finally a discussion of the implications for noise source modeling and the requirements for future research are discussed in chapter 8.

Chapter 2

Turbulence and Aeroacoustics

2.1 Turbulence

The study of turbulence is often described as the study of the last unsolved problem in classical mechanics. Research into this topic has been ongoing throughout the last century but the basic mechanisms involved in a turbulent flow and in particular governing noise production are still not understood. The complex nature of the problem has been well known since the beginning of aeroacoustic research and the principle difficulties are summarized well by Batchelor [3]. He identified the three main obstacles faced by the researcher as

- The three dimensional character of the velocity field
- The non-linearity of the equation of motion
- The random variation of the velocity and the need for statistical methods

From an experimental point of view the three dimensional nature of the turbulent field is a large obstacle to gathering sufficient data to quantify the flow. The availability of non-intrusive three component measurement technology is a very recent development and even today few researchers have access to such equipment. As a result our insights into the structure of turbulence have for the most part been limited to measurements of a single variable in one or two spatial dimensions at a single point

in space. It has required decades of research to build up sufficient empirical data to test theories and to propose modifications where appropriate.

The non-linearity of the governing equations has hampered research as often gross simplifications of the equations are required before they can be solved. The validity of the assumptions involved needs to be tested and while simplified equations will often give rough-and-ready answers on the nature of turbulence they also often remove elements essential to the physics of the problem. In a problem as complex as turbulence it may be the case that any simplification of the governing equations impedes an accurate understanding of the problem. It is only with recent developments in computational power that full solutions of the governing equations for simple problems have become possible. As technology develops over the coming decade this ability will spread to cover increasingly complex turbulent flows and will hopefully provide further insights to aid our understanding of how a turbulent flow produces noise.

The random nature of the turbulence is a particular difficulty for all elements of turbulent research including theoretical, numerical and experimental research. While it is impossible to predict what value a turbulent fluctuation will take at any given moment it was accepted very early in the research that the average values for a particular location in the flow should remain constant. While this view of turbulence as a stationary continuous process allowed for much easier analysis of the problem it is possible that not all scales of the turbulence can be viewed in this manner. The identification of intermittent large scale structures in turbulence posed difficulties for any analysis technique that relies on time averaging. In addition it may be difficult to justify classifying the formation and decay of these large scale structures as a stationary process. However the statistical properties of turbulence have provided great insight into the nature of turbulent flows and proven to be vital in predicting the noise they produce.

Beyond the initial problem of defining and measuring turbulent motion there exists the equally difficult task of understanding how such flows produce noise. Any air flow will produce pressure fluctuations either in the form of regular eddies or an irregular turbulent flow. These pressure fluctuations can be detected and measured by a microphone or the human ear; however only a relatively small proportion of the

energy of these fluctuations actually propagates away from the disturbance as what can accurately be called sound. Most of the pressure fluctuations, for example eddies, are transported in the flow at the flow speed and do not propagate at the typical sound speed for the medium. These hydrodynamic pressure fluctuations transfer a certain amount of their kinetic energy into radiated sound. An examination of the radiated sound field reveals that it is comprised of a continuous frequency spectrum and therefore all scales of the turbulent pressure fluctuations must be producing some propagating sound. However the large and small scales of the turbulence may behave very differently and the exact mechanisms through which sound is generated by these fluctuations are not understood.

Identifying the factors that make a particular turbulent structure an efficient producer of sound has always been a key aim of research. It is logical to assume that this understanding would lead to improvements in noise reduction technologies as this would allow a clear aim for modifying the flow to be stated for the first time. To further complicate the problem there is the possibility of this radiated sound field having an effect on the flow field that produced it. For most purposes this feedback effect of the radiated sound is deemed negligible and is therefore ignored. However there has been research that sound can strongly affect flows in air ducts and boundary layers [4]. Also in the case of supersonic jets that produce a strong screech Lighthill [5] himself stated that the reaction on the flow could no longer be ignored. So while it is convenient to ignore these effects for normal jets they may prove important as even a small change in the turbulence may affect how efficiently it generates sound.

In summary the problem of predicting how turbulent flows produce sound is extremely complex and requires highly detailed and accurate analysis techniques. The dramatic increase in computational power available to researchers in the last two decades has produced important new research tools. These computer modeling and prediction tools can provide the entire flow field and all relevant variables required to solve the problem of turbulent noise production. An important role of experiments is now to validate these new tools and confirm that their predictions are reflected in the real life physics of the problem. Furthermore experiments should be designed so that they can feed new information into these computer codes to improve their prediction

capabilities. It was with this aim in mind that this investigation was undertaken and a review of the relevant computer prediction technologies will now be given. The challenge will be to incorporate the experimental results of this investigation into these technologies to improve their capabilities.

2.2 Computational Fluid Dynamics

2.2.1 Reynolds Averaged Navier Stokes

The most widely used numerical simulations of turbulence in industry are based on a Reynolds Averaged Navier Stokes (RANS) solver. These are perhaps the least computationally expensive to run and therefore provide the fastest solutions; often being run on standard desktop PCs. The governing equations are time averaged to get their steady form. As a result all variables consist of a steady, time independent average value and a modeled fluctuating value.

This means that all scales of the turbulence are modeled in RANS. These turbulence models have been developed from vast empirical databases of turbulent measurements over decades of research. However the advent of new noise reduction technologies that rely on changing the flow structure and turbulent statistics means there is increasing evidence that these models may no longer be valid [2]. Despite this RANS often provides a starting point for further computations, in particular computational aeroacoustics [6]. Rough answers for local turbulent kinetic energy and the length and time scales can be calculated relatively quickly and then used in further modeling of the turbulence for other applications.

Even with the most advanced turbulence models RANS is inherently unsuitable for many problems, in particular flows with large unsteady turbulent structures which can not be time averaged. Turbulent jets consist of these large scale structures so a more comprehensive computational technique is required for accurate results.

2.2.2 Large Eddy Simulation

With the increased computational power available in modern super computers and computer clusters another technique for turbulence simulation has emerged; large eddy simulation (LES). In this technique the equations are not time averaged so unsteady turbulent fluctuations can still be calculated however a detailed LES can take several months to simulate even a few seconds of real time flow. The basis of this technique is to volume average filter the Navier Stokes equations. This divides the equations into large scale structures that can be directly calculated and small scale structures that can be modeled. The premise being that the small scale structures are more isotropic and homogeneous and so are more conducive to being modeled accurately. By calculating the large structures of the flow more of the real physics of the flow are retained. In essence LES approaches a direct numerical solution of the governing equations for the larger scales. The choice of where to stop calculating and start modeling is left to the researcher and is usually in the inertial sub range. A finer computational grid will allow for smaller scales of the turbulence to be resolved accurately but unfortunately fine 3D meshing of the problem leads to a dramatic increase in computational time over the coarse 2D RANS solutions. Despite this LES simulations are increasingly being used as the starting point for aeroacoustic predictions [7].

2.3 Computational Aero-Acoustics

2.3.1 The Acoustic Analogy

By far the greatest single advancement in the history of aeroacoustics was the development of the acoustic analogy by Lighthill. This work was released in two papers in the early 1950s [8] [9]. It was groundbreaking research as it allowed acoustic predictions of turbulent flow to be made for the first time. A brief overview of the main theory as outlined in Lighthills original papers will be discussed here. Lighthill began by considering a fluctuating fluid flow occupying a small part of very large body of fluid at rest. He then related the equations governing the fluctuations of density in the fluid to those governing a uniform acoustic medium at rest. This produced an equation

expressing the momentum contained in a small fixed region of space. This equation relates the rate change of momentum to the stress acting at the boundaries and the flow across the boundaries of momentum bearing fluid. Comparing these real stresses with the stress found in an acoustic medium produced the equation below

$$T_{ij} = \rho u_i u_j + [(p - p_0) - c_0^2(\rho - \rho_0)]\delta_{ij} + \sigma_{ij} \quad (2.1)$$

where c_0 is the ambient speed of sound, p and ρ are the absolute local pressure and density, the ambient pressure and density are given by p_0 and ρ_0 , δ_{ij} is a delta function, σ_{ij} is the viscous stress tensor and the subscripts i and j are summation notation. The external stress system T_{ij} incorporates sound generation, convection with the flow, propagation with variable speed and dissipation by conduction and viscosity [8]. This is all of the relevant information required for aeroacoustic predictions and the equation required no approximations to be made in order to achieve this form. At this point assumptions can be made about the relative importance of the terms. The dissipation by viscosity is a very slow process and is assumed unimportant for most problems. It can also be said that the pressure fields are unimportant in problems which are of fairly uniform temperature. The essential piece of information gained is therefore that the Reynolds stresses, $\rho u_i u_j$, are the principle generators of sound.

This equation now shows the relationship converting the kinetic energy of fluctuating shearing motions into acoustic energy of fluctuating longitudinal motions [8]. The next step is to rewrite the equations of fluid motion in light of these observations

$$\frac{\delta^2 \rho'}{\delta t^2} - c_0^2 \nabla^2 \rho' = \frac{\delta^2 T_{ij}}{\delta x_i \delta x_j} \quad (2.2)$$

where ρ' is the acoustic density fluctuation. These are the basic equations used in the theory to define the Lighthill source terms. Physically these state that a fluctuating flow in a limited region of space at rest produces the same density fluctuations as those of a stationary acoustic medium under a system of externally applied stress [5].

Developing these equations to provide the Lighthill source term produces the need for a two point correlation of the velocity and density fluctuation in all three spatial dimensions. Modeling this correlation tensor accurately has been the subject of much

research. A popular model based on assumptions of homogeneous isotropic turbulence was proposed by Ribner [10] and this model predicts the far field spectral density of the noise to be given by the equation below

$$dS(x, x_s, \omega) = \frac{\omega^4 l_t^3 \tau_t \bar{\rho}^2 \bar{u}_t^2}{128\pi^3 c_0^4 r^2} \exp\left(-\frac{\omega^2}{8\pi} \left(C^2 \tau_t^2 + \frac{l_t^2}{c_0^2}\right)\right) dV \quad (2.3)$$

where dV is the volume of the element and the total spectral density can be obtained by integrating over the jet volume. The turbulence statistics required for this model are l_t the length scale, τ_t the time scale and \bar{u}_t^2 the isotropic turbulence kinetic energy.

The essential point to note from acoustic analogy type predictions is that sound is produced by quadrupoles with strength related to the two point correlation function of the Reynolds stresses. The difficulty now lies in calculating the Reynolds stress terms as experiments can generally only acquire two point velocity measurements in two spatial dimensions leaving the requirement to model the third velocity component and density fluctuations. This is where statistical modeling of turbulence is required. Therefore it is necessary to have detailed turbulence statistics including the length scales in order to perform an acoustic analogy prediction. This is the starting point for many computational aeroacoustics predictions which use a RANS calculation and statistical modeling to provide this information.

2.3.2 The Tam-Auriault Model

While there have been many modifications to Lighthill's original acoustic analogy there have also been several new theories that attempt to solve the problem from a different starting point. The most popular of these more recent models was proposed by Tam and Auriault [11]. This theory uses the kinetic theory of gases as a starting point to relate the local turbulent kinetic energy to the local pressure fluctuations of the small scale turbulence. The theory was developed using turbulence statistics supplied from a $k - \epsilon$ turbulence model which was itself developed from empirical data. As such the original theory is also semi-empirical. This theory deals with the noise produced from the fine scale turbulence and not that produced by the large scale structures. The far

field spectral density is given integrating the equation below over the volume of the jet

$$ds(x, x_s, \omega) = \frac{\omega^2}{16\pi^3 c_0^4 r^2} \left(\frac{\pi}{\ln 2} \right) \frac{q_t^2 l_t^2}{\tau_t} \frac{\exp\left(\frac{2l_t^2}{u_1^2 (4\ln 2)}\right)}{1 + 2 \tau_t^2 \left(1 - \frac{u_1}{c_0} \cos\theta\right)^2} dV \quad (2.4)$$

Similarly to the acoustic analogy the integral length scale l_t and the integral time scale τ_t are required as is the turbulent kinetic energy q_t^2 . All of these quantities can be supplied by a RANS calculation and so this theory is also easily applied at low computational cost. However the length and time scales and kinetic energy are modeled for both methods and this is significant for noise reduction technologies that significantly alter the nature of these statistics.

2.4 The Turbulent Jet

A jet is a flow consisting of the continuous addition of fluid into a surrounding stationary medium. The interaction between the flow and the surrounding medium leads to intense mixing and the creation of a shear layer. As the flow extends further from the jet exit the shear layer widens and eventually the inner core of the jet, which maintains the original velocity of the flow, dissipates and a fully developed mixing region exists. The basic structure of the jet is shown in figure 2.1.

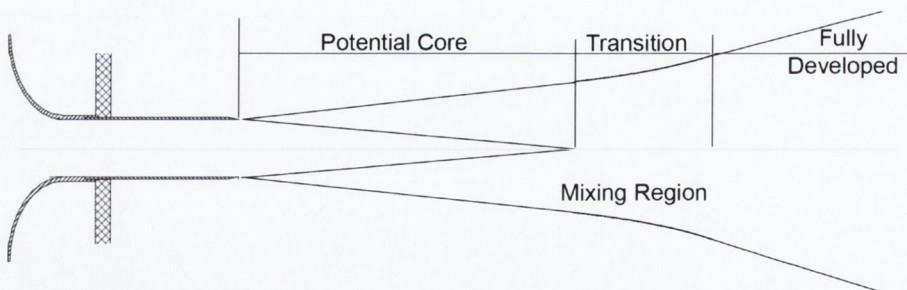


Figure 2.1: Structure of a Jet

There are several regions of interest in the jet structure and while some consensus exists over which are most relevant for noise production there still exists a lot of uncertainty. The original work in jet noise focused on the fine turbulence scales as these were believed to be the source of the jet noise. However during the 1970s large

scale turbulent structures were discovered in the shear layer and the focus shifted to how these could generate noise. It was shown by Juvé [12] that these structures displayed significant intermittency and he demonstrated that 50% of their noise was produced in only 10 – 20% of the time. Juvé also suggested that noise emission would take place upstream of these structures as non-turbulent fluid was rapidly entrained. The breakdown of these structures at the end of the potential core is also believed to be a significant source of noise.

In order to shed more light on the noise producing regions of a jet numerous attempts have been made to correlate point measurements of velocity with near and far field acoustic measurements. This approach was taken by the likes of Schaffar [13] [14] when large scale structures were first discovered and is still applied today with modern measurement techniques by many researchers such as Panda [15]. However the process of relating a point velocity measurement to a far field microphone measurement is far from trivial. A microphone measurement will record all of the sound radiated by a jet and the emissions of a single point, regardless of how significant that point is in relation to the overall sound field, can be lost in the rest of the noise.

The use of microphone arrays allows more advanced techniques such as beam forming to be used. This technique uses the overlapping signals of several microphones to focus in on a specific region of space and has been applied successfully to propeller noise [16] and jet noise [17]. This technique allows the important noise producing regions of the flow to be identified. However there are other issues which affect how sound radiates out from a source in a jet. Most noise producing phenomena are carried in the jet at a relatively high speed; this convection of the source has a strong affect on the directivity of the noise radiated. It can be shown that this leads to increased radiation in the direction the source is being carried. Furthermore in order for the radiated sound to reach the far field it must pass through the shear layer which results in refraction effects [18]. These result from the velocity and temperature gradients that exist in the shear layer.

Since the discovery of the larger scale structures in turbulence there has been much debate as to which turbulent scales are most significant for noise production. The spectral content of the noise differs at different angles to the jet axis and researchers

focus on the radiated sound at 30° and 90° . The different spectral content of the noise at these angles has led some researchers to propose that two different mechanisms are responsible. Tam [11] has proposed that the fine scale turbulence is responsible for noise at 90° to the jet axis while the large scale structures are responsible for the noise at 30° . Other researchers still support the earlier view proposed by the likes of Ffowcs Williams [19] that the difference in spectral content can be explained by the directivity of the source without the need for two separate mechanisms.

Chapter 3

Turbulence Statistics

It is usual to picture turbulence as random fluctuations superimposed on a mean flow. This breaking of the velocity signal u into a mean and fluctuating part is given by the equations below and this process can be applied to the three components of velocity.

$$\begin{aligned}u(t) &= \bar{u} + u'(t) \\ \bar{u} &= \frac{1}{2T} \int_{-T}^T u(t) dt\end{aligned}\tag{3.1}$$

For a jet flow turbulence in the three spatial directions is given by the equations below with $u(t)$ along the axis of the jet, $v(t)$ in the radial direction and $w(t)$ the azimuthal direction. Any mean flow in the radial or azimuthal directions will be due to entrainment of the surrounding fluid into the jet.

$$\begin{aligned}u(t) &= \bar{u} + u'(t) \\ v(t) &= \bar{v} + v'(t) \\ w(t) &= \bar{w} + w'(t)\end{aligned}\tag{3.2}$$

The mean square values and cross products of these fluctuating turbulence components are also important as these represent the Reynolds stresses which have been shown to be important in noise production. These are the basic statistics used to quantify turbulence.

3.1 Spatial and Temporal Correlations

Turbulence is often described in terms of its spatial and temporal statistics namely the length scale, time scale and convection speed. By calculating a length scale in each of the three spatial dimensions a volume of fluid is defined. This volume is a measure of the average spatial extent of the turbulent structures at that location in the flow [3]. In addition the time scales and convection velocity give an indication of the speed of the average vortex in the flow and its rate of decay. In general only one or two of the three spatial dimensions are available through experiment. These statistics can be obtained from the normalized cross correlation function as will now be outlined. The cross correlation function between two measurements is given by

$$R_{ij}(\delta, \tau) = \int_{-\infty}^{\infty} u_i(x, t)u_j(x + \delta, t + \tau)dt \quad (3.3)$$

where δ and τ represent spatial separation and a time delay between the two measurement positions. The normalized cross correlation function can then be expressed as

$$r_{ij}(\delta, \tau) = \frac{R_{ij}(\delta, \tau)}{[R_{ij}(0, 0).R_{ij}(\delta, 0)]^{0.5}} \quad (3.4)$$

From this function the turbulence length and time scales can be calculated as described by Townsend [20]. For a fixed reference frame the length scale as a function of separation is given by

$$l_{ij}(\delta) = r_{ij}(\delta, 0) = \frac{R_{ij}(\delta, 0)}{R_{ii}(0, 0).R_{jj}(\delta, 0)} \quad (3.5)$$

From this the integral length scale can easily be obtained from

$$\lambda_{ij} = \int_0^{\infty} l_{ij}(\delta)d\delta \quad (3.6)$$

In order to calculate the time dependent statistics a series of correlation peaks, one for each separation distance δ , are calculated. As the separation distance increases the peak moves away from the origin. Plotting these peak values as a function of δ and

$\hat{\tau}$, the associated time lag, produces a function $\hat{r}_{ij}(\delta, \tau)$. The integral time scale can then be calculated from

$$\tau_{ij} = \int_0^{\infty} \hat{r}_{ij}(\delta, \hat{\tau}) d\hat{\tau} \quad (3.7)$$

From the time delay $\hat{\tau}$ the convection velocity, U_c , and moving axis length scale, λ_{ij}^* can be calculated

$$U_c = \frac{\delta}{\hat{\tau}} \quad (3.8)$$

$$\lambda_{ij}^* = \int_0^{\infty} \hat{r}_{ij}(\delta, \hat{\tau}) d\tau \quad (3.9)$$

The majority of engineering analysis of turbulence is conducted in the frequency domain and as such is it worth noting that the cross spectra and the cross correlation function are Fourier transform pairs.

$$G_{ij}(\delta, f) = \int_{-\infty}^{\infty} R_{ij}(\delta, \tau) e^{-i2\pi f\tau} d\tau \quad (3.10)$$

It then follows that the normalized cross correlation function can be expressed in terms of the cross and auto spectra as

$$r_{ij}(\delta, \tau) = \frac{\int_0^{\infty} G_{ij}(\delta, f) e^{i2\pi f\tau} df}{[\int_0^{\infty} G_{ii}(f) df \int_0^{\infty} G_{jj}(f) df]^{0.5}} \quad (3.11)$$

In order to calculate the fixed axis length scale the cross correlation functions needs to be evaluated at $\tau = 0$ and it can be shown that this is equivalent to the real part of the cross spectra

$$R_{ij}(\delta, 0) = \int_0^{\infty} \text{Re}[G_{ij}(\delta, f)] df \quad (3.12)$$

Thus the length scales are given by

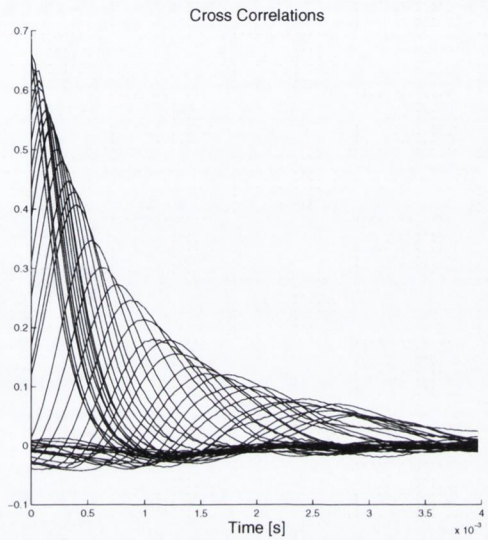
$$l_{ij}(\delta) = \frac{\int_0^{\infty} \text{Re}[G_{ij}(\delta, f)] df}{[\int_0^{\infty} G_{ii}(f) df \int_0^{\infty} G_{jj}(f) df]^{0.5}} \quad (3.13)$$

The fixed and moving axis integral length scales can now be calculated as outlined previously.

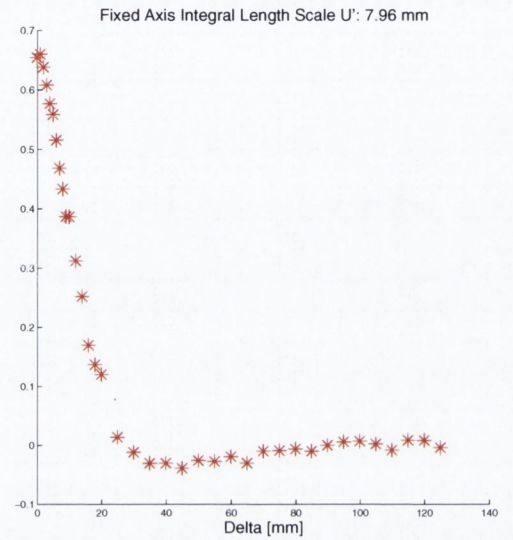
3.1. SPATIAL AND TEMPORAL CORRELATIONS

Figure 3.1 (a) shows the normalized cross correlation functions calculated from the cross and auto spectra for the baseline nozzle at $50\%L_c$. The fixed axis integral length scale is calculated by evaluating these functions at $\tau = 0$ and this value is plotted as a function of δ in figure 3.1 (b). Numerical integration is then used to calculate the integral length scale, λ_{11} in this case. The convection speed is calculated by plotting the correlation function peaks as a function of time and separation distance and using a linear fit. The slope of the fitted line provides the convection speed as shown in figure 3.1 (c). This fit is affected by the finite size of the cross wire and LDA measurement volumes both of which are on the order of $1mm$ which is comparable to the initial spacing of the test points. The accuracy of this fit was checked by insuring that the curve passed through the origin since there should be zero time delay at zero separation. The moving axis length scale also provides more difficulty as the value of the length scales often do not reach zero within the range of measurement positions. In order to overcome this problem the values must be extrapolated to zero and then integrated. An inverse Gaussian is fitted to the data and this is shown in figure 3.1 (d). In reality this curve may still underestimate the values for the moving axis length scale but was seen as an improvement over the lower under estimate found by simply integrating as far as the final measurement point.

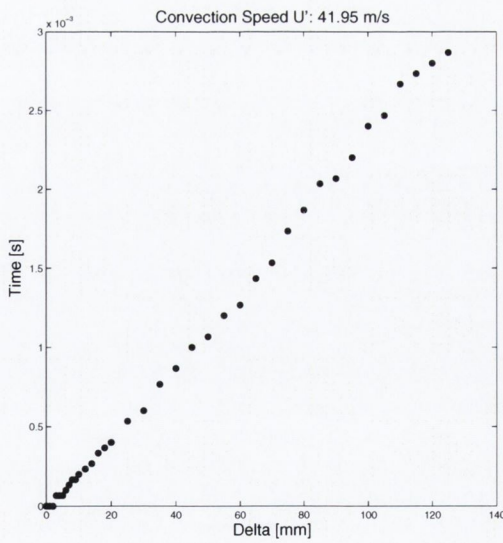
3.1. SPATIAL AND TEMPORAL CORRELATIONS



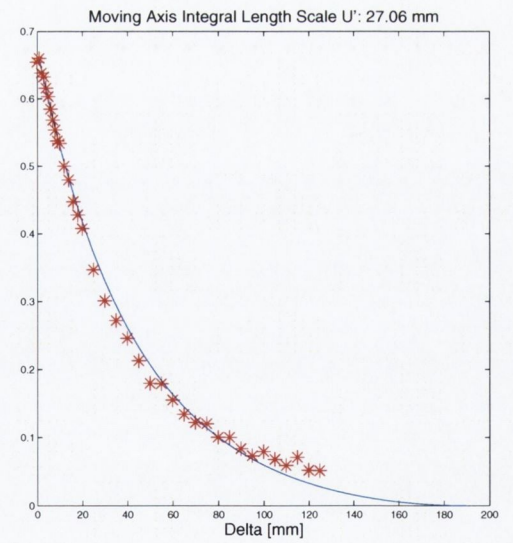
(a) Cross Correlations



(b) Fixed Axis Length Scales



(c) Correlation Function Peaks vs. Separation



(d) Moving Axis Length Scales

Figure 3.1: Spatial and Temporal Statistics u' Baseline Nozzle $0.5lc$

3.2 Frequency Dependent Statistics

The notion that turbulence consists of a superposition of a large number of eddies of different sizes, shapes and orientations has been accepted for quite some time. It was suggested by Townsend as early as 1974 that while local average statistics may provide important insight into the turbulence structures that they may also hide the multi-scale aspect of turbulence. Recent work by Kerherve et al. [21] has developed the concept of frequency dependent length scales, time scales and convection velocities. Through the use of this new technique more information has been revealed about the multi-scale structure of turbulence. This investigation will be one of the first to use a technique such as this to investigate the effects of complex nozzle geometries on the different turbulence scales. Due to the novel nature of this technique it will be unfamiliar to many researchers.

In order to attain the frequency dependence of the turbulence scales the space-time correlation function must be considered in the frequency domain. It was shown by Kerherve et al. [21] that this results in the definition of a “complex coherence function” using the auto and cross spectra as

$$\gamma_{ij}(\delta, f) = \frac{G_{ij}(\delta, f)}{[G_{ii}(f) \cdot G_{jj}(f)]^{0.5}} \quad (3.14)$$

From this the frequency dependent fixed axis length scales were given by

$$l_{ij}(\delta, f) = \text{Re}[\gamma_{ij}(\delta, f)] \quad (3.15)$$

$$\lambda_{ij}(f) = \int_0^{\infty} l_{ij}(\delta, f) d\delta \quad (3.16)$$

Using the phase of this complex coherence function a frequency dependent convection speed $U_c(f)$ can be calculated as shown below

$$\phi_{ij}(\delta, f) = 2\pi f \tau_{ij}(\delta, f) = 2\pi f \frac{\delta}{U_c(f)} \quad (3.17)$$

Finally the moving axis length scales can be obtained from

$$l_{ij}^*(\delta, f) = \frac{|G_{ij}(\delta, f)|}{[G_{ii}(f) \cdot G_{jj}(f)]^{0.5}} \quad (3.18)$$

$$\lambda_{ij}^*(f) = \int_0^\infty l_{ij}^*(\delta, f) d\delta \quad (3.19)$$

In order to calculate the frequency dependent integral length scales the experimental data often requires interpolation. The fixed axis length scale required identification of the first zero point crossing and the moving axis length scale required interpolation to zero for the larger turbulence scales. In order to achieve this a curve needed to be fitted to the length scales for each frequency. While a polynomial fit could have been applied to the data this would not have lended itself well to future inclusion in CAA codes. As such an effort has been made to find a curve fit that will be easily implemented in existing computer codes. Since many of this codes already employ Gaussian type models for some variables this was the logical starting point.

It was found that an inverse Gaussian curve suited the moving axis length scale while multiplying an inverse Gaussian and a sine wave matched the fixed axis length scales. The equations used for these curves are given below

$$c_1(\delta, f) = \frac{1}{e^{\frac{1}{2}(\alpha \frac{\delta}{L})}} \quad (3.20)$$

$$c_2(\delta, f) = c_1(\cos(2\pi T)) \quad (3.21)$$

For the c_1 curve the variable α is the reciprocal of the standard deviation and the variable L controls the width of the curve. Fixing the value of $\alpha = 2$ the curve was fitted to the lowest frequency length scale using L . The value of α was then linearly increased over the frequency range to produce the decay in the length scale seen for higher frequencies. The fixed axis length scales required this curve to be combined with a sine wave the period of which was set to match the first zero point crossing of the experimental data. An example of the types of curves produced by this method is given in figure 3.2. Figures 3.3 and 3.4 show the fitted curves for the fixed and moving axis length scales for a range of Strouhal numbers for the u' component of the baseline nozzle at $50\%L_c$.

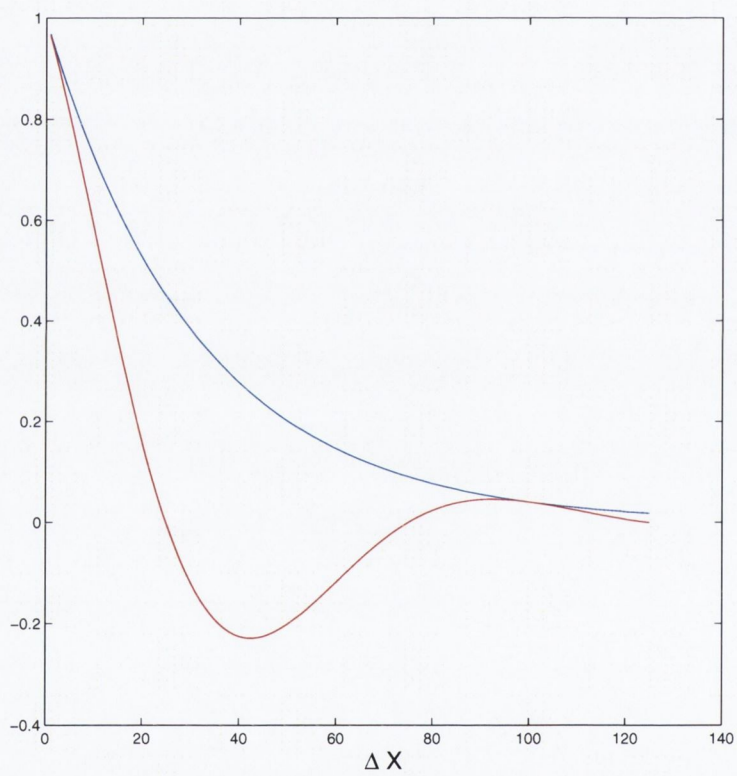
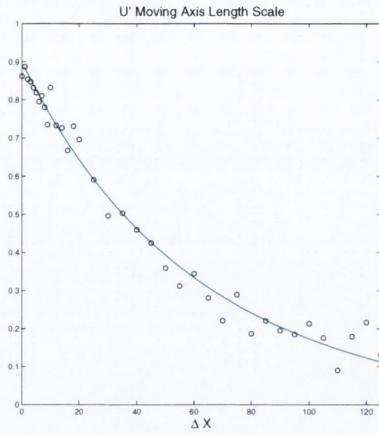
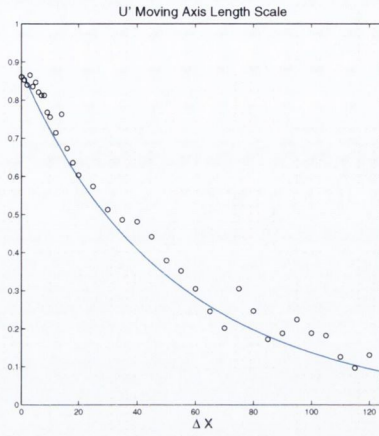


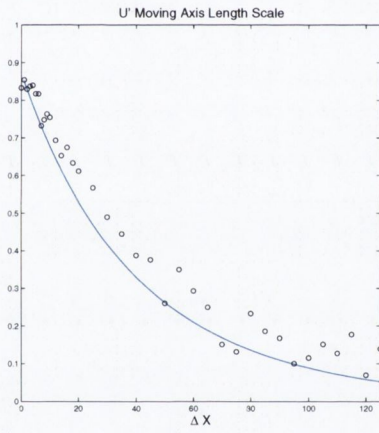
Figure 3.2: Example Curve Shapes for Fixed and Moving Axis Length Scales



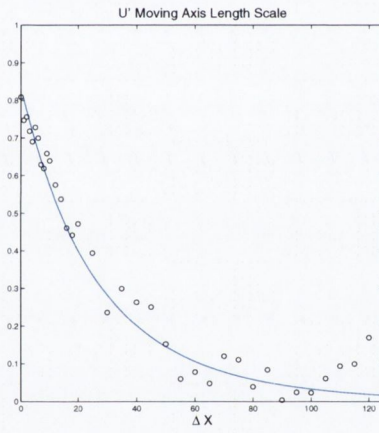
(a) $St = 0.001$



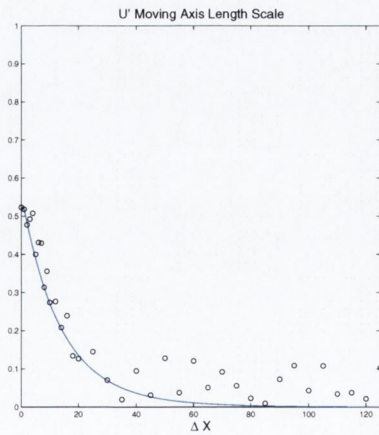
(b) $St = 0.01$



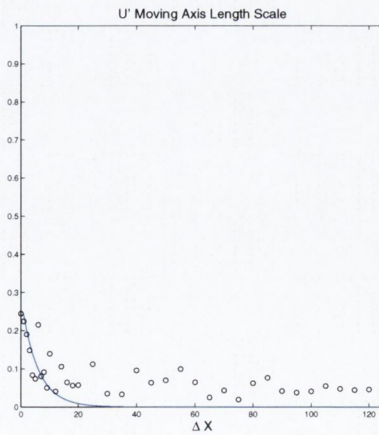
(c) $St = 0.25$



(d) $St = 0.50$



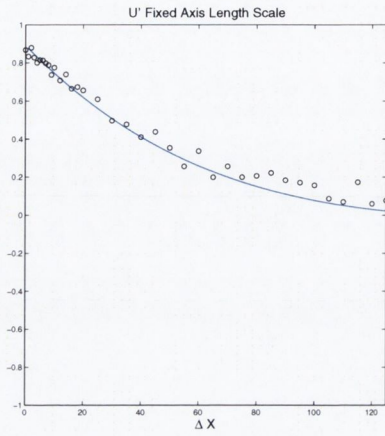
(e) $St = 1.0$



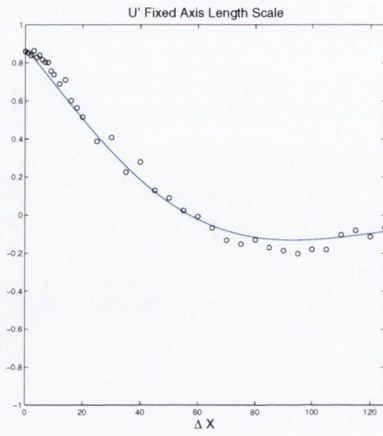
(f) $St = 2.0$

Figure 3.3: Frequency Dependent Moving Axis Length Scale u' Baseline Nozzle $0.5lc$

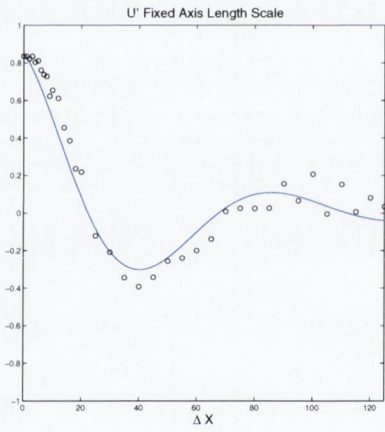
3.2. FREQUENCY DEPENDENT STATISTICS



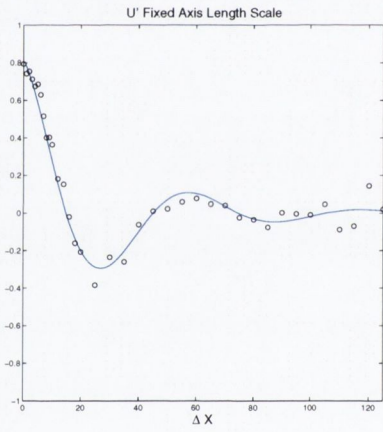
(a) $St = 0.001$



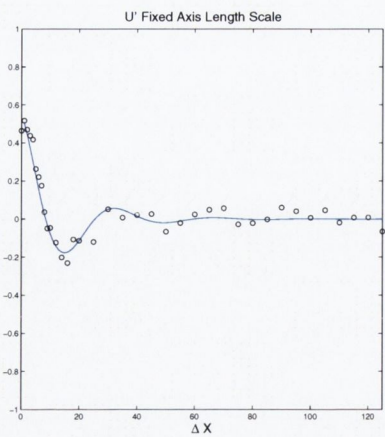
(b) $St = 0.01$



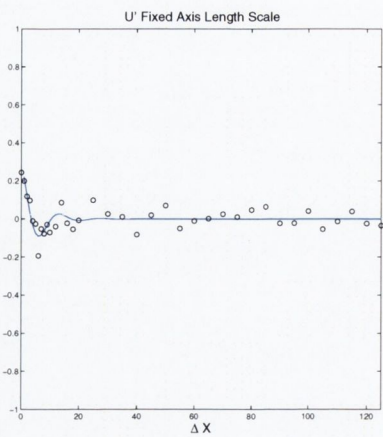
(c) $St = 0.25$



(d) $St = 0.50$



(e) $St = 1.0$



(f) $St = 2.0$

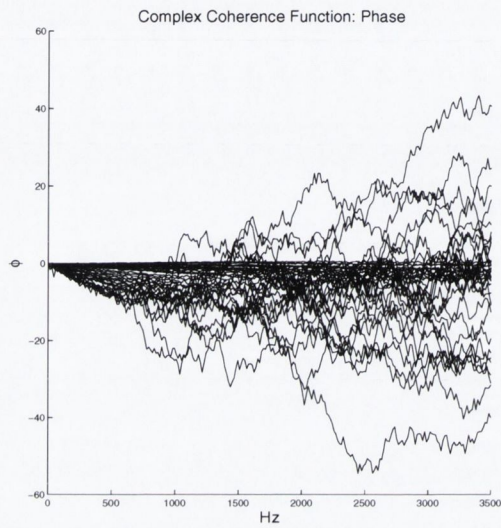
Figure 3.4: Frequency Dependent Fixed Axis Length Scale u' Baseline Nozzle $0.5lc$

In order to calculate the frequency dependent convection speed the phase of the complex coherence function is required. Unfortunately the phase is most sensitive to noise within the measurement. In order to achieve as accurate and smooth a phase result as possible a larger number of averages were required when calculating the cross and auto spectra and smoothing was required on the final phase data. The smoothing function applied to the phase is given below and this was applied for three iterations to the data.

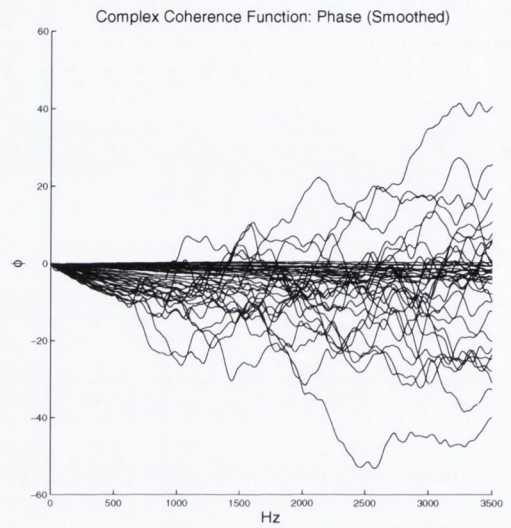
$$\phi(i) = 0.25\phi(i - 1) + 0.5\phi(i) + 0.25\phi(i + 1) \quad (3.22)$$

The value for the phase was then rejected beyond the point where the value deviated by greater than 5% of the expected value based on the previous 15 points. Figure 3.5 shows the results of this procedure for the baseline nozzle at $50\%L_c$. The smoothed and truncated phase is then used to calculate the convection speed as outlined above. An example of the convection speed for the u' component for the baseline nozzle at $50\%L_c$ is given in figure 3.6. Due to the extreme sensitivity of these calculations to error and the quantity of other data available only the frequency dependent length scales will be presented in future chapters.

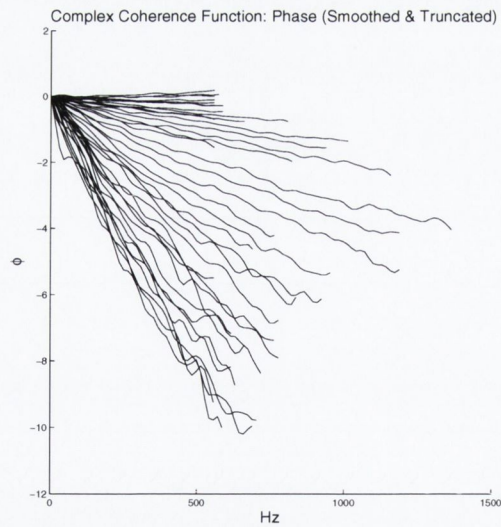
3.2. FREQUENCY DEPENDENT STATISTICS



(a) Raw Phase



(b) Smoothed Phase



(c) Smoothed and Truncated Phase

Figure 3.5: Cross Coherence Function Phase

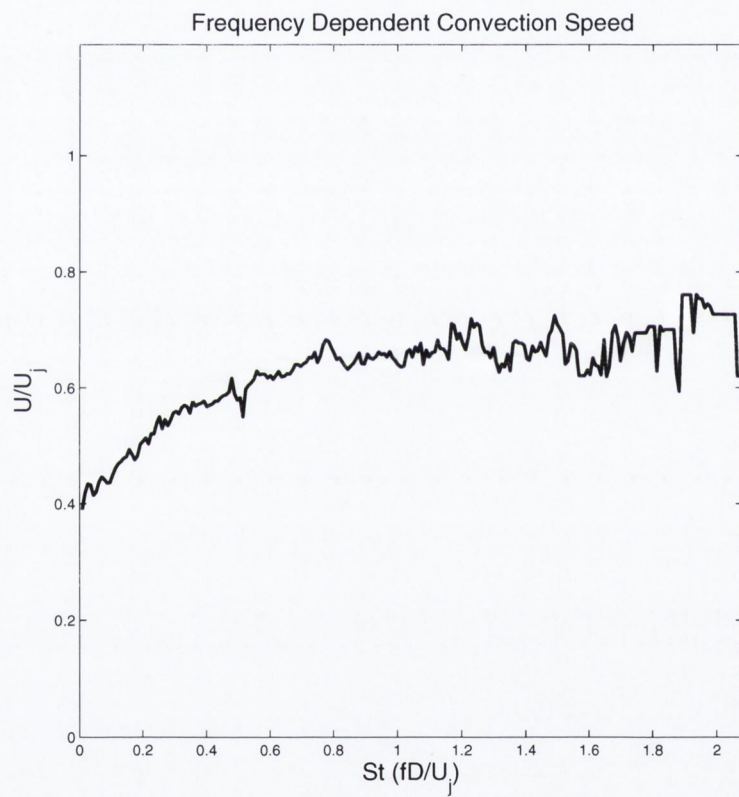


Figure 3.6: Frequency Dependent Convection Speeds

Chapter 4

Noise Reduction Technologies

There are numerous sources of noise found throughout the processes of a jet engine. Internally the fan and turbine blades produce noise which is related to the frequency of the blade rotation. In order to counteract the swirling motions produced by the blades the flow is straightened using vanes called stators. The interaction of the flow with these stators also produces noise. The first noise reduction technologies were based on optimizing the geometry of this system. By changing characteristics like shape, angle or number of these blades and stators this noise can be reduced. Further significant reductions are achieved through the use of acoustics liners in the inlet and exhaust ducts. Further research into optimizing the flow path [22] and boundary layer profiles [23] over these ducts is ongoing and they still have potential to further reduce sources of jet noise within the engine.

Unfortunately a significant portion of noise produced by the jet is produced by turbulence as the jet mixes with the free stream. This noise is produced after the flow has left the engine and therefore can not be removed by internal engine design. The majority of this noise is produced by mixing in the shear layer of the jet. By having two flows through the jet, the core and fan flows, the shear layer mixing is separated into two regions. The first is between the inner core flow and the outer fan flow and the second is between the fan flow and the free stream. The ratio between these two flows is called the bypass ratio and by optimizing this bypass ratio the jet noise can be further reduced. The majority of these noise reduction technologies have now been

optimized and new technologies are now required.

Several of these new noise reduction technologies focus on altering the flow structure after it leaves the nozzle in order to reduce the noise. The most popular technologies of this type currently being researched are chevrons and microjets, sometimes referred to as fluidic chevrons. Both of these technologies have achieved noise reductions of several dB and some researchers have begun to use them in combination to achieve further reductions as in the work by Alkislar et al [24].

4.1 Chevron Nozzles

The concept of nozzles with mixing enhancement features is not a new one. Lighthill stated that measures which shorten the mixing region or decrease turbulence intensity would likely prove beneficial for noise reduction [5]. These comments were being made in relation to lobed mixers which were being tested as early as the 1960s. Jet engines incorporating these designs did indeed show a significant noise reduction but posed problems in terms of weight increase. The difficulties associated with engineering these nozzles were too great in comparison to other noise reduction technologies yet to be implemented in jet aircraft. Nearly half a century on researchers have returned to mixing enhancement features to further reduce the noise.

Beginning in the late 1990s NASA personnel at the Glenn Research Center conducted a number of experiments on the noise reduction achieved from various nozzle designs. Since there was little or no understanding of how to optimize these nozzles for noise reduction a wide variety of designs were put forward and tested. Beginning with the lobed mixer designs from the 1960s tests were run on one quarter scale nozzles with internal lobed mixers. These results showed that lobed mixers reduce the low-frequency noise and produce a more uniformly mixed exit flow however they also increase the high-frequency noise upstream possibly due to enhanced mixing inside the nozzle [25]. Further tests were run on nozzles using chevron and tabbed designs. These were found to have an improved performance over the lobed mixer designs; mainly due the significantly lower thrust loss for similar noise reduction. They also showed that in comparison with chevrons, tabs appeared to be an inefficient method of reducing

jet noise [26]. By testing this wide variety of nozzle design they selected those which showed the most potential to go on for further research. Two point turbulent statistics were acquired for these nozzles in order to quantify the changes to jet structure [27]. Through extensive experimental measurements of the selected nozzle designs, including far field noise and turbulence statistics, some insight had been gained into which technology would likely prove most beneficial for noise reduction.

Until this point research had focused on high speed hot jets containing both fan and core flows. Tests had been carried out on configurations where both fan and core nozzles had been altered with mixing enhancement devices and also where only one of the two had been altered. It was realized that in order to better understand the effects of the chevrons a more parametric approach was required. In 2004 a report was published by NASA Glenn Research Center which detailed a parametric study on 10 single flow nozzles which are shown in figure 4.1 [28]. Using these simpler nozzles they were able to draw several conclusions about the importance of chevron count, penetration, length and symmetry. Based on their findings it appears that chevron length is not a key factor in the noise reduction and that asymmetry in the nozzle design marginally decreases the effectiveness of the chevrons. It was found that the key features are chevron count and penetration.

A high number of chevrons decreases the low frequencies without a significant high frequency penalty. The maximum number of chevrons in a nozzle design is limited by structural stability so further improvements in noise reduction require control of the chevron penetration. The results showed that an increase in chevron penetration into the flow further decreases the low frequency noise coupled with an increase in high frequency content. This demonstrated that varying chevron penetration can control the frequency content of the noise produced. The explanation for the effects of chevrons was the production of counter rotating vortices formed from the chevron tips. These vortices increase mixing in the shear layer of the potential core and their production and properties are controlled by the geometries of the chevrons. The study also compared the effects of chevrons on hot and cold jets and found that there were no significant differences in the behavior. This showed that valid conclusions can be drawn about chevron behavior in real life jet engines from studies on isothermal jets.

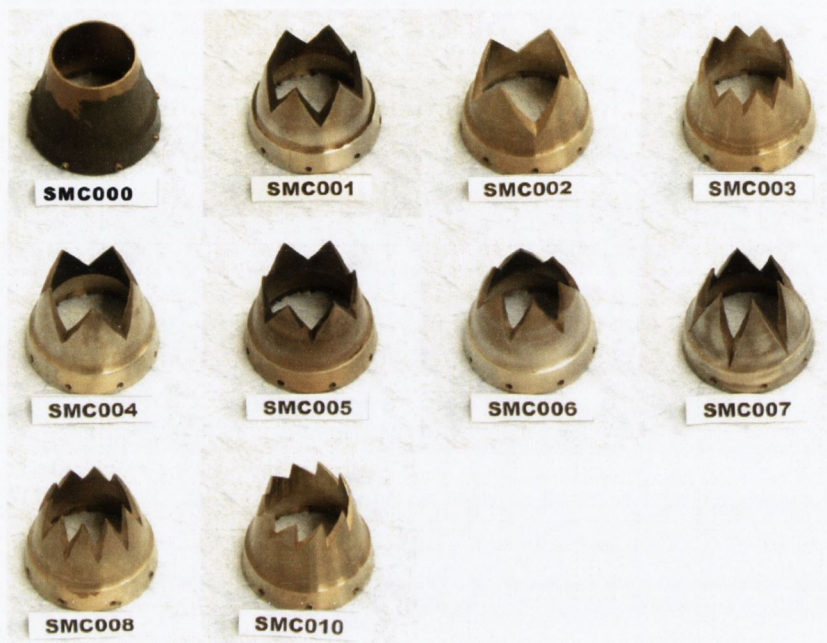


Figure 4.1: NASA Nozzle Designs

These were essentially empirical results but they could be used to begin nozzle design for commercial aircraft. Boeing has since developed a highly advanced system for testing chevron penetration on a full scale commercial aircraft. They have implemented a variable geometry chevron design on a Boeing 777-300ER with GE-115B engines [1]. Figure 4.2 shows the nozzle design implemented on the aircraft. The main aim was as a design tool to compare chevron configurations and investigate the possibility that a different configuration will provide better noise reduction at a different stage of flight. They used a 14 chevron nozzle on the outer exhaust flow. Since it has been shown that chevron immersion leads to a thrust penalty their current designs aim towards minimum immersion of the chevrons into the flow. Each chevron is comprised of shape memory alloy actuators combined with a system of heaters and strain gages to change and control the chevron immersion. They are designed for a tip motion of 0.9 inches which translates into approximately 3 degrees. The effects on jet noise were measured using a ground based microphone array during take off and the results found a reduction of $2dB$ could be achieved. During flight interior microphones were used to measure cabin noise where improvements of $1 - 2db$ were also achieved.

One particularly interesting proposal in relation to the community noise results



Figure 4.2: Boeing 777-300ER with Chevron Nozzle

of their research is the possibility of directing the noise away from the ground based observer [29]. It is already known that the noise field is asymmetric due to interactions with the aircraft frame. The possibility of varying chevron immersion azimuthally and hence varying the mixing around the nozzle means that it may be possible to direct the noise away from the ground based observer. This offers the possibility of reducing community noise using chevrons without necessarily reducing the overall noise produced by the jet. The success of this variable geometry chevron design has led to it being incorporated into Boeing's next generation of commercial aircraft. Beginning with the release of the Boeing 787 Dreamliner noise reduction using chevron nozzles may become a standard feature of future aircraft.

In conjunction with the research being conducted at the NASA facilities and on full scale Boeing flight tests there are numerous other research projects underway that are involved with the effects of chevrons. Several attempts are being made to run the first numerical simulations of chevron nozzles. Due to the limitations on the size of an LES computation several of these computations have focused on capturing the changes to the flow near the nozzle. The increase in high frequencies produced by

chevron nozzles is often attributed to the increased mixing near the nozzle. A recent investigation of the near nozzle region of the flow by Uzun et al [7] showed that the turbulence length and time scales are being effected by chevrons. Some work has also been done by Mihaescu et al [30] in making aeroacoustic predictions from LES results on chevron nozzles. These results have been successful in capturing the overall noise reduction produced by chevrons.

The research so far has been hampered by the large number of variables and geometries associated with nozzles that have mixing enhancement features. The effects on the far field sound and on the jet structure have been well documented but more fundamental research is required on the effects on the turbulence properties. This change in the nature of the turbulence needs to be quantified and incorporated into computational models before accurate aeroacoustic predictions of these new nozzle designs are possible.

4.2 Summary

The effects of chevron nozzles are driven by chevron count and penetration into the flow. In general the effects include

- Increased mixing in the nozzle region resulting in more isotropic turbulence. This produces a faster centerline velocity decay and a shorter potential core.
- A high chevron count leads to a noise reduction for low frequencies without a high frequency penalty.
- As the chevrons are immersed into the flow further low frequency reductions are possible but are coupled with a high frequency penalty.
- The latest nozzle design is based on controlling chevron immersion to achieve additional noise reduction during take off and landing and reducing thrust losses during flight. This design has been realized in the new generation of Boeing commercial aircraft.

- The LES and CAA computations have so far captured some of the changes to the turbulence properties and the overall reduction in noise levels. They have so far been confined to the nozzle region and do not include variable chevron immersion.

Due to the large number of variables involved in chevron nozzle design by necessity most research has focused on the effects of chevrons on far field sound. This approach has allowed researchers to develop the current variable geometry chevrons found on Boeing's next generation aircraft by identifying the key features required to achieve noise reduction at low thrust penalty. Now that this has been achieved more fundamental research on the effects these nozzles are having on the jet structure and the turbulence properties is required. A key objective of this research is to fill the gap in this more fundamental knowledge that has been left by the drive to achieve the most beneficial noise reduction. This knowledge is required to enable the fields of CFD and CAA to accurately predict the effects of these new nozzle designs.

4.2. SUMMARY

Chapter 5

Experimental Facilities and Instrumentation

This chapter describes the experimental facilities and measurement techniques used in this investigation. A description of the subsonic open jet facility used for these experiments is provided. In addition the instrumentation available and the data acquisition and processing procedures are outlined. The use of hot wire anemometry requires accurate calibration and an overview of the calibration procedures and facilities developed for this work is provided.

5.1 Small Scale Jet Rig

The subsonic open jet facility described by Chatellier et al [31] was used for all tests in this investigation. The jet is powered by a $5.5kW$ centrifugal blower. The $50mm$ diameter jet discharges into quiescent air from the plenum through a bell mouth of elliptic cross-section. The facility is capable of achieving velocities from $30m/s$ to $84m/s$. This provides a Reynolds number range of approximately 10^5 to 3×10^5 for a standard $50mm$ diameter nozzle. In order to insure a low turbulence intensity in the nozzle exit and to uncouple the flow from the centrifugal blower a series of honeycomb screens is used in addition to the bell mouth. A schematic of the facility is provided in figure 5.1.

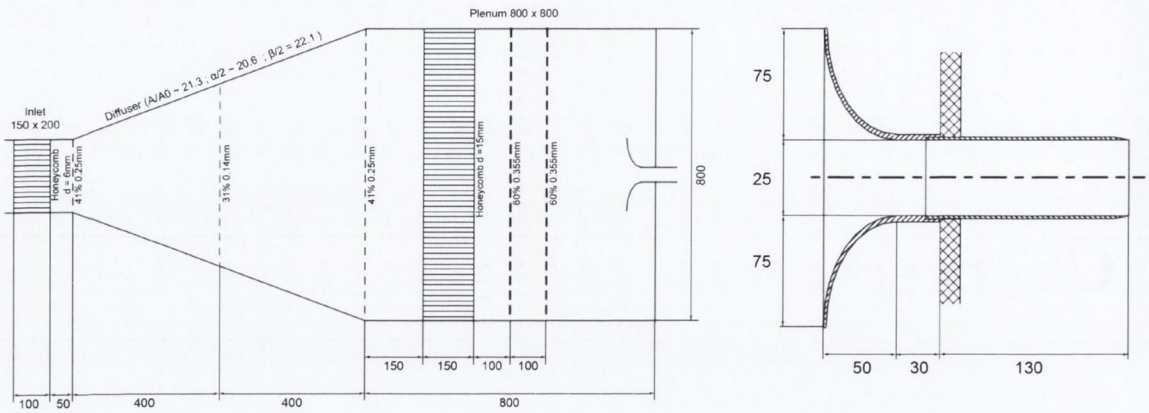


Figure 5.1: Subsonic Open Jet Facility and Nozzle Close Up

5.2 Nozzle Designs

As extensive testing had been performed on a 50mm diameter single jet nozzle this nozzle was used as the baseline comparison for the chevron nozzles. This single jet nozzle had been manufactured using rapid prototyping technology available within the department. This process provides high dimensional accuracy and can deal with complex geometries. This made it a perfect choice for producing accurate, uniform chevrons which would be difficult to machine using traditional manufacturing techniques.

Due to the large number of factors which come into play for complex nozzle geometries the designs were chosen to allow for future modification while also setting a realistic limit on the experimental time required for the study. The most relevant variable for current chevron nozzle designs is chevron immersion. The designs currently being pursued by Boeing involve a variable geometry chevron design [1]. This allows for the thrust penalty associated with chevron immersion to be removed once the aircraft has reached cruising altitude. Any future CAA models must be able to take account of this changing immersion of the chevrons during the initial take off period.

A high chevron count was chosen due to the evidence that increased chevron count provides noise reduction without a high frequency penalty [28]. The number of chevrons on each nozzle was limited to eight in order to insure they were struc-

turally rigid enough to avoid vibration once immersed into the flow. The chevron length was chosen as 30mm since length was shown to be a less significant variable and this length was comparable to nozzle designs used during tests at NASA Glenn Research Center [28]. The chevrons tapered to a minimum thickness of 1mm . The nozzle diameter in each case is 50mm taken at the base of the chevrons and the nozzle exit was taken as the tip of the chevrons.

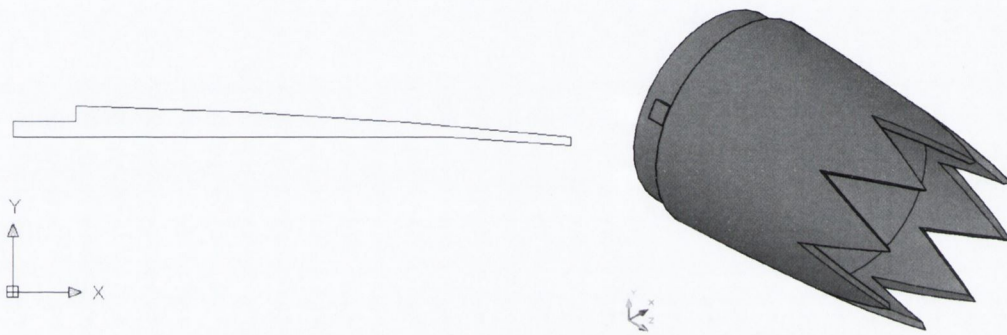


Figure 5.2: Four Degree Chevron Nozzle Profile and Model

Due to the fact that chevron immersion results in a thrust loss it is desirable to keep the immersion angle to a minimum. A baseline chevron nozzle with no immersion into the flow was required. In addition two other nozzles with increasing immersion were chosen and these were the two and four degree chevron nozzles. Figure 5.2 shows the four degree nozzle CAD profile and 3D render. These levels of immersion are comparable to the variable geometry chevrons tested by Boeing [1]. An overview of the nozzle parameters is provided in table 5.1.

Nozzle ID	Chevron Count	Chevron Length	Penetration Angle	Penetration	Diameter
SJ	0				50mm
N0	8	30mm	0°	0.0mm	50mm
N2	8	30mm	2°	1.0mm	50mm
N4	8	30mm	4°	2.1mm	50mm

Table 5.1: Nozzle Parameters

5.3 Seeding Particle Generation

Both laser based measurement techniques used in this work require the flow to be seeded. Seeding particles were produced using a commercial smoke machine; the Phantom PS31 produced by PeaSoup Ltd. A supply of compressed nitrogen is used to nebulize the working fluid before being passed through the heating element. This machine is capable of producing smoke particles from any working fluid since the temperature of heating element can be adjusted. By altering the ratio of gas to fluid the particle size can also be accurately adjusted. The primary advantage of this system is its ability to produce a uniform particle size. These LDA experiments used a commercially available oil based fluid again manufactured by PeaSoup. By varying the gas supply smoke particles ranging from $0.2 - 1.5\mu m$ can be produced using this fluid. The maximum size of $1.5\mu m$ is ideal for use with LDA while smaller particle sizes can be used for PIV.

5.4 Particle Image Velocimetry

Particle Image Velocimetry, PIV, is a non-intrusive laser based technique capable of providing quantitative flow field information including turbulent statistics. The flow is seeded with neutrally buoyant tracer particles which are illuminated using a double pulsed laser beam. This laser beam passes through a series of lenses to produce a light sheet which covers the measurement region. A high speed camera records a pair of images from the two light pulses. Since the time interval between the two images is known the movement of the particles and hence the flow velocity can be calculated [32].

This process involves dividing each image into a series of interrogation windows and performing a $2D$ cross correlation between the same window in each image to evaluate the particle displacement. This method provides the average displacement for all particles in the interrogation window. Interrogation window size should be chosen such that all particles within the window are moving with a relatively homogeneous velocity and there are a reasonable number of particles within the window. The implication of

this is that the spatial resolution of the calculated vector field depends on the size of the interrogation window which should be small enough to ignore any velocity gradients. The results can be improved by using overlapping interrogation windows and multiple iterations to provide the software with expected values of the local velocity.

The timing of the laser pulse should be such that all particles in the flow have had time to move a detectable distance while remaining in the same interrogation window. This has implications for flows with high velocity gradients such as jets. Choosing a time step to provide optimum displacement for particles at the jet velocity will be less than optimum for the particles in the shear layer and surrounding medium. However if the time displacement is chosen for those particles in the shear layer then the particles in the potential core of the jet may have moved too far between pulses to be within the same interrogation window. Both of these situations may result in an incorrect vector calculation. As a result a compromise must be chosen that captures the entire velocity range as accurately as possible. Figure 5.3 shows the experimental setup for these investigations. The red area in the figure marks one of the four overlapping measurement regions. Figure 5.4 shows an example vector calculation for the 0° nozzle.

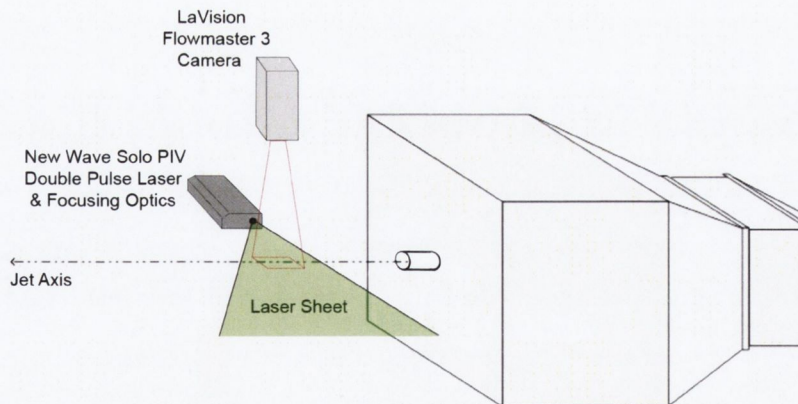


Figure 5.3: PIV Experimental Setup

Using the correct post-processing procedures PIV can provide an accurate and more global representation of the flow than single point measurements making it much easier to identify areas of interest. The PIV system used for these experiments featured a $15mJ$ New Wave Solo PIV Double Pulse Laser. The images are recorded using a double exposure LaVision Flowmaster 3 camera that has a maximum resolution of

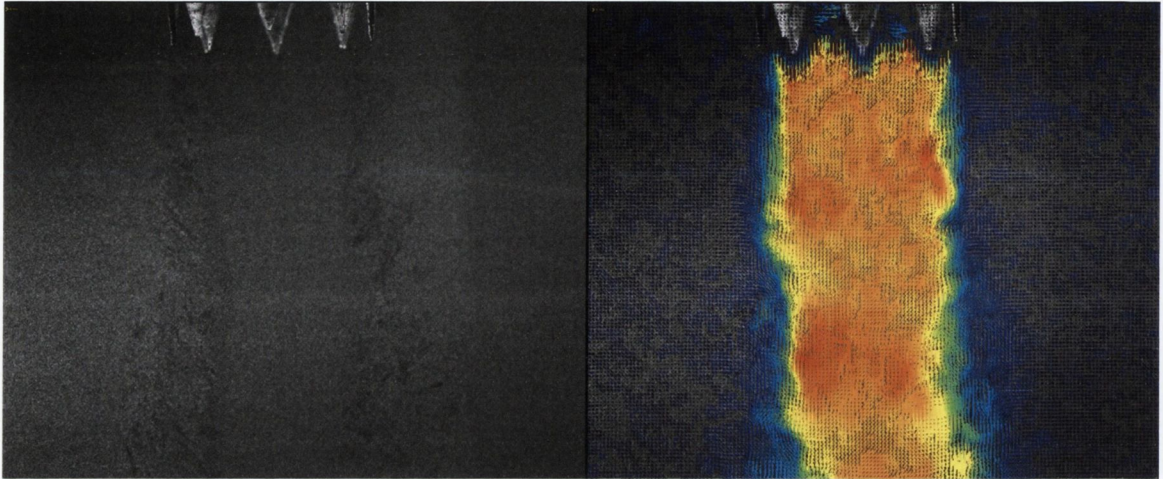


Figure 5.4: PIV Calculation Example

1280x1024 pixels. Data acquisition and processing is preformed using the supplied LaVision DaVis software. The system is capable of operating at $4Hz$ i.e. acquiring four PIV image pairs every second.

5.5 Laser Doppler Anemometry

Laser Doppler Anemometry, LDA, is another non intrusive measurement technique which relies on seeding particles within the flow. The principle advantages of this technique are the high spatial and temporal resolution it provides. An LDA system consists of a laser beam passed through a beam splitter, Bragg cell and focusing optics. The beam splitter and Bragg cell work to split the laser beam into two beams of equal intensity one of which has been slightly frequency shifted. These beams are then passed to a probe which contains the focusing optics. These beams are made to intersect a certain distance from the probe. The interference pattern of the two light beams is a series of light and dark fringes. The spacing of these fringes is a function of the laser wavelength and the beam angles. This area of interference is the measurement volume. The frequency shift that was introduced into one of the beams causes these fringes to move at a velocity related to the frequency shift of the Bragg cell.

As a seeding particle passes through the measurement volume it scatters light. This scattered light contains a Doppler frequency related to the particle velocity and

the fringe spacing. Due to the movement of the fringes a particle traveling at the same speed in opposite directions will produce a different signal. Receiving optics mounted either within the probe or attached to an external camera lens pass this light to a photo multiplier. The signal from this photo multiplier gets sent to the processing hardware which calculates the velocity. Figure 5.5 shows the setup for the LDA and hot wire experiments used in this investigation.

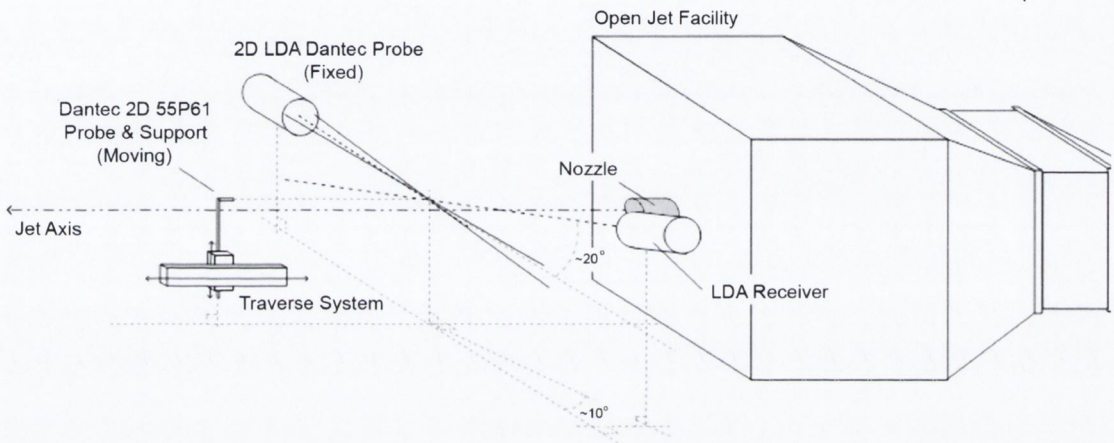


Figure 5.5: LDA Experimental Setup

The LDA system used for these experiments consists of a $500mW$ argon ion laser provided by Dantec Dynamics. The system is a two component system which allows for the simultaneous measurement of two velocity components. The laser is split into two pairs of beams of different wavelengths. The two beams have wavelengths of $514.5nm$ and $488nm$ producing green and blue beams respectively. The two beam pairs are focused on the same location producing co-incident measurement volumes which are $0.12mm \times 0.12mm \times 1.6mm$ with $1.6mm$ being the length of measurement volume.

5.6 Constant Temperature Anemometry

Constant temperature anemometry, or hot wire anemometry, was the first measurement technique that allowed for fast responsive measurements of turbulence. The continuous analogue signals provided by the probes also lend themselves well to being digitally sampled at high data rates. The foundation for this technique is based on the

5.6. CONSTANT TEMPERATURE ANEMOMETRY

principles of heat transfer. This technique uses a probe usually containing a tungsten wire approximately 1mm in length and $5\mu\text{m}$ in diameter. This wire is maintained at a constant overheat temperature above the fluid temperature. The resistance of the wire should be constant for a given temperature. A CTA system uses a Wheatstone bridge to keep resistance, and therefore temperature, constant by varying the voltage across the wire. Using the thermodynamic principles of a heated cylinder in cross flow the voltage required to maintain the temperature can be related to the heat loss and hence the flow velocity.

The advantages of this technique include a very high frequency response and high data rates. The probes can also be used over a very wide velocity range but require an accurate calibration. The intrusive nature of the probe and this calibration requirement are the principle disadvantages of this technique. For most applications a simple single wire ($1D$) probe is used. Due to the nature of this probe the measurement is not directionally sensitive. In addition any thermal variation in the flow will affect the calculated velocity. As a result these probes are best suited to unidirectional flows of constant temperature. A typical hot wire anemometry set up is shown in figure 5.6.

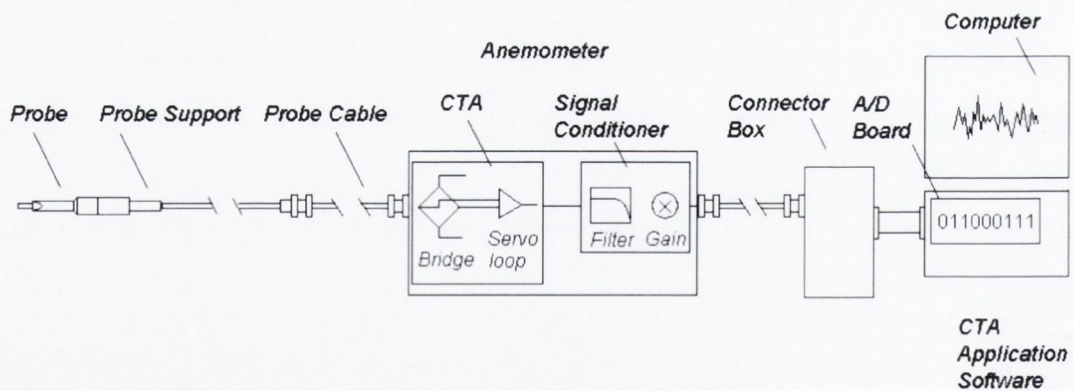


Figure 5.6: Dantec Dynamics Hot Wire System

The CTA system used in this investigation has several capabilities to overcome these limitations. The inclusion of a temperature dependent resistor in the Wheat-

stone bridge with temperature sensor in the flow compensates for any variation from the calibration temperature. By using a probe consisting of two wires orientated perpendicular to each other additional velocity components can be measured. These probes, known as X-wire probes, require additional steps in the calibration procedure.

5.6.1 Hot Wire Probe Calibration

The department has a self-contained calibration unit for use with hot wires. This unit consists of a compressed air supply, settling tank, mass flow meter, yaw manipulator and jet with interchangeable nozzles for different velocity ranges and this is shown in figure 5.7.

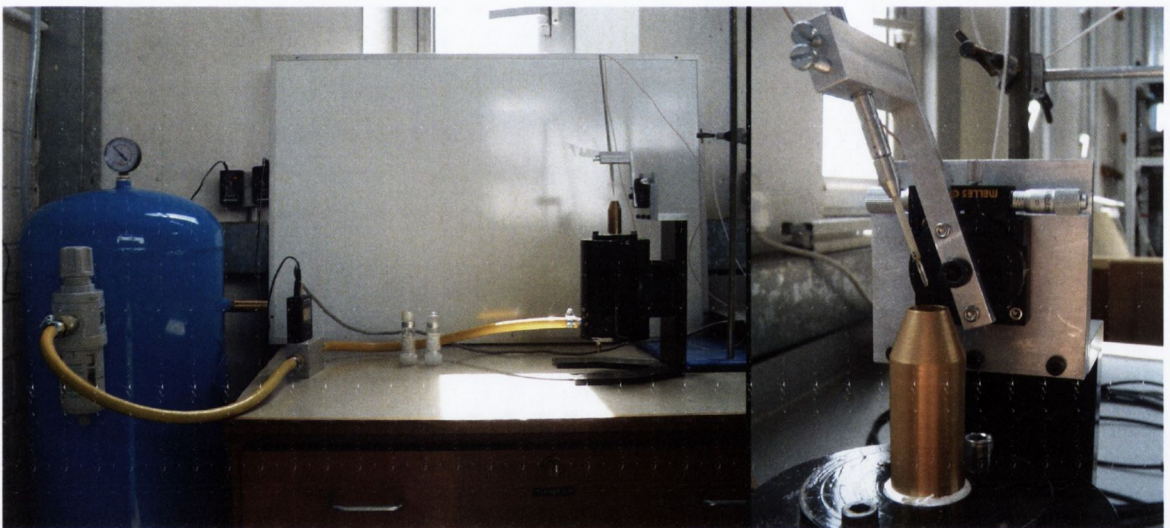


Figure 5.7: Calibration Facility

In order to achieve accurate results using a X-wire probe a directional calibration is required in addition to the usual velocity calibration. The Dantec 55P61 x-wire probes used in this investigation is shown in figure 5.8. This probe consists of two $5\mu m$ wires in parallel planes orientated at 45° to the probe axis. Using the yaw manipulator the probe is rotated through a series of angles from -45° to $+45^\circ$ about the probe axis. At each extreme one wire is positioned perpendicular to the flow and one wire parallel to the flow. At each angle where one wire is perpendicular to the flow a velocity calibration can be carried out as usual using a fourth order polynomial fit to the data. This velocity calibration will provide an effective velocity V_{eff} once the

wire is positioned at an angle to the flow which will be related to the actual velocity magnitude \tilde{V} and a function of the angle $f(\alpha)$.

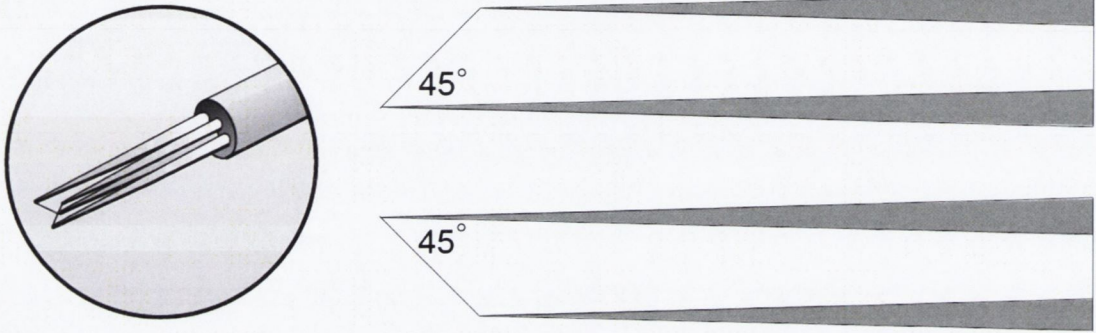


Figure 5.8: Dantec Dynamics 55P61 X-WireProbe

$$V_{eff} = \tilde{V} f(\alpha) \quad (5.1)$$

The standard function for $f(\alpha)$ is given below where m is a calibration constant.

$$\begin{aligned} f(\alpha) &= \cos^m \alpha \\ g(\alpha) &= m \tan \alpha \end{aligned} \quad (5.2)$$

At each angle a velocity calibration is conducted and this produces a complete calibration map for the probe as shown in 5.9. From this the value of m can be calculated and used to calculate the U and V velocities as outline below where $\bar{\alpha}$ is the measurement angle.

$$\begin{aligned} U &= \frac{V_{eff1} + V_{eff2}}{2f(\bar{\alpha})} \\ V &= \frac{V_{eff2} - V_{eff1}}{2f(\bar{\alpha})g(\bar{\alpha})} \end{aligned} \quad (5.3)$$

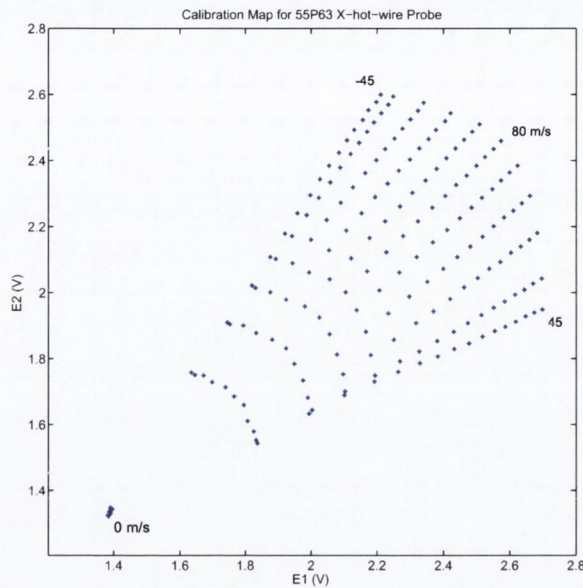


Figure 5.9: Calibration Map Dantec 55P61 X-Wire Probe

5.7 Data Acquisition and Error Analysis

5.7.1 PIV

The PIV system consists of purpose built acquisition hardware and software which provides the calculated velocity data. Provided the correct experimental parameters have been chosen this system is capable of providing extremely accurate velocity values. The guideline for optimum particle displacement within an interrogation window is less than a quarter the window size. For this investigation four vector calculations of decreasing interrogation window size were computed. The initial two passes were conducted using 64×64 pixels interrogation windows and the final two passes at 32×32 pixels. The timing of the laser pulse was set to allow for a pixel displacement of 8 pixels for the jet velocity of 84 m/s . Recent work has shown that the latest PIV algorithms can accurately calculate particle displacement to within 0.01 pixels under ideal conditions however a more reasonable value for laboratory conditions is 0.1 pixels. This produces an error of 1.25% for particle displacements at the jet velocity from the PIV algorithm itself.

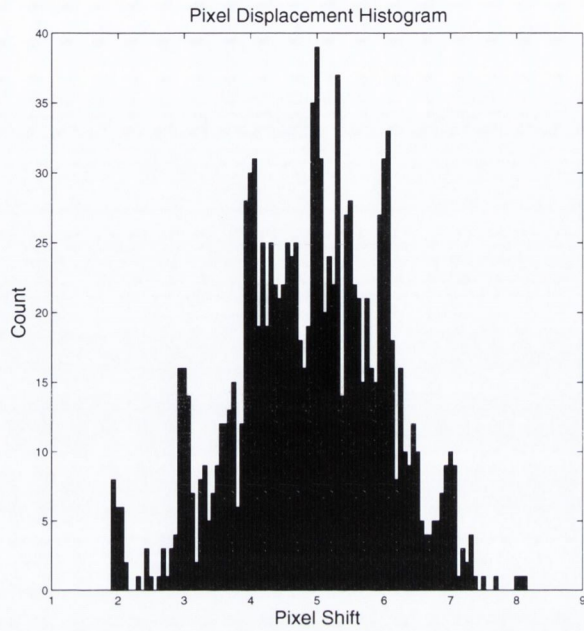
The quality of the seeding is also vital in achieving good PIV data. For these tests considerable effort was spent achieving relatively equal levels of seeding both within

the jet and in the surrounding medium. In addition to seeding the jet through the compressor inlet an enclosure containing the jet rig and PIV system was constructed and separately seeded. This was found to be vital in maintaining uniform seeding throughout the shear layer and avoiding low particle densities. The seeding particle size is also a key factor. If the seeding particles are too small the pixel displacements will tend towards integer values in a phenomena known as peak locking [32]. This effect can be detected by plotting a histogram of the particle displacements. Figure 5.10 shows a comparison of a generated peak locking histogram with a histogram from a single calculated vector map of this investigation. As can be seen the histogram from this investigation shows a smooth range of pixel displacements from 8 pixels at the jet velocity through to 0 pixels in the surrounding medium. The smooth transition through these regions is a good indication of particle seeding quality.

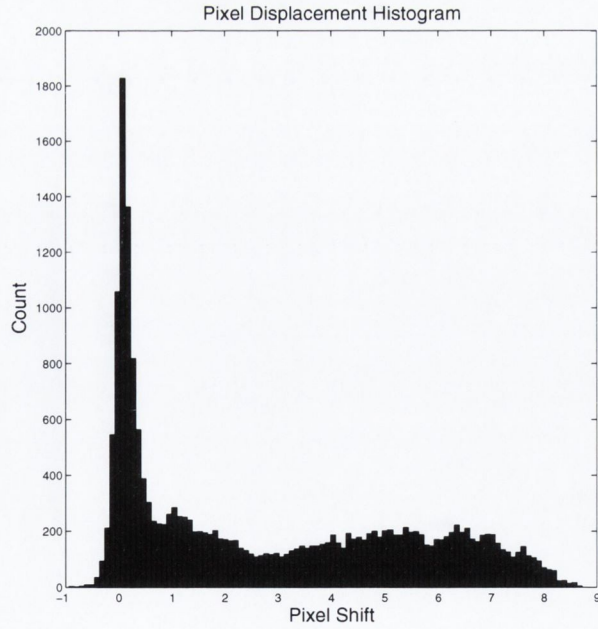
There are other factors which effect the accuracy of the results which are harder to quantify. These include reflections and out of plane displacements which can result in bad vector calculations. As a result a rigorous post processing procedure must be applied to the vectors in order to ensure their accuracy. The common method is the Q peak test used in combination with a median filter. The Q peak test compares the correlation peak representing the displacement with the highest noise peak [32]. The ratio is calculated using the formula below and compares the ratio of these two peaks, P_1 and P_2 , after the minimum value has been removed. This ratio is set so that the value of P_1 can be confidently stated not to be noise.

$$Q = \frac{P_1 - p_{min}}{P_2 - p_{min}} \quad (5.4)$$

This technique is combined with a median test developed by Westerweel [33]. This method compares a vector against the median and deviation of the surrounding eight vectors according to the formula below. The vector is rejected if it is found to be outside the allowable range of the values.



(a)



(b)

Figure 5.10: Pixel Displacement Histograms (a) Peak Locking Example (b) Measurement Example

$$U_{median} - U_{rms} \leq U \leq U_{median} + U_{rms} \quad (5.5)$$

In order to investigate the quality of the data the values of these tests were recorded for a series of images in the $0 - 2D$ region of the 0° nozzle. This region was chosen as it contained the steepest velocity gradient, reflections from the nozzle and a significant region of ambient fluid outside the jet and as such it should represent the worst case scenario for the data validation. The Q test criterion was set to remove vectors which had a P_1 value less than $1.3P_2$. On average the P_1 value was $2.72P_2$. The median filter was set to remove vectors greater than $2xRMS$ of the surrounding vectors. Based on these criteria there were 0.26% bad vectors in the measurement region per image.

Evidence of the quality of the data is demonstrated by the fact that no interpolation was required when joining the results from the four measurement regions for each jet.

5.7.2 LDA

The LDA system manufacturers provide dedicated acquisition hardware and software which provides the calculated velocity data. The supplied calibration certificate reports a measurement uncertainty of 0.12%. While this is an exceptional level of accuracy there are other factors which can effect the results. If the measurement volumes are not aligned perfectly with the axis of the jet there will be some error in the axial and radial velocity magnitudes. The measurement volumes are $1.6mm$ across and are not a true point measurement.

The largest draw back to the technique is that the flow needs to be seeded with particles to scatter the light. Since these particles will be irregularly distributed there is no way to control the sampling rate for the data. In addition the sampling rate will be coupled with the flow since the number of particles passing through the measurement volume will increase at higher speeds. Irregularly spaced data also presents difficulties for some analysis techniques and can lead to computationally expensive post processing. To counter this problem researchers originally applied analogue fil-

ters and equidistant time resampling and the possible effects of these techniques on the spectral content of the signal were ignored [34]. Other factors which affected the spectral content were already known. Examples of these are reflections and the scattering of light from multiple particles passing through the measurement volume; these were known to produce noise in the signal. Each of these noise signals is indistinguishable from a genuine turbulence fluctuation but as a collective whole they form a very recognizable white noise spectrum. This is easily identified and removed from the genuine turbulence spectrum. Provided that the effects of the resampling process are similarly calculated and removed from the signal the problem of irregularly spaced data is overcome.

The sample and hold technique allows the data to be easily resampled at the desired rate and the effects on the turbulence spectrum were shown by Simon et al [35]. The technique is based on a simple time resampling of the data. This is highly advantageous since it is less computationally expensive than other techniques. A continuous time signal is reconstructed from the point velocity measurements by simply holding the same value until the next point is measured. This signal can then be artificially resampled at the desired frequency using a simple computer algorithm. It has been shown that this process adds a step noise component to the signal and also acts as a low pass filter which attenuates the reconstructed data [35].

The effect of the low pass filter is related to the mean data rate of the original data and the resampled data rate. As shown by Fitzpatrick and Simon [36] this filter is accurately calculated using the formula below where f_m is the mean data rate and f_r is the resample frequency.

$$L_d(f) = \frac{1 - e^{-f_m/f_r}}{1 - e^{-f_m/f_r} e^{-j2\pi f/f_r}} \quad (5.6)$$

An estimate of the step noise can be obtained from the filtered auto spectra of the data. This procedure assumes that the step noise is uncorrelated with the signal and that the step noise in two signals is uncorrelated. The spectra of the original signal can be easily calculated from the resampled data once the spectra of the filter and noise are obtained.

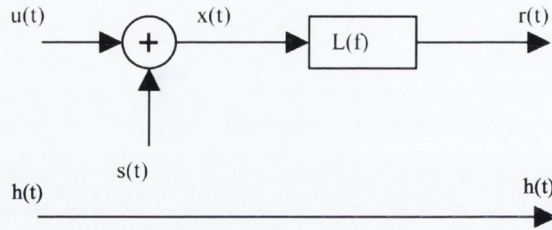


Figure 5.11: LDA and Hot Wire Signals

The spectra of the original signal can be easily calculated from the resampled data once the spectra of the filter and noise are obtained. In this investigation the cross spectra of hot wire and LDA signals is required. The resulting system is shown in figure 5.11. This calculation is made easier if the step noise of the LDA signal is assumed to be completely uncorrelated with the hot wire signal. As was shown by Fitzpatrick and Simon [36] in this case the step noise can be ignored in the cross spectra. As a result only the filter correction is required for these cross spectra.

5.7.3 X-Wire

Of the three measurement techniques employed in this investigation hot wire anemometry is perhaps the most prone to experimental error. The velocity and directional calibrations required for the use of X-wire probes are not trivial and factors such a temperature variation, probe vibration and particle contamination can prove significant.

The x-wire measurements in this investigation were aquired simultaneously with LDA measurements which require the use of seeding particles. If seeding particles condense on the hot wire probes this can effect the heat transfer from the wire and result in an apparently reduced velocity measurement. The seeding fluid chosen for these tests was designed to produce very little condensation. In order to insure that the seeding had no effect on the hot wires tests were conducted with and without seeding and the turbulence statistics and spectra were compared.

In order to validate the hot wire calibration the results were compared with the LDA system as this is regarded as the most accurate measurement of the flow. A

comparison of the mean velocities showed an error of only 1% for the axial component u . In order to further quantify the error the fluctuating velocity component was examined. The irregular sampling rate of the LDA made a direct comparison impossible since very few data point would occur at the exact instant a hot wire measurement was recorded. LDA data points were deemed sufficiently close for a comparison if they occurred within 25% of Δt for the hotwire measurements. This comparison revealed a mean error of 6% on the u' fluctuating velocity and 5% for the v' component.

$$E(t) = \frac{|u'_{ht}(t) - u'_{lda}(\tau)|}{|u'_{lda}(\tau)|} \quad (5.7)$$

$$\tau = t \pm 0.25\Delta t$$

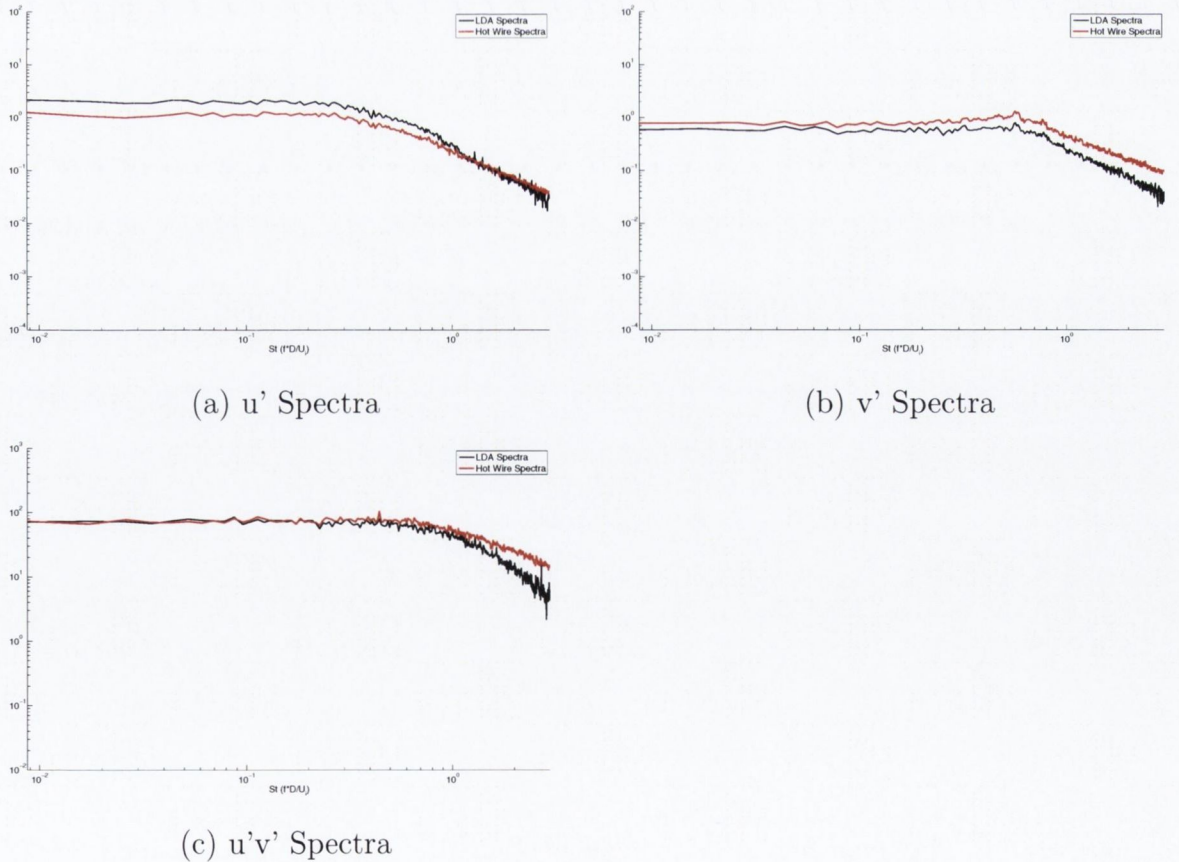


Figure 5.12: Comparison of LDA and Hot Wire Spectra Baseline Nozzle $0.5lc$

A comparison of the calculated X-wire velocity spectra and the LDA results is given in figure 5.12. The difference in amplitude of the spectra can be explained by the error in velocity amplitudes. The other main source of error is at high frequencies where the turbulent scales are comparable in size to the measurement volumes of the probes. The probes can also no longer be said to be approximately coincident in space for these turbulence scales since the the x-wire probe can not intrude into the laser measurement volume and in reality is positioned just outside the beams.

5.7.4 DAQ System

In order to acquire simultaneous measurements from the hot wire and LDA systems a National Instruments DAQ system was used. The National Instruments system consisted of a mainframe *NIPX11044* which housed six eight channel *NIPXI4472B* acquisition cards. Each card is capable of sampling eight voltage inputs simultaneously using *24bit* analogue to digital conversion. The system was connected to a desktop PC via a PCI card. National Instruments Labview software was used to control the mainframe.

A dedicated labview program was written for the two point LDA and hot wire tests. This program acquired the hot wire data and controlled the hot wire probe position via a stepper motor. The LDA hardware provides a BNC analogue out which can be programmed to output $5V$ while measurement is running. This was used as the trigger signal for the Labview program.

5.7.5 Test Matrix

This investigation comprised of two major test campaigns to be outline in the following two chapters. Table 5.2 shows a test matrix for the PIV experiments while table 5.3 shows the test matrix for the LDA and X-wire experiments.

5.7. DATA ACQUISITION AND ERROR ANALYSIS

<i>PIV</i>	<i>0-2 D</i>	<i>2-4 D</i>	<i>4-6 D</i>	<i>6-8 D</i>
Single Jet	2000 PIV Images	2000 PIV Images	2000 PIV Images	2000 PIV Images
N0 Tip	2000 PIV Images	2000 PIV Images	2000 PIV Images	2000 PIV Images
N0 Trough	2000 PIV Images	2000 PIV Images	2000 PIV Images	2000 PIV Images
N2 Tip	2000 PIV Images	2000 PIV Images	2000 PIV Images	2000 PIV Images
N2 Trough	2000 PIV Images	2000 PIV Images	2000 PIV Images	2000 PIV Images
N4 Tip	2000 PIV Images	2000 PIV Images	2000 PIV Images	2000 PIV Images
N4 Trough	2000 PIV Images	2000 PIV Images	2000 PIV Images	2000 PIV Images
N4 Trough	2000 PIV Images	2000 PIV Images	2000 PIV Images	2000 PIV Images
				56000 PIV Images

Table 5.2: PIV Test Matrix

LDA/X-wire	$0.5 L_c$	$0.75 L_c$	$1.0 L_c$	Total Measurements
Single Jet	37 measurements	37 measurements	37 measurements	111 measurements
N0 Tip	37 measurements	37 measurements	37 measurements	111 measurements
N0 Trough	37 measurements	37 measurements	37 measurements	111 measurements
N2 Tip	37 measurements	37 measurements	37 measurements	111 measurements
N2 Trough	37 measurements	37 measurements	37 measurements	111 measurements
N4 Tip	37 measurements	37 measurements	37 measurements	111 measurements
N4 Trough	37 measurements	37 measurements	37 measurements	111 measurements
			21 Tests	777 measurements

Table 5.3: LDA and X-wire Test Matrix

Chapter 6

Nozzle Characterisation

This chapter outlines the changes from the baseline nozzle in order to identify areas of interest for the subsequent two point measurements. The results of the PIV investigations are used to identify changes in jet structure and the nature of the turbulence. In addition LDA spectra are provided to further characterize the nozzles.

6.1 Jet Structure

A whole flow field investigation was undertaken using PIV in order to examine the effects of chevrons on jet structure. The purpose of this study was to identify changes in both jet structure and the basic turbulence properties. In terms of jet structure the primary quantities of interest are potential core length, defined based on a center line velocity $U_c = 0.95U_j$, and shear layer growth indicated by the momentum integral thickness θ . The turbulent properties of interest are u', v', u'^2, v'^2 and $u'v'$.

Due to the complex nature of these nozzle geometries the flow exiting the nozzle is not uniform as differences exist between the tip and trough regions of the chevrons. Quantifying how far downstream these differences persist is a major objective of this study. As a result two series of tests were conducted for each chevron nozzle; the first for a plane in line with the chevron tip and the second with the plane in line with chevron trough. In order to achieve a complete picture of the jet structure measurements were taken in the region of $0 - 8D$ downstream of the nozzle. Due to the limitations on laser power and camera field of view the tests were conducted in

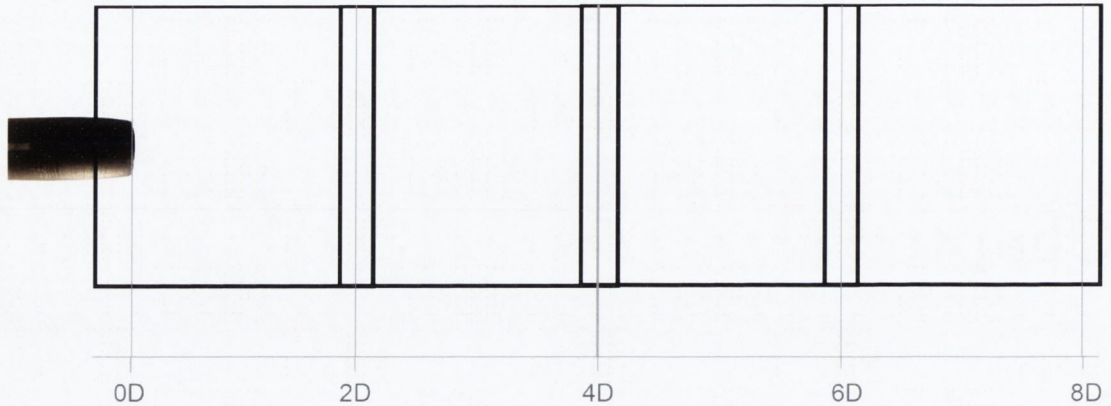


Figure 6.1: Measurement Positions

four overlapping measurement positions. Two thousand PIV image pairs were taken in each position. This resulted in eight thousand PIV images for each of the seven nozzle configurations. Figure 6.1 shows the measurement positions and the nozzle configurations are given in table 6.1. In order to provide as accurate a measurement as possible each series of tests was conducted on a continuous run of the jet. A system of laser pens was employed to reposition the camera without the need to turn off the jet. Due to reflections from the nozzle no vectors could be calculated in the region of $0 - 0.2D$.

The vectors were calculated using multiple passes of the standard PIV cross correlation technique. Three passes were used 64×64 pixels with 50% overlap down to two passes of 32×32 pixels with 75% overlap. The Q peak and median filter post processing techniques were also applied to identify and remove bad vectors. The resulting spatial resolution of the calculated vectors is on the order of $1mm$.

A comparison of the \bar{U} profiles for all nozzles is presented in figure 6.2. The results for each chevron nozzle in both tip and trough configurations are plotted over the baseline single jet profile. As expected the chevrons significantly alter the potential core length and the immersion of the chevrons into the flow has further affected the jet structure.

The three chevron nozzles exhibit difference behavior as the jet evolves. The 0° nozzle shows a widening of the profiles with a larger effect in the trough regions. This

SJ	0-2 D	2-4 D	4-6 D	6-8 D
N0 Tip	0-2 D	2-4 D	4-6 D	6-8 D
N0 Trough	0-2 D	2-4 D	4-6 D	6-8 D
N2 Tip	0-2 D	2-4 D	4-6 D	6-8 D
N2 Trough	0-2 D	2-4 D	4-6 D	6-8 D
N4 Tip	0-2 D	2-4 D	4-6 D	6-8 D
N4 Trough	0-2 D	2-4 D	4-6 D	6-8 D

Table 6.1: Nozzle Configurations

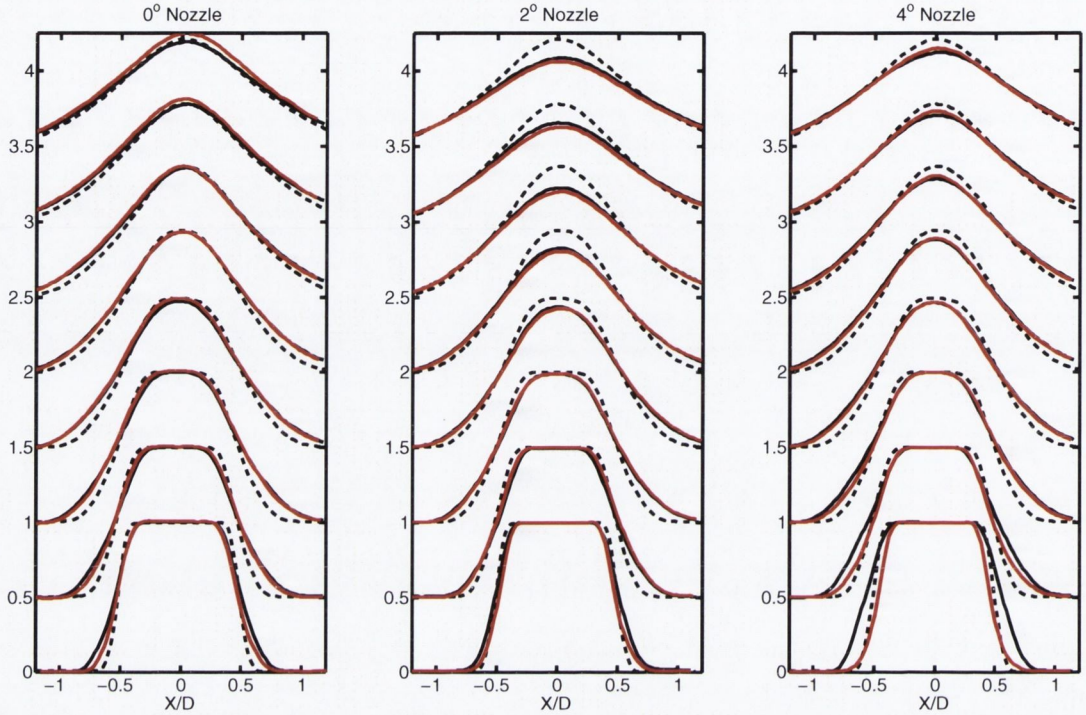
effect extends over the entire jet out to $8D$ downstream. The 2° nozzle shows a less significant widening of the profiles but the centerline velocity has been significantly reduced in the flow region beyond $4D$ downstream. This nozzle also exhibits very little difference between the tip and trough regions of the flow.

Close to the nozzle the 4° nozzle exhibits the largest difference between tip and trough regions. The tip profile is narrower than the baseline case at $1D$ downstream but evolves to be wider from $2D$ onwards. This nozzle exhibits both a significant widening of the profiles and a reduction of the center line velocity as the flow develops. The effects on the centerline velocity are shown by the potential core lengths given in table 6.2.

SJ	4.92D
N0	4.64D
N2	3.80D
N4	4.13D

Table 6.2: Potential Core Length

The axial evolution of the shear layer was measured using the momentum integral thickness θ . The standard formulation was used for the calculation where U denotes the local velocity and U_j the jet velocity.

Figure 6.2: \bar{u}/u_j Profiles 1 – 8D

Red - Chevron Tip. Black - Chevron Trough. Black Dashed - Single Jet

$$\theta = \int_0^\infty \frac{U}{U_j} \left(1 - \frac{U}{U_j}\right) \quad (6.1)$$

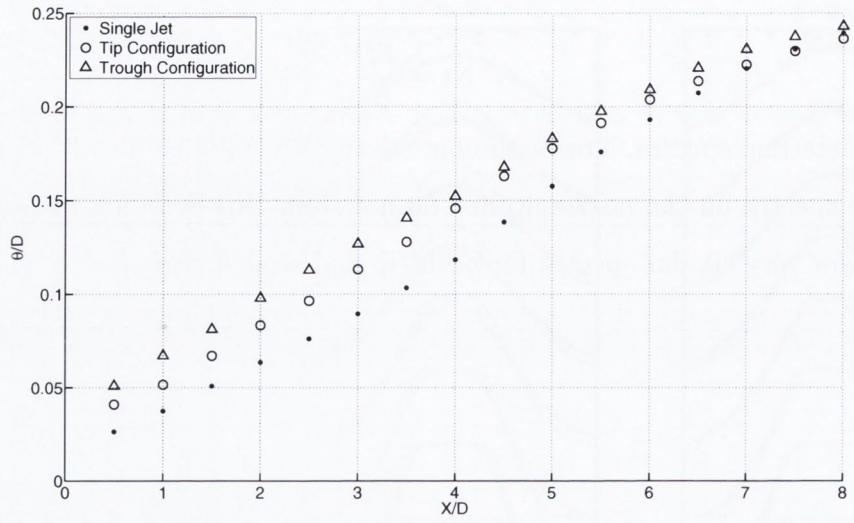
The results for each nozzle in tip and trough configurations are shown against the baseline single jet in figure 6.3. All chevron nozzles show a significant increase in the thickness of the initial shear layer in comparison to the single jet. In addition the trough regions have a thicker initial shear layer than the tip regions. As can be seen in the figures the chevron nozzle shear layers tend to become uniform after approximately $4D$ downstream of the nozzle exit. The wider initial shear layer of all nozzles is in keeping with the widening of the \bar{U} profiles. The 4° tip region has a narrower \bar{U} profile than the baseline case but still exhibits a wider initial shear layer than the baseline. In this case the shear layer has grown inwards to the potential core region.

Turbulence spectra were calculated at two radial locations at the end of the potential core for each nozzle configuration. Measurements were taken on the jet center line and on the nozzle lip line. These spectra are presented as a function of Strouhal Number in figure 6.4.

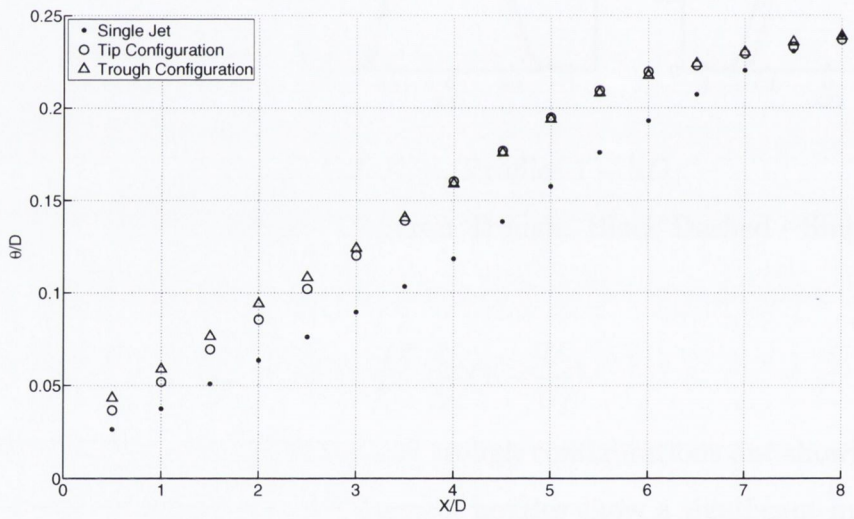
$$St = \frac{fD}{U_j} \quad (6.2)$$

The centerline spectra show a similar Strouhal instability for all nozzles at $St = 0.45$. The spectra on the nozzle lip line do not show this Strouhal instability and all nozzles show very similar spectra for both tip and trough regions.

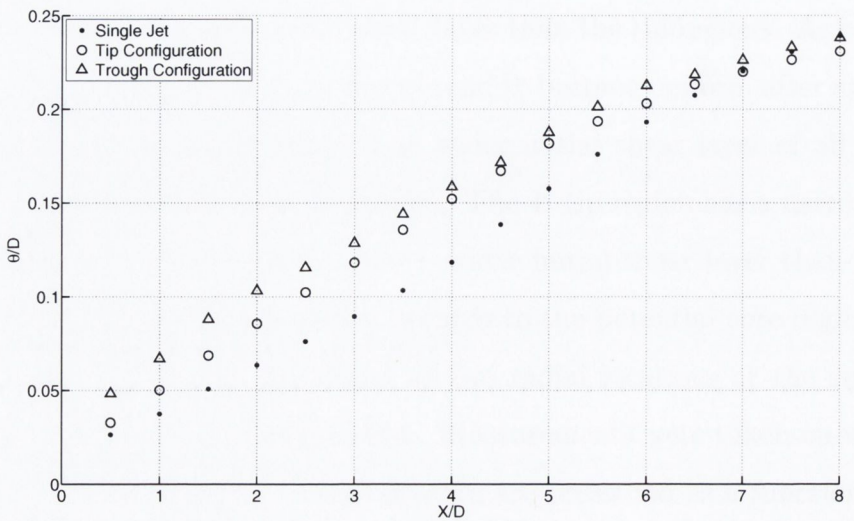
6.1. JET STRUCTURE



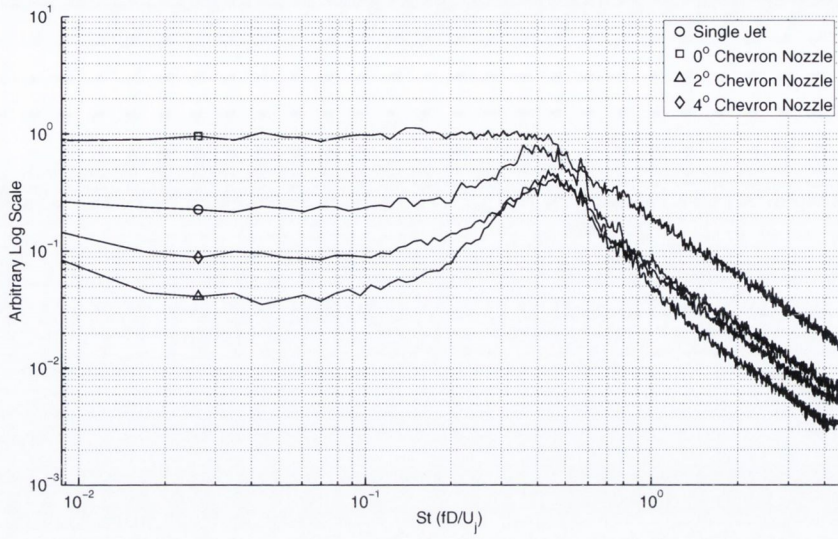
(a) 0° Nozzle



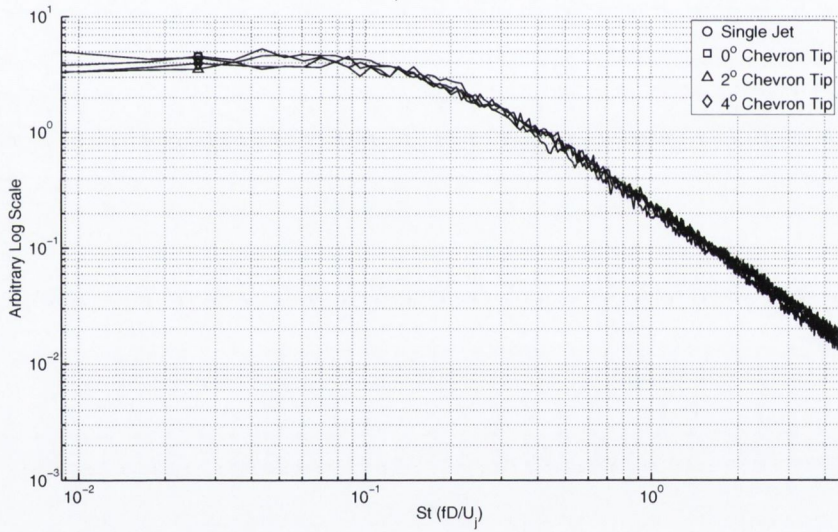
(b) 2° Nozzle



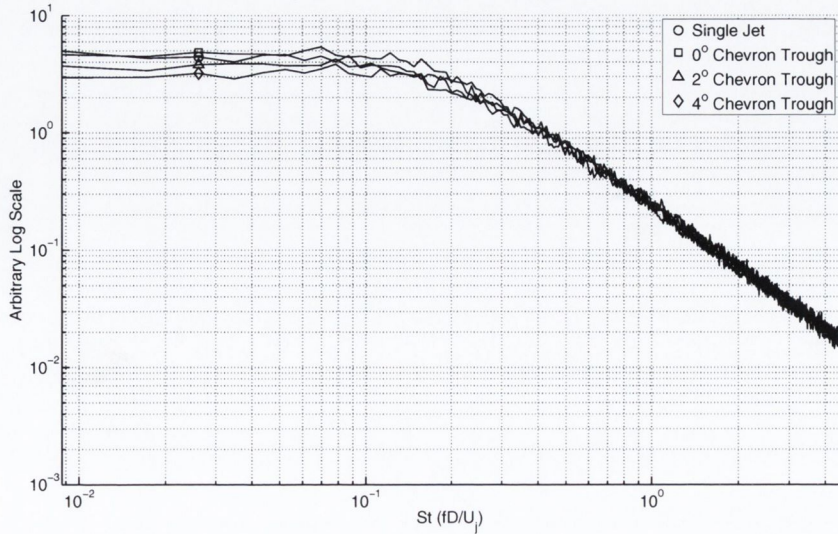
(c) 4° Nozzle



$Y/D = 0$



$Y/D = 0.5$ Chevron Tip



$Y/D = 0.5$ Chevron Trough

Figure 6.4: Hot Wire Spectra

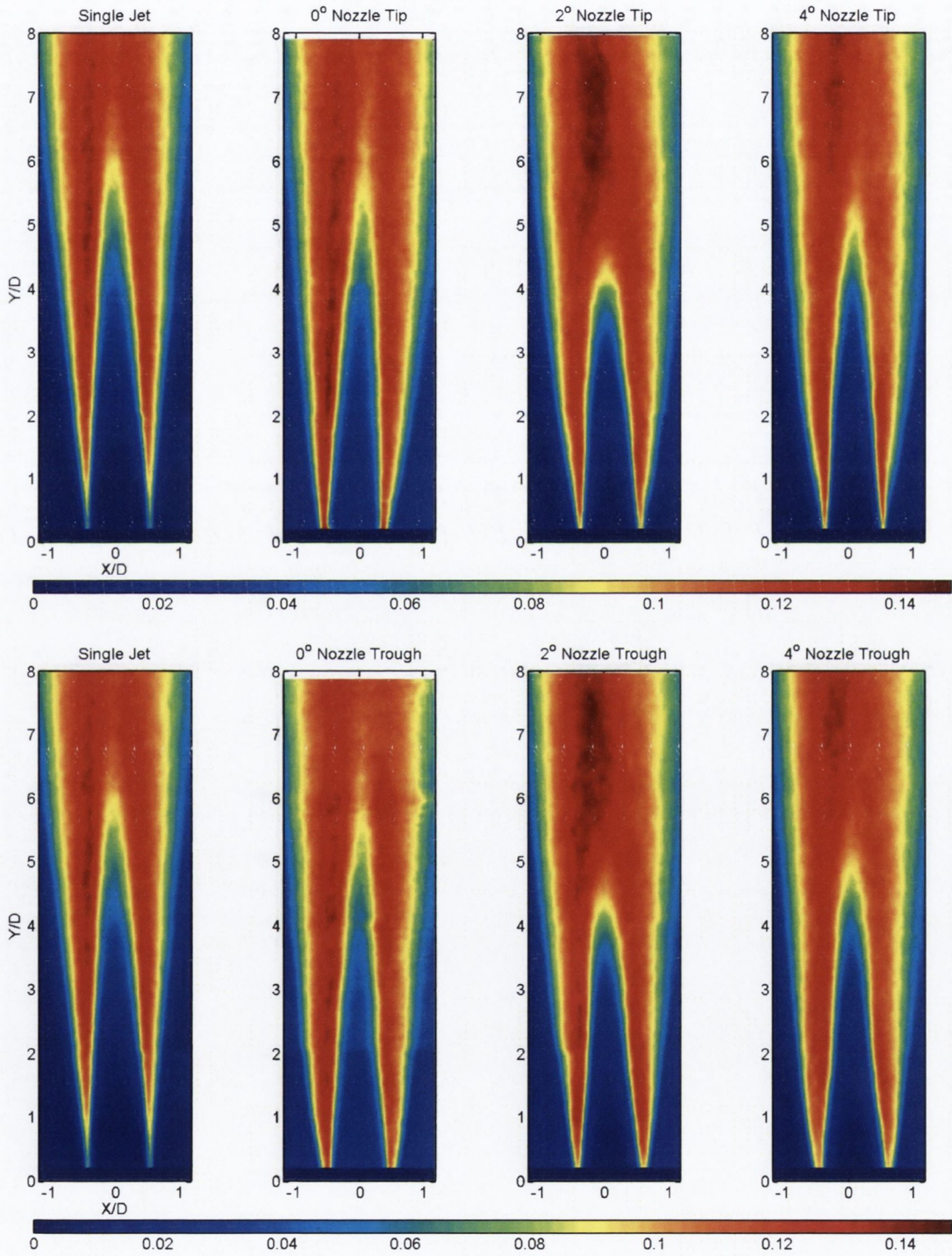
6.2 Turbulence Properties

In order to calculate the turbulence properties the mean values for u and v were calculated using two thousand PIV images for each position. Once the mean had been calculated it was then subtracted from each instantaneous vector field to provide the fluctuating components. This process allowed u', v', u'^2, v'^2 and $u'v'$ to be calculated and averaged. All of these statistics have been normalized using the jet velocity u_j . Due to the large quantity of data involved profiles and surf plots are provided only for the basic turbulence properties u' and v' . All Reynolds stress components are represented using profiles.

The differences between tip and trough configurations are more evident for the turbulence statistics. Surf plots for the regions $0 - 8D$ are given for both tip and trough regions in figures 6.5 and 6.6. The results for the \bar{u} profiles and momentum integral thickness showed alterations to the shear layer thickness and potential core length. These changes are also clearly evident in these plots. The initial shear layers of all chevron nozzles show much higher turbulence intensities with the largest increase for the 0° . Despite this thicker and more intense shear layer the 0° shows only a small 6% decrease in potential core length.

The shape and length of the potential core is more significantly affected by the 2° and 4° nozzles. The tip regions for these nozzles show a narrower initial potential core which mixes with the wider trough region $2D$ downstream of the nozzle exit. This would suggest the chevron penetration has the most significant effect on the potential core length and it is the tip regions which produce a narrowing effect which leads to the length reduction.

These differences can be more clearly seen in the profiles comparison given in figure 6.8. In the region of $0 - 1D$ of the nozzle the chevron nozzles show significantly higher turbulence intensity than the baseline nozzle. However the peak u' turbulence intensity of 16% is similar for all nozzles. The 4° nozzle shows a reduction in v' turbulence beyond the potential core.

Figure 6.5: u'/u_j Tip and Trough Regions

6.2. TURBULENCE PROPERTIES

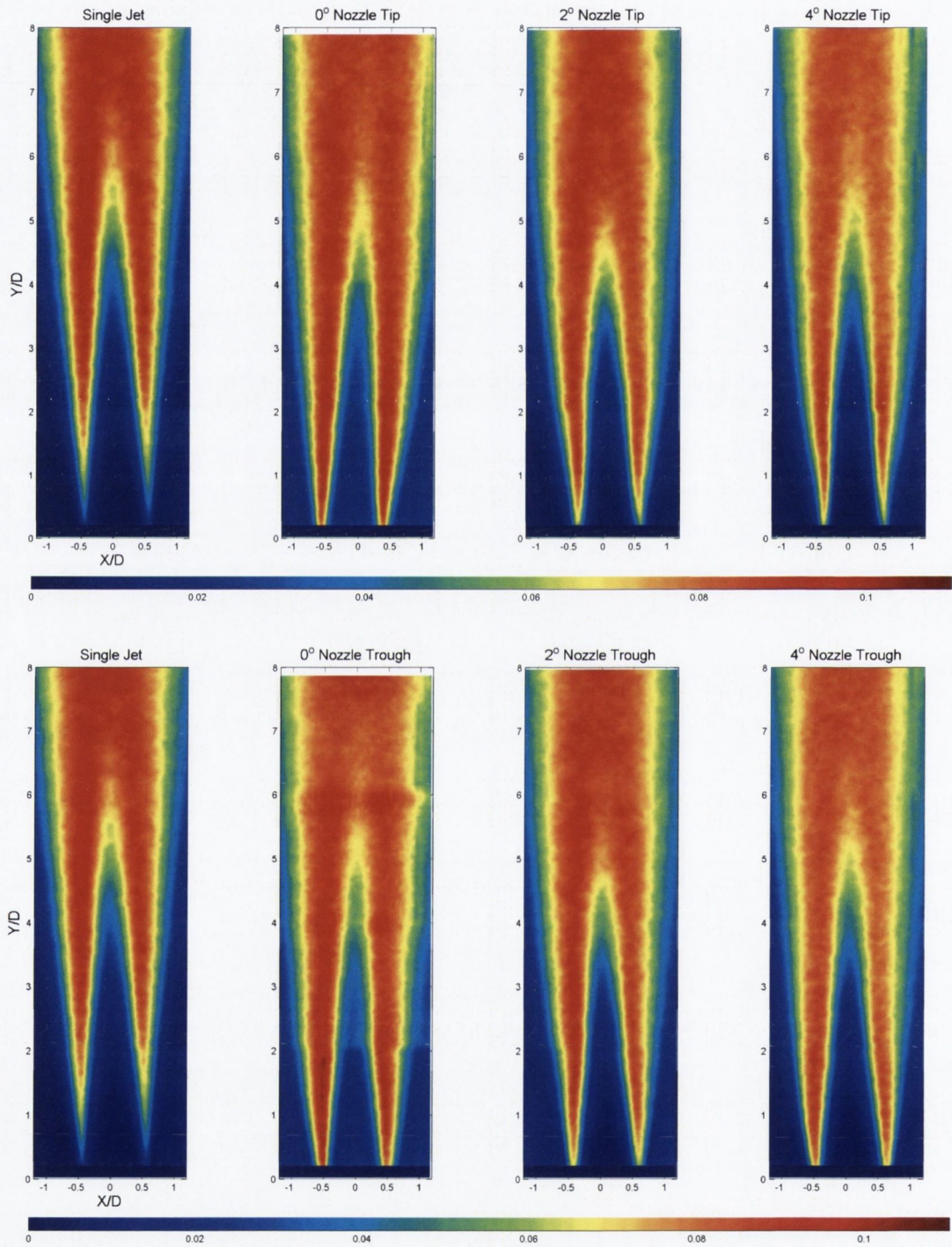
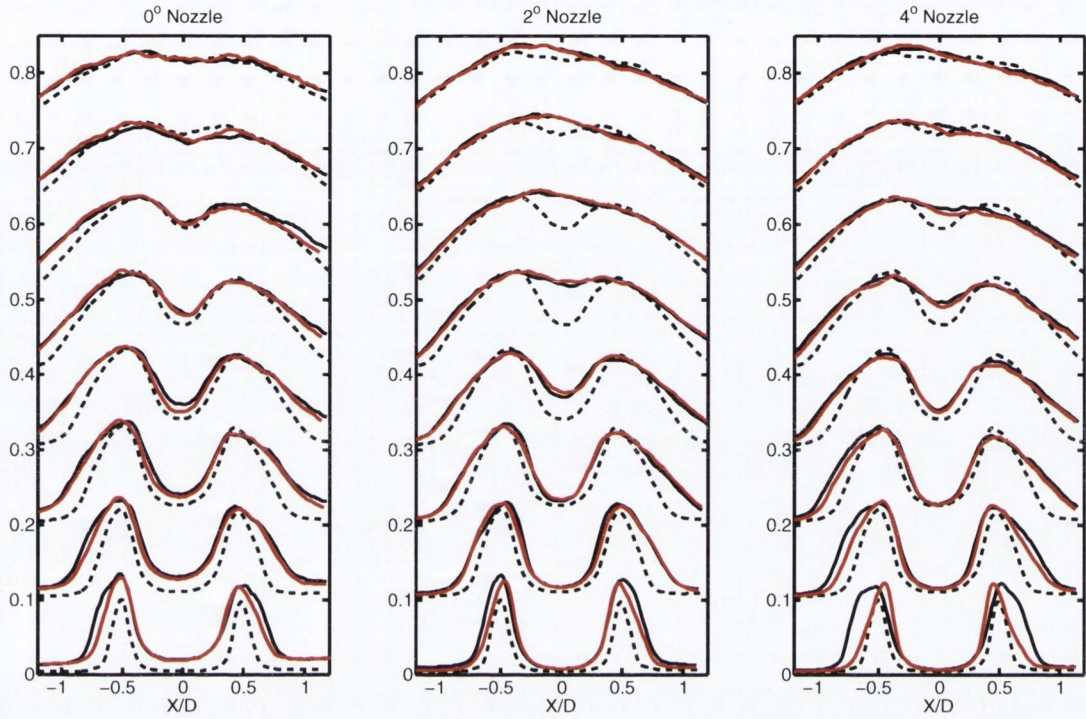
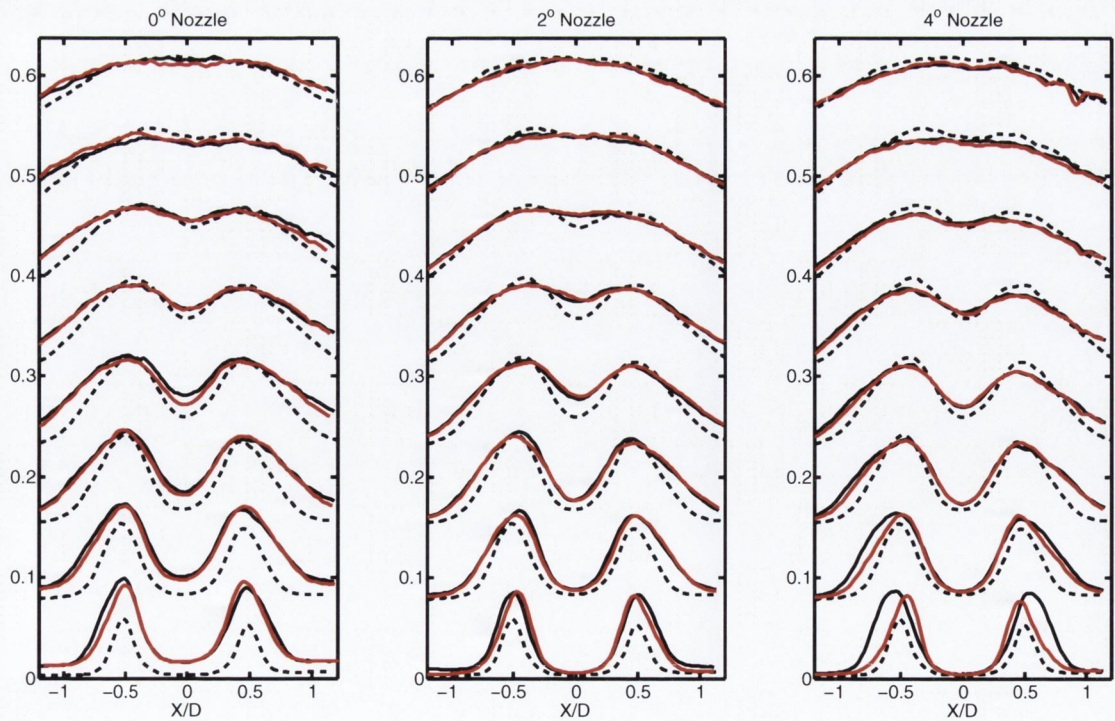


Figure 6.6: v'/u_j Tip and Trough Regions

Figure 6.7: u'/u_j Profiles 1 – 8D

Red - Chevron Tip. Black - Chevron Trough. Black Dashed - Single Jet

Figure 6.8: v'/u_j Profiles 1 – 8D

Red - Chevron Tip. Black - Chevron Trough. Black Dashed - Single Jet

6.2.1 Ratio of Radial to Axial Turbulence Intensity

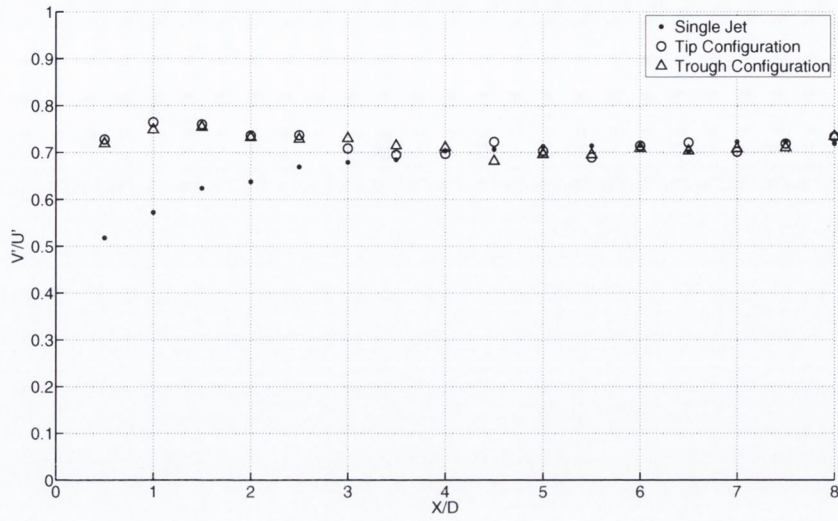
The most significant changes to the basic turbulence properties are within $0 - 2D$ of the nozzles and affect the v' component. In order to demonstrate the change in the nature of the turbulence the ratio of radial to axial components was calculated along the nozzle lip lines. Figure 6.9 show the ratio of turbulence components u' and v' for each chevron nozzle in comparison to the baseline nozzle along the lip line. The chevrons significantly increase the v'/u' ratio in the nozzle region from a value of 50% for the baseline nozzle to values close to 80% for the 0° and 4° nozzles. The ratio of the turbulent component is even higher in the initial region of these two nozzles than it is in the mixing region after the potential core. While the 2° nozzle has higher values than the baseline case for the near nozzle regions these are still lower than the values found downstream in the mixing region.

Chevron nozzles have been shown to suffer from a high frequency penalty despite their overall noise reduction and these results suggests that the radial component of velocity might play a larger role in noise production near the nozzle for chevron designs. While all nozzles show an increase of the v' component near the nozzle there are also significant differences between nozzles.

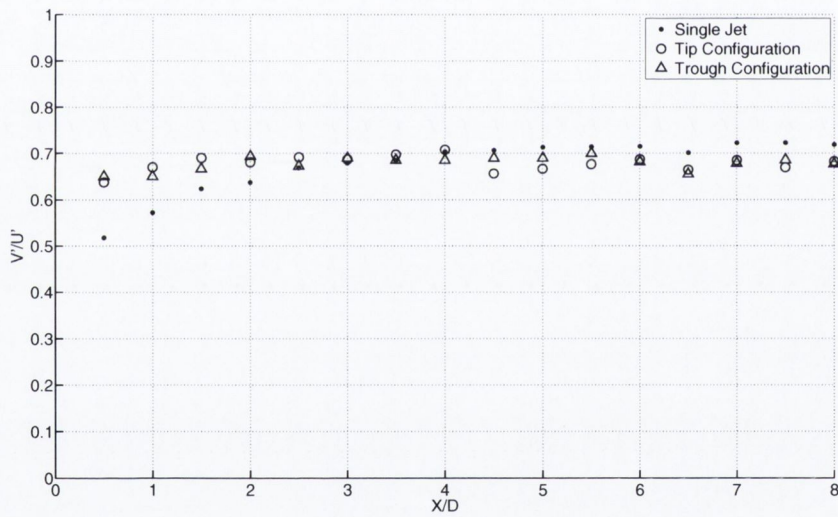
The 0° nozzle shows an increasing v' intensity between $0.5D$ and $1D$ which then falls to the baseline level after $4D$. This nozzle produced the largest increase in v' and the tip and trough regions also show a very similar v'/u' ratio.

The tip and trough regions behaved significantly different for the 4° nozzle. The trough regions exhibit the behavior of the 0° nozzle with a high 80% ratio of the turbulence intensities. The tip region shows the behavior of the 2° nozzle with a v'/u' ratio higher than the baseline case but lower than the ratio in the mixing region downstream of the potential core.

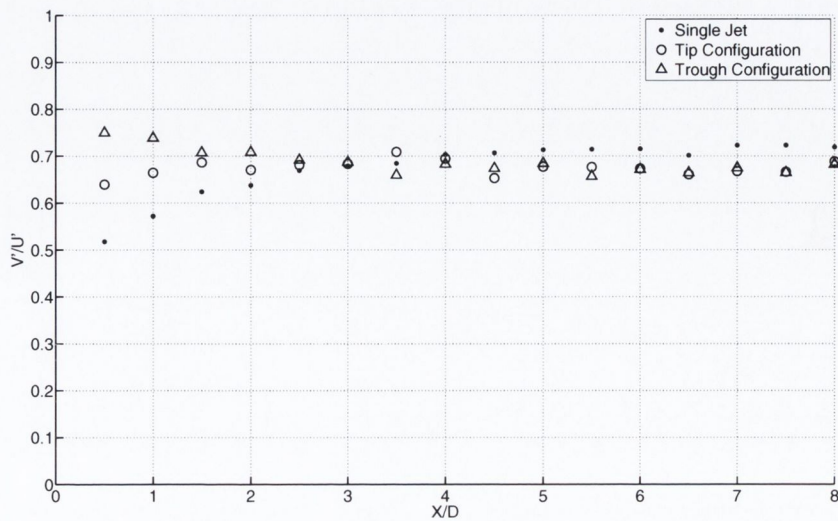
Although the 0° nozzle showed the largest difference in the nozzle region this collapsed to the baseline case after $4D$. The 2° and 4° nozzles do not collapse onto the baseline nozzle and the turbulence ratio is actually lower than the baseline case after $4D$.



(a) 0° Nozzle



(b) 2° Nozzle



(c) 4° Nozzle

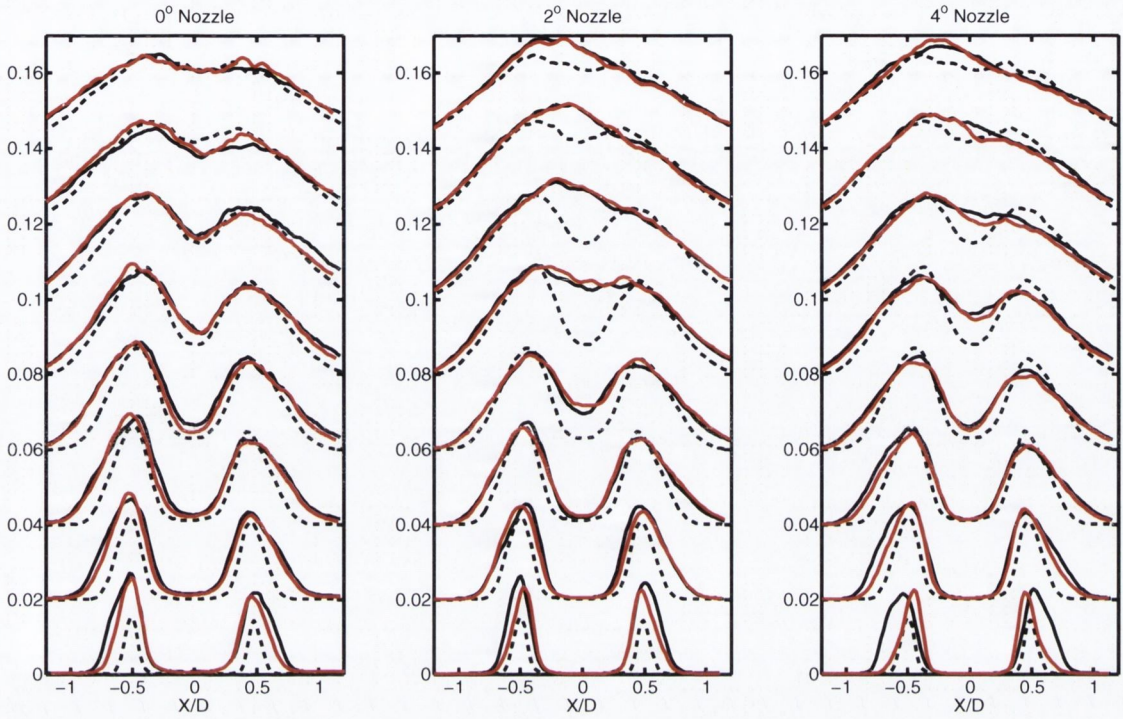
Figure 6.9: Ratio of Radial to Axial Turbulence Intensities v'/u'

6.2.2 Reynolds Stresses

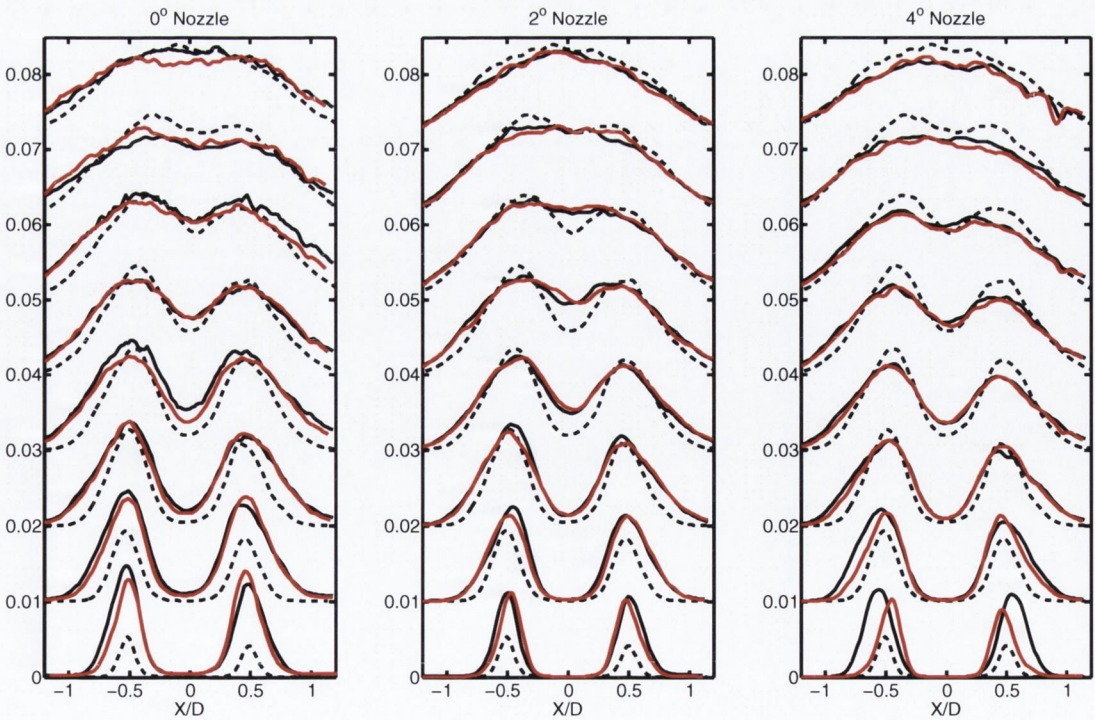
It has long been understood that the Reynolds stresses play a larger role in noise production than the basic turbulence statistics of u' and v' . An examination of how the stresses u'^2 , v'^2 and $u'v'$ change was conducted along with the effects on vorticity. As is expected from the previous results the most significant effects are present near the nozzles. The u'^2 and v'^2 profiles are given in figures 6.10 and 6.11. The nozzle region shows significantly higher values which then reduce to the baseline case after approximately $4D$ downstream. As before the nozzle regions show a wider shear layer apart from the 4° nozzle which has a tip region narrower than the baseline. The 2° nozzle again shows the smallest variation between tip and trough regions.

Beyond $3D$ downstream of the nozzle the u'^2 and v'^2 stresses are significantly higher along the centerline for the 2° and 4° nozzles due to the shorter potential core lengths.

The v'^2 term again shows the greatest increase over the single jet case in the nozzle region. In order to demonstrate this further figure 6.12 shows how the ratio of v'^2 to u'^2 develops along the nozzle lip line. Similarly to before the 0° nozzle showed the largest difference in the nozzle region and this collapsed to the baseline case after $4D$. The 2° and 4° nozzles do not collapse onto the baseline nozzle and the ratio is again lower than the baseline case after $4D$. As before the 4° nozzle shows two clearly different regimes between the tip and trough regions with the trough behaving similarly to the 0° nozzle and the tip similarly to the 2° .

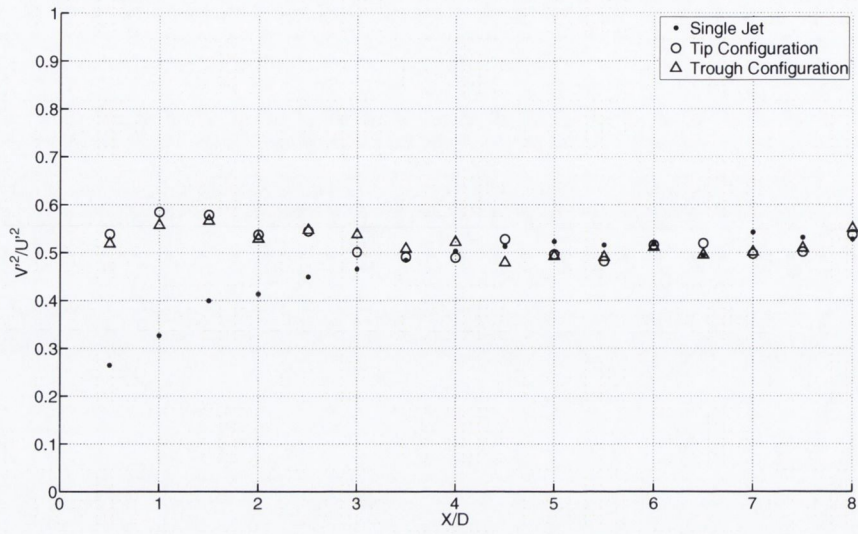
Figure 6.10: u'^2/u_j^2 Profiles 1 – 8D

Red - Chevron Tip. Black - Chevron Trough. Black Dashed - Single Jet

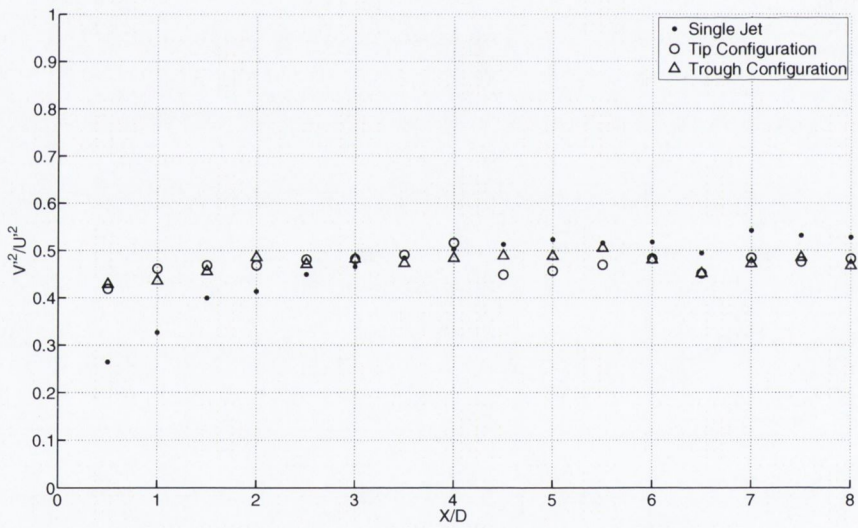
Figure 6.11: v'^2/u_j^2 Profiles 1 – 8D

Red - Chevron Tip. Black - Chevron Trough. Black Dashed - Single Jet

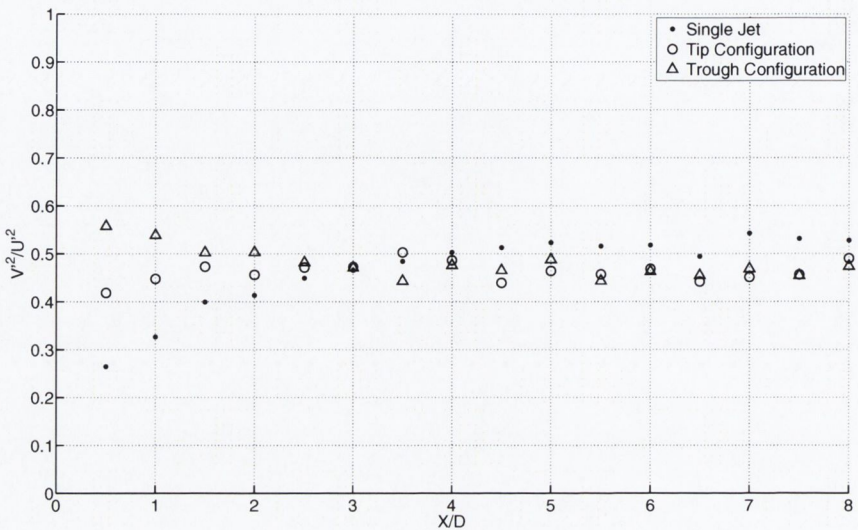
6.2. TURBULENCE PROPERTIES



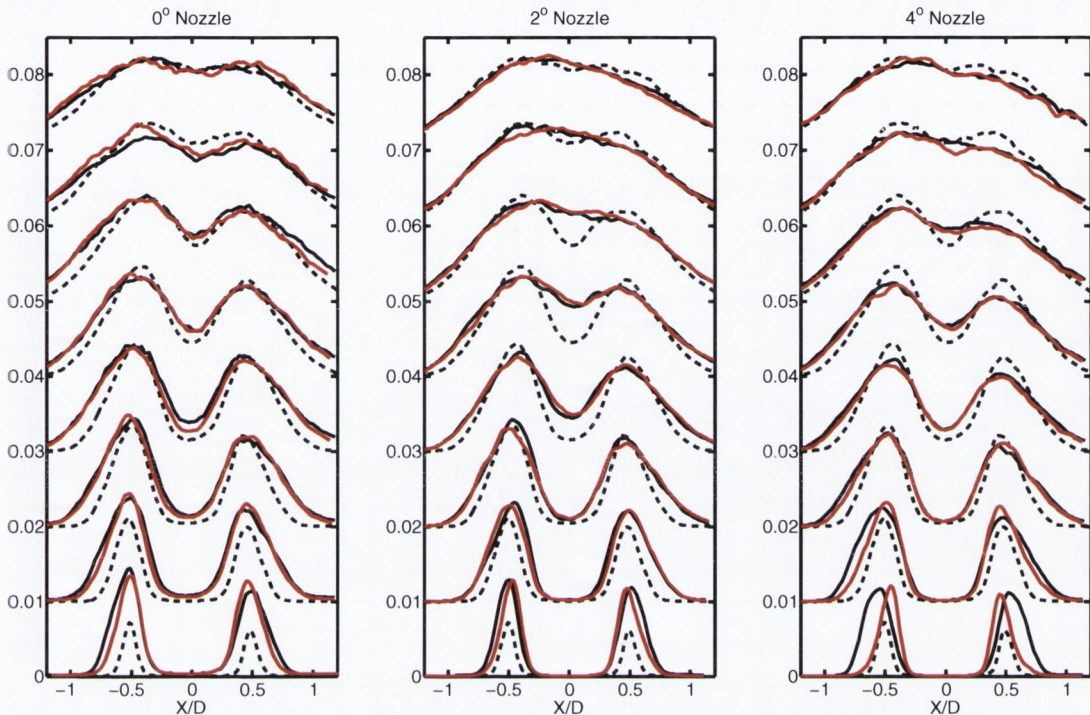
(a) 0° Nozzle



(b) 2° Nozzle



(c) 4° Nozzle

Figure 6.13: $u'v'/u_j^2$ Profiles 1 – 8D

Red - Chevron Tip. Black - Chevron Trough. Black Dashed - Single Jet

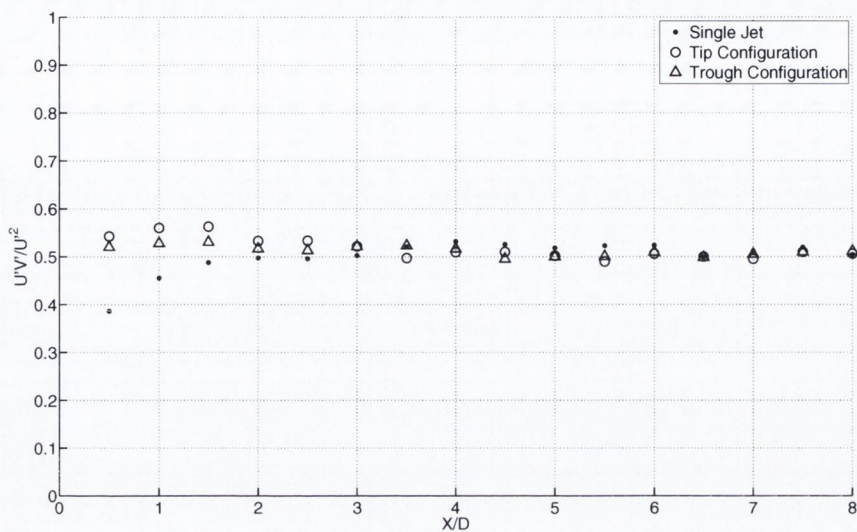
Similar results were found for the $u'v'$ component of the Reynolds stress. The $u'v'$ profiles are given in figure 6.13. The most significant changes are again in the nozzle regions which show higher values in comparison to the baseline nozzle. The most noticeable change here is in the ratio of the $u'v'$ to u'^2 Reynolds stress. Figure 6.14 shows how the ratio of $u'v'$ to u'^2 develops along the nozzle lip line. As can be seen from the figure the ratio close to the nozzles is very close to the levels found in the mixing region. This is a result of the rapid evolution of the shear layer for the chevron nozzles and the increased v' component close to the nozzle exit.

The effects on vorticity were examined to provide a final additional insight into the effects of the chevrons. These results can be seen in figures 6.15 and 6.16. The levels of vorticity are lower for the chevron nozzles as a result of the wider shear layers. A narrower more intense region of vorticity can be seen around the nozzle tips. The most intense vorticity apart from the baseline case is seen for the 4° nozzle tip region. Here the vorticity almost reaches the levels in the base line case.

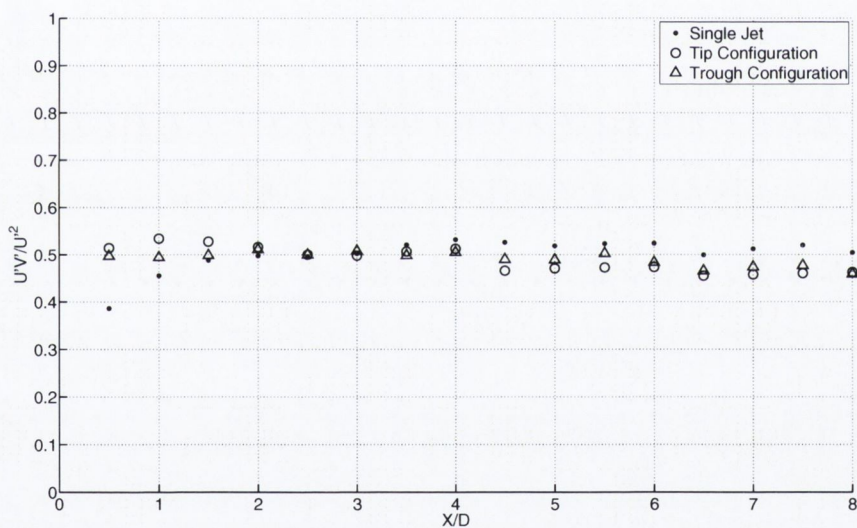
The 2° shows the smallest variation between tip and trough regions but the trough

regions of vorticity are still slightly less intense and wider. This nozzle also shows the lowest levels beyond $4D$ downstream of the nozzle as this nozzle had the shortest potential core. The 0° nozzle shows the lowest levels of vorticity close to the nozzle with the most significant widening of the regions of vorticity.

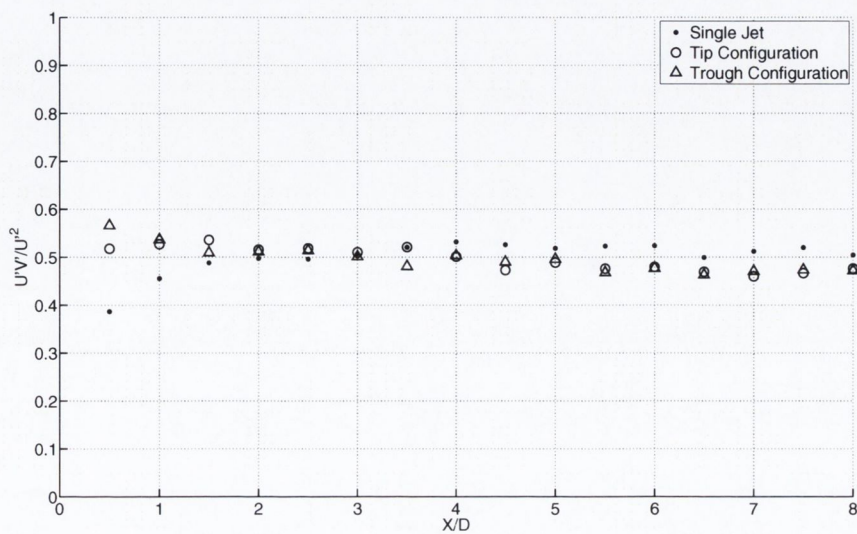
As found previously the 4° nozzle tip region behaves similarly to the 2° nozzle and the trough region behaves similarly to the 0° nozzle.



(a) 0° Nozzle



(b) 2° Nozzle



(c) 4° Nozzle

Figure 6.14: Ratio of Reynolds Stresses $u'v'/u'^2$

6.2. TURBULENCE PROPERTIES

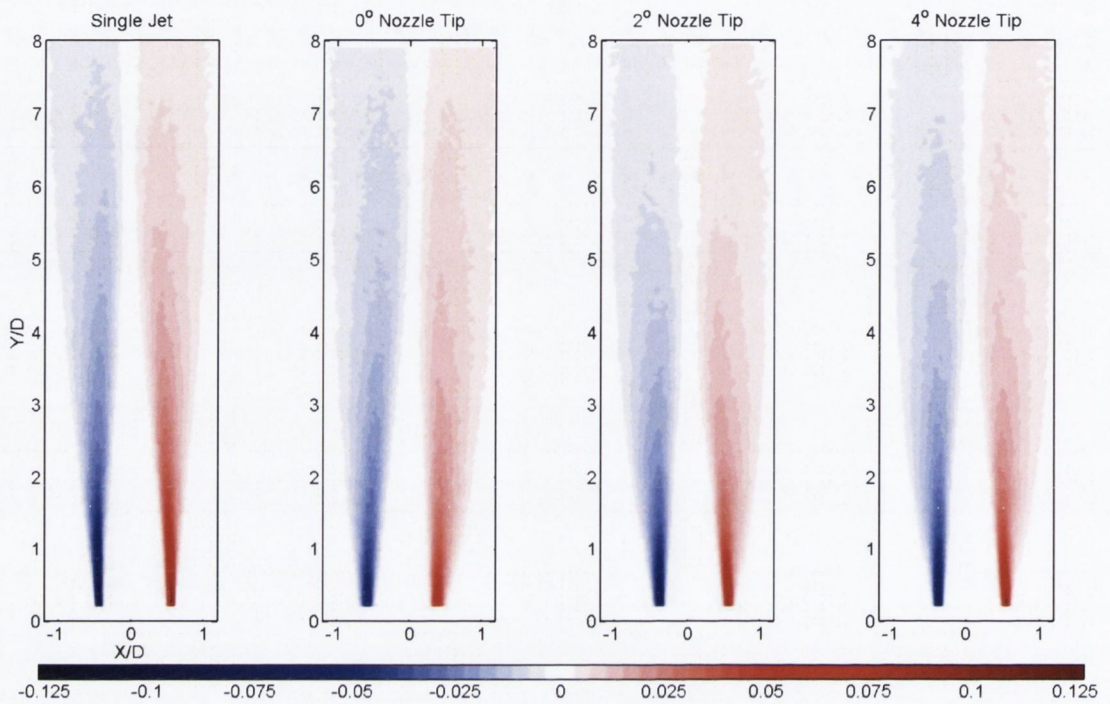


Figure 6.15: Vorticity Tip Regions

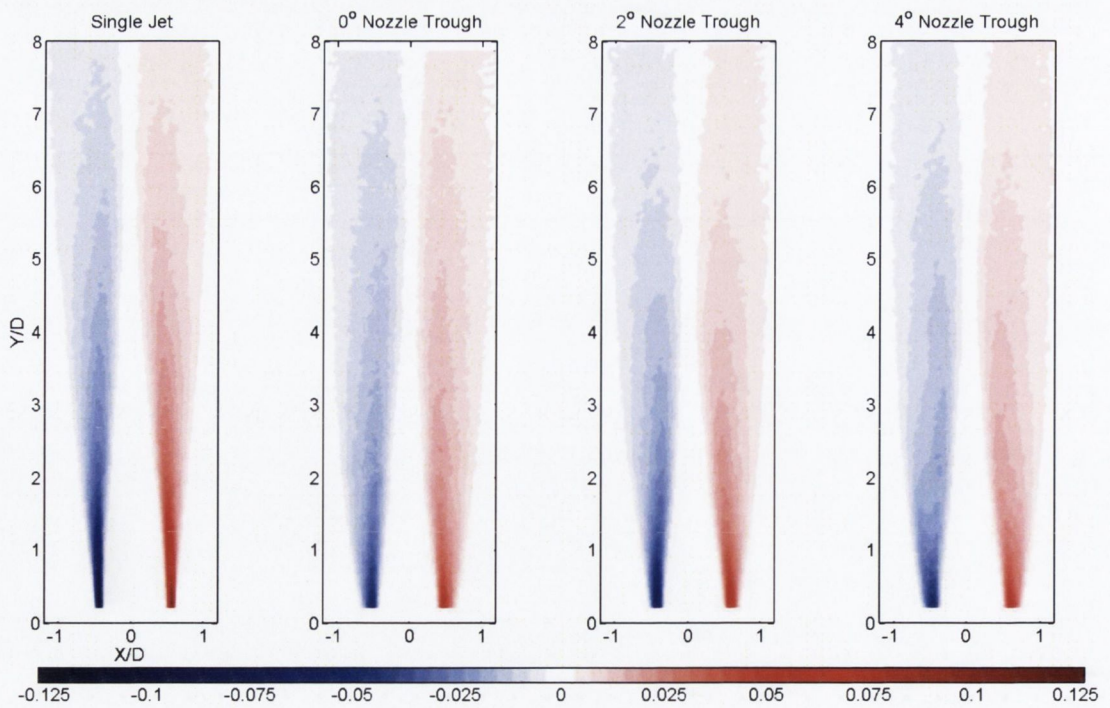


Figure 6.16: Vorticity Trough Regions

6.3 Discussion

Two effects on jet structure were identified for the chevron nozzle designs.

- Widening of the shear layer
- Shortening of the potential core

The principle effect on the turbulence properties was found to effect the v' component and was most significant in the nozzle region. While all nozzles exhibited these features to some extent there were important differences between nozzles.

0° Nozzle This nozzle did not significantly effect the potential core length showing a reduction of less than 6%. This nozzle showed the thickest initial shear layer which increased by almost 100% from the baseline case for the trough region. The largest increase in the v' turbulence in the initial region was also observed for this nozzle as the v'/u' ratio increased from 50% for the baseline nozzle to 80% for this nozzle. This collapsed to the baseline after $4D$.

2° Nozzle This nozzle showed the most dramatic changes to the potential core length with a reduction of over 22%. This significantly lowered the centerline velocity and increased the turbulence properties well above the baseline case beyond $4D$. This nozzle showed the lowest tip to trough region differences and while both regions showed a wider shear layer than the baseline case the increase was less significant than the 0° nozzle. This nozzle also increased the v'/u' ratio in the initial region but the values were still below those found in the mixing region after the potential core.

4° Nozzle This nozzle showed the largest tip to trough differences. The trough region behaves very similarly to the 0° nozzle while the tip region is similar to the 2° nozzle. After $4D$ these differences have mixed and the flow exhibits the behavior of both other nozzles with a wider shear layer and lower centerline velocity.

The 0° nozzle demonstrated that the addition of chevrons to a nozzle has strong effects on the shear layer and v' turbulence. However the mechanisms involved change once

the chevrons are immersed into the flow. The 2° nozzle appears to have a balance between tip and trough regions working together to significantly alter the potential core length while having less of an impact on the shear layer and v' turbulence. Beyond this low angle of immersion the tip and trough regions begin to behave very differently. For the 4° nozzle the trough regions revert to the behavior found in the 0° nozzle with significant effects on the shear layer and v' turbulence. The tip regions continue to behave as the 2° nozzle and lead to a shortening of the potential core.

A possible explanation of this may be found in the depth of penetration of the chevrons. For the 2° nozzle only the front face of the chevrons penetrates into the flow where as both the front and back faces of the chevrons are immersed into the flow in the 4° nozzle. This may imply that the mechanisms involved in chevron immersion are more efficient when the flow is not forced around the back face of the chevron. It has been suggested that the penetration of chevrons into the flow produces pairs of counter rotating vortices from the chevron tips and the formation and propagation of these vortices may be adversely affected by the flow around the back face of the chevrons.

Chapter 7

Two Point Statistics

Following on from the preliminary PIV work outlined in chapter 6 two point statistics were calculated from LDA and X-wire measurements. The results of these two component tests are presented here. The tests were conducted at three positions along the nozzle lip line for each nozzle $50\%L_c$, $75\%L_c$ and $100\%L_c$ where L_c is the potential core length. Each test consisted of thirty seven measurement positions. For all tests the LDA probe was held stationary and the hot wire position controlled via a traversing system. The hot wire was stepped back from the LDA with an initial spacing of $1mm$ increasing to $2mm$ after $0.2D$ downstream of the LDA and $5mm$ between $0.8D$ and $2.5D$ downstream. Figure 7.1 shows the test locations for the baseline nozzle.

Due to the differences between tip and trough regions identified during the PIV investigation two sets of measurements were required for each chevron nozzle. The chevron nozzle tests were conducted at equivalent positions to the baseline with one set of measurements aligned with a chevron tip and the second set aligned with a chevron trough. From these tests the axial length scales and convection speeds for the u' , v' , u'^2 , v'^2 and $u'v'$ components were calculated. As outlined in chapter 3 both the traditional and frequency dependent statistics were calculated.

Due to the large quantity of data the frequency dependent length scales for $50\%L_c$ and $100\%L_c$ positions are presented here and $75\%L_c$ results are included in Appendix A. The frequency dependent length scales are non-dimensionalised using the nozzle diameter and presented as a function of Strouhal number.

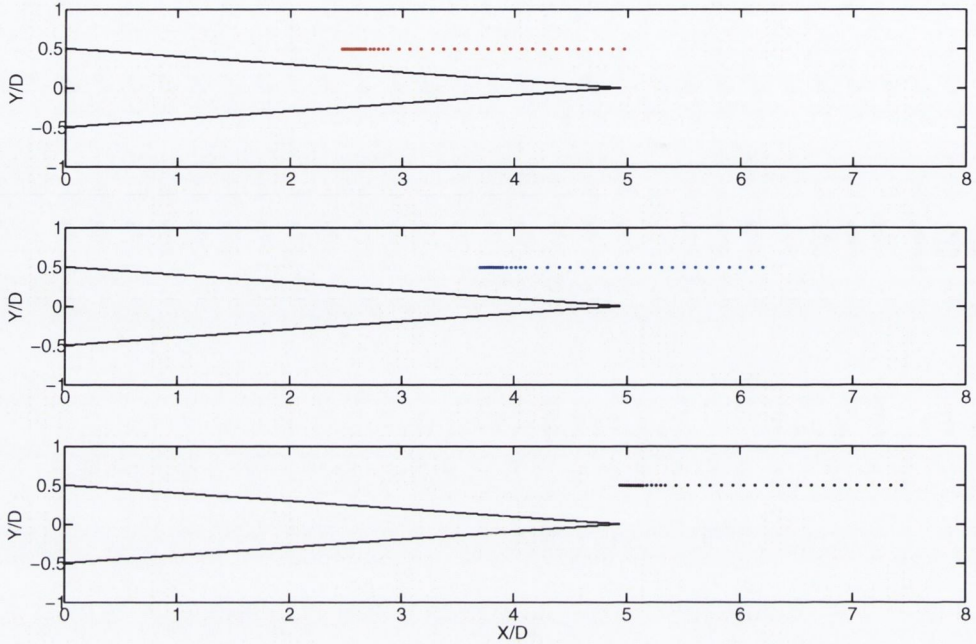


Figure 7.1: Two Point Measurement Positions Baseline Nozzle

$$St = \frac{fD}{U_j} \tag{7.1}$$

7.1 Bulk Length Scales

7.1.1 u' and v' Length Scales

Tables 7.1 to 7.3 show the length scales and convection speed for the u' and v' components. Table 7.1 shows the u' and v' component length scales at the $50\%L_c$ position. The most significant changes from the baseline nozzle are found in the 0° chevron nozzle. There is a dramatic increase to all the length scales with a larger increase in the tip region. The v' component is also effected more strongly than the u' component. The v' fixed length scale is increased by 36% for the tip region where as the u' component is increased by 26%. The 2° nozzle behaves quite differently. For the u' component the tip region length scales are larger than the trough region length scales. Generally the tip region length scales are larger than the baseline values while the

trough region length scales are lower than the baseline values. The opposite trend is observed for the v' length scales and these are larger in the trough region than the tip region. The 4° is very similar to the 2° nozzle but the values are significantly closer to the baseline values. Despite this the same patterns can be observed.

Table 7.2 shows the u' and v' component length scales at the $75\%L_c$ position. As with the previous position the most significant changes from the baseline values are found for the 0° nozzle. All length scales show a significant increase however the difference between tip and trough regions has decreased substantially. Several of the trough region length scales are now larger than the tip region values. The u' length scales for the 2° and 4° nozzles still show an increase over the baseline for the tip regions and a decrease in the trough regions. Unlike the previous position all v' length scales, with the exception of the fixed axis length scale for the 4° nozzle, are lower than the baseline values. The tip region v' length scales are also larger than the trough region values of for these nozzle.

Table 7.3 shows the u' and v' component length scales at the $100\%L_c$ position. The 0° nozzle length scales are still increased for this position but the difference from the baseline values is less than for the previous positions. The values for tip and trough regions are almost equal in this position. The v' length scales are decreased below the baseline values for both the 2° and 4° nozzles. The u' length scales are still decreased compared to the baseline for the 2° nozzle but are increased for the 4° nozzle.

7.1. BULK LENGTH SCALES

Table 7.1: u' and v' Length Scales and Convection Speed $0.5L_c$

$0.5 L_c$	L_c	Fixed Axis		Moving Axis		Convection Speed	
		u' (mm)	v' (mm)	u' (mm)	v' (mm)	u' (m/s)	v' (m/s)
SJ	4.92D	7.96	4.54	27.06	19.60	41.95	52.63
N0 Tip	4.64D	10.10	6.18	38.90	25.18	44.36	50.49
N0 Trough	4.64D	9.36	5.63	35.24	22.68	41.11	43.25
N2 Tip	3.80D	8.41	4.00	27.01	16.94	41.67	51.19
N2 Trough	3.80D	7.66	4.34	26.82	17.88	40.60	41.60
N4 Tip	4.13D	8.71	4.48	28.06	20.28	40.92	41.67
N4 Trough	4.13D	7.43	4.69	26.09	18.10	38.94	36.68

Table 7.2: u' and v' Length Scales and Convection Speed $0.75L_c$

$0.75 L_c$	L_c	Fixed Axis		Moving Axis		Convection Speed	
		u' (mm)	v' (mm)	u' (mm)	v' (mm)	u' (m/s)	v' (m/s)
SJ	4.92D	10.60	5.82	37.53	23.22	40.48	43.69
N0 Tip	4.64D	12.48	6.91	47.41	27.85	42.84	44.81
N0 Trough	4.64D	13.12	6.92	48.12	26.28	40.74	43.14
N2 Tip	3.80D	10.90	5.28	38.49	19.96	40.15	41.81
N2 Trough	3.80D	9.74	5.13	35.91	18.56	38.53	41.67
N4 Tip	4.13D	10.96	5.88	39.46	23.05	39.44	37.81
N4 Trough	4.13D	9.84	5.43	35.95	22.85	38.90	39.10

Table 7.3: u' and v' Length Scales and Convection Speed $1.0L_c$

$1.0 L_c$	L_c	Fixed Axis		Moving Axis		Convection Speed	
		u' (mm)	v' (mm)	u' (mm)	v' (mm)	u' (m/s)	v' (m/s)
SJ	4.92D	13.60	7.19	47.06	27.14	39.73	40.16
N0 Tip	4.64D	15.45	7.88	55.92	31.04	41.44	43.58
N0 Trough	4.64D	15.86	7.72	56.20	30.62	40.18	40.95
N2 Tip	3.80D	13.13	5.91	46.13	22.29	38.48	39.45
N2 Trough	3.80D	12.06	6.09	43.57	22.74	38.64	40.28
N4 Tip	4.13D	13.64	6.55	48.05	25.03	37.40	37.19
N4 Trough	4.13D	13.81	6.67	49.78	23.96	38.74	38.87

7.1.2 u'^2 and v'^2 Length Scales

Tables 7.4 to 7.6 show the length scales and convection speed for the u'^2 and v'^2 components. Table 7.4 shows the nozzles at $50\%L_c$ as with the previous results the 0° chevron nozzle shows the largest difference from the baseline values. All length scales show a significant increase over the baseline with a larger increase in the tip region. The increase is more significant for the v'^2 length scales which show an increase of up to 43%. The 2° nozzle length scales are all decreased from the baseline values with the exception of the moving axis length scale for the tip region which shows an increase. The u'^2 length scales are larger for the trough regions while the v'^2 length scales are larger for the tip regions of this nozzle. All of the length scales for the 4° nozzle are larger in the tip region than the trough region and the values are either close to the baseline or show an increase.

Table 7.5 shows the length scales for the nozzles at $75\%L_c$. The 0° nozzle length scales are still significantly increased over the baseline. The trough region length scales are now larger than the tip region with the exception of the u'^2 moving axis length scale. The 2° nozzle length scales are generally lower than the baseline values with the exception of the tip region moving axis length scales. The tip region length scales are all larger than the trough region in this position. The 4° nozzle behaves similarly to the 2° nozzle and the length scales are generally lower than the baseline with the exception of the tip region moving axis length scales. All of the tip region length scales are larger than the trough region.

Table 7.6 shows the length scales for the nozzles at $100\%L_c$. The 0° nozzle length scales are still increased but the v'^2 length scales in particular are now very close to the baseline values. For this position the u'^2 length scales are more strongly affected than the v'^2 . Tip and trough region length scales are also very similar. For the 2° nozzle the tip and trough region v'^2 length scales are approximately equal but the tip region u'^2 length scales are still larger than those in the trough region. The values are generally a reduction of those of the baseline nozzle. The u'^2 length scales for the 4° nozzle show a slight increase from the baseline values and the v'^2 length scales show a slight decrease. Tip and trough region length scales are very similar at this position.

7.1. BULK LENGTH SCALES

Table 7.4: u'^2 and v'^2 Length Scales and Convection Speed $0.5L_c$

0.5 L_c	L_c	Fixed Axis		Moving Axis		Convection Speed	
		u'^2 (mm)	v'^2 (mm)	u'^2 (mm)	v'^2 (mm)	u'^2 (m/s)	v'^2 (m/s)
SJ	4.92D	4.05	2.66	9.25	5.79	37.31	53.76
N0 Tip	4.64D	4.80	3.37	13.49	8.28	37.21	56.65
N0 Trough	4.64D	4.54	3.37	11.92	7.26	27.93	58.16
N2 Tip	3.80D	3.72	2.49	8.83	6.39	48.54	50.07
N2 Trough	3.80D	3.84	2.42	9.01	5.72	21.32	28.61
N4 Tip	4.13D	4.00	2.77	10.48	7.67	45.08	41.83
N4 Trough	4.13D	3.75	2.53	9.67	5.76	27.13	28.71

Table 7.5: u'^2 and v'^2 Length Scales and Convection Speed $0.75L_c$

0.75 L_c	L_c	Fixed Axis		Moving Axis		Convection Speed	
		u'^2 (mm)	v'^2 (mm)	u'^2 (mm)	v'^2 (mm)	u'^2 (m/s)	v'^2 (m/s)
SJ	4.92D	5.23	3.47	13.36	8.09	49.92	53.34
N0 Tip	4.64D	5.80	3.92	17.02	10.00	40.34	54.17
N0 Trough	4.64D	6.01	4.20	16.85	10.18	47.05	54.99
N2 Tip	3.80D	4.97	3.14	13.77	8.32	41.84	47.16
N2 Trough	3.80D	4.67	2.99	12.58	7.11	31.81	56.16
N4 Tip	4.13D	5.04	3.43	14.62	8.47	36.52	45.84
N4 Trough	4.13D	4.67	3.03	13.39	7.99	34.55	51.84

Table 7.6: u'^2 and v'^2 Length Scales and Convection Speed $1.0L_c$

1.0 L_c	L_c	Fixed Axis		Moving Axis		Convection Speed	
		u'^2 (mm)	v'^2 (mm)	u'^2 (mm)	v'^2 (mm)	u'^2 (m/s)	v'^2 (m/s)
SJ	4.92D	6.53	4.40	16.52	10.00	47.36	50.15
N0 Tip	4.64D	7.16	4.69	20.84	11.88	44.69	51.04
N0 Trough	4.64D	7.19	4.77	19.93	11.95	44.52	48.71
N2 Tip	3.80D	6.33	3.60	16.76	8.79	44.63	50.41
N2 Trough	3.80D	5.49	3.66	15.50	8.79	44.57	50.83
N4 Tip	4.13D	6.66	3.96	17.87	9.98	44.04	49.81
N4 Trough	4.13D	6.78	4.01	18.01	9.47	45.71	46.65

7.1.3 $u'v'$ Length Scales

Table 7.7 shows the $u'v'$ length scales for the nozzles at $50\%L_c$. All of the nozzle show an increase to the length scales above the baseline values for both tip and trough regions. Tip region length scales are larger than the trough region and the largest increase is found for the 0° nozzle.

Table 7.8 shows the $u'v'$ length scales for the nozzles at $75\%L_c$. The length scales for the 0° nozzle are still increased over the baseline but the trough region length scales are now larger than the tip region. The 2° nozzle length scales are all decreased from the baseline values with larger length scales in the tip region. The tip region of the 4° nozzle has larger length scales than the baseline but the trough region length scales are lower than the baseline values.

Table 7.9 shows the $u'v'$ length scales for the nozzles at $100\%L_c$. The 0° nozzle length scales are still increased above the baseline values but less than the previous positions. The 2° nozzle length scales are decreased from the baseline values with slightly larger length scales in the tip region. The 4° nozzle length scales are very close to the baseline values but generally show a slight increase particularly for the trough region.

Table 7.7: $u'v'$ Length Scales and Convection Speed $0.5L_c$

0.5 L_c	L_c	Fixed Axis	Moving Axis	Convection Speed
		$u'v'$ (mm)	$u'v'$ (mm)	$u'v'$ (m/s)
SJ	4.92D	2.55	7.22	50.08
N0 Tip	4.64D	3.21	9.66	49.27
N0 Trough	4.64D	3.04	8.87	46.88
N2 Tip	3.80D	2.78	8.10	48.06
N2 Trough	3.80D	2.71	7.40	45.68
N4 Tip	4.13D	3.00	8.71	46.93
N4 Trough	4.13D	2.96	8.01	42.56

Table 7.8: $u'v'$ Length Scales and Convection Speed $0.75L_c$

0.75 L_c	L_c	Fixed Axis	Moving Axis	Convection Speed
		$u'v'$ (mm)	$u'v'$ (mm)	$u'v'$ (m/s)
SJ	4.92D	3.50	9.83	48.06
N0 Tip	4.64D	3.91	11.77	49.22
N0 Trough	4.64D	4.08	11.88	46.94
N2 Tip	3.80D	3.27	9.65	47.15
N2 Trough	3.80D	3.22	8.99	48.03
N4 Tip	4.13D	3.60	10.46	46.46
N4 Trough	4.13D	3.38	9.65	46.31

Table 7.9: $u'v'$ Length Scales and Convection Speed $1.0L_c$

1.0 L_c	L_c	Fixed Axis	Moving Axis	Convection Speed
		$u'v'$ (mm)	$u'v'$ (mm)	$u'v'$ (m/s)
SJ	4.92D	4.43	12.25	46.50
N0 Tip	4.64D	4.72	14.51	47.22
N0 Trough	4.64D	4.76	14.36	46.30
N2 Tip	3.80D	3.89	11.36	46.58
N2 Trough	3.80D	3.63	10.62	46.39
N4 Tip	4.13D	4.38	12.43	43.07
N4 Trough	4.13D	4.49	12.66	46.13

7.2 Frequency Dependent Length Scales

7.2.1 u' Moving Axis Length Scale

Figures 7.2 and 7.3 show the frequency dependent moving axis length scale for the u' component in the axial direction. Figure 7.2 (a) shows the 0° nozzle in comparison to the baseline jet at $50\%L_c$. This nozzle shows a significant increase to the length scale for all frequencies at this position. The tip regions also produce a larger increase in the length scale than the trough regions for all frequencies. There is a larger increase in the length scale for higher frequencies beyond a Strouhal number of 1 which show a 100% increase over the baseline values.

Figure 7.2 (b) shows the 2° nozzle in comparison to the baseline jet at $50\%L_c$. The values for both tip and trough region are equal to the baseline values below a Strouhal number of 0.2. Beyond this Strouhal number the baseline values fall between the tip and trough regions with the trough region having larger length scales. This nozzle had the shortest potential core length which may explain why it shows the smallest difference to the baseline nozzle in this position.

Figure 7.2 (c) shows the 4° nozzle in comparison to the baseline jet at $50\%L_c$. This nozzle shows an increase to the length scale for all frequencies at this position. The effects are more significant for higher frequencies beyond a Strouhal number of 1. The trough region shows the largest length scale while the tip region is much closer to the baseline particularly below a Strouhal number of 1.

Figure 7.3 (a) shows the 0° nozzle in comparison to the baseline jet at $100\%L_c$. The length scales for this nozzle are still significantly increased over the baseline values but the difference is less than the previous position. There are tip to trough region differences below a Strouhal number of 0.5 where the trough region has larger length scales. The length scales above this Strouhal number are equal for both regions and show a larger increase over the baseline than those at the lower Strouhal numbers.

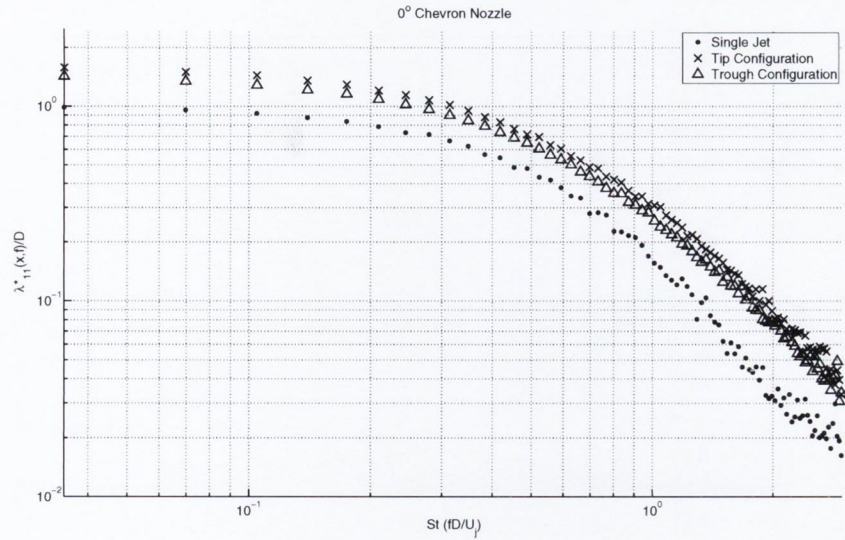
Figure 7.3 (b) shows the 2° nozzle in comparison to the baseline jet at $100\%L_c$. The trough region has larger length scales than the baseline at all frequencies. The tip region has lower length scales than the baseline below a Strouhal number of 0.4

but they are increased above the baseline beyond this Strouhal number.

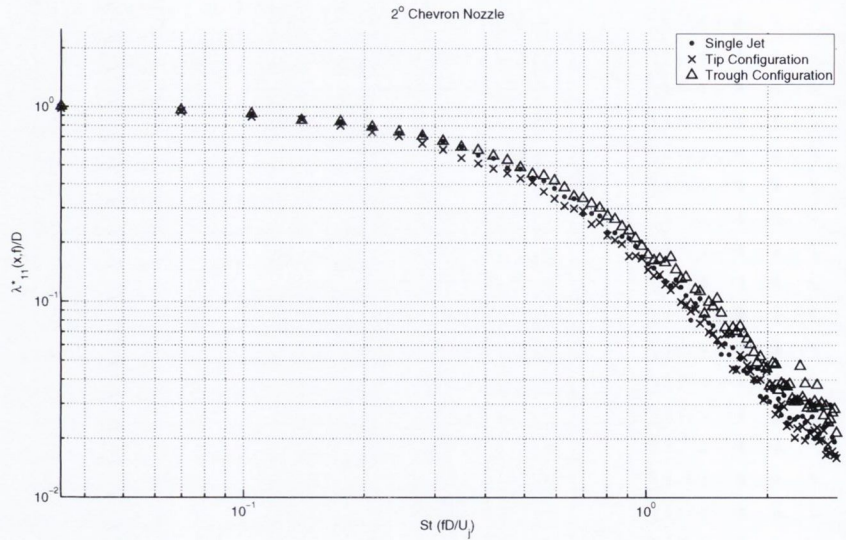
Figure 7.3 (c) shows the 4° nozzle in comparison to the baseline jet at $100\%L_c$. The baseline length scales fall between the tip region and trough region for all frequencies. The trough region shows a slight increase to the length scales over the baseline case at all frequencies and the tip region a slight decrease. The tip region of this nozzle in this position is the only result lower than the baseline at all Strouhal numbers.

Firstly comparing the traditional statistics to the frequency dependent statistics at $50\%L_c$ it is found that the 0° nozzle reflects what was previously observed and shows an increase for all frequencies with a larger effect in the tip region. In comparison the traditional statistics for the 2° nozzle showed a larger increase in the tip region while the frequency dependent statistics show that beyond a Strouhal number of 0.2 the trough region length scales are actually larger. This could be explained if the traditional statistics are dominated by the larger scales of the turbulence. The 4° nozzle length scales do not agree well with the traditional statistics as the trough region length scale is clearly larger for all scales of the turbulence where as the tip region is larger in the traditional statistics.

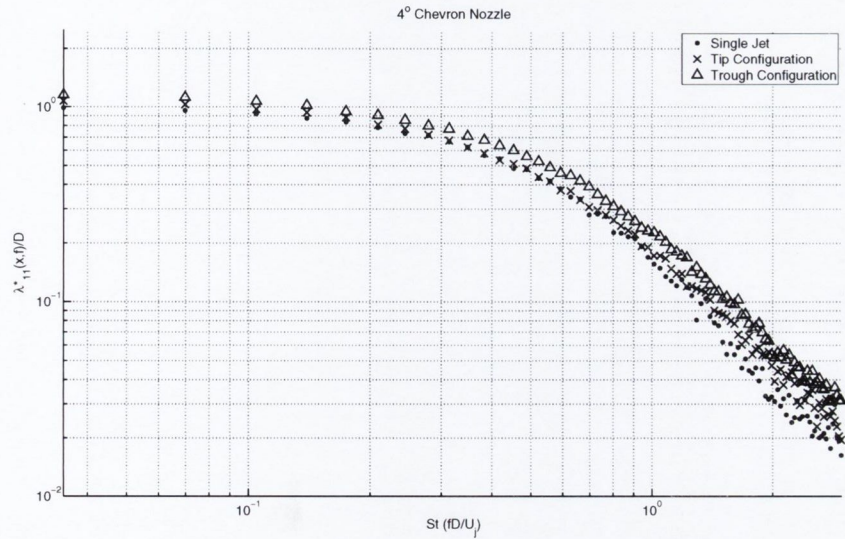
At $100\%L_c$ the 0° nozzle again reflects the traditional statistics as the trough region shows an increase over the tip region below a Strouhal number of 0.5. Beyond this Strouhal number the two regions are equal and this is in agreement with the slightly larger values found in the trough region's traditional statistics. For this position the 2° nozzle does not agree well with the traditional statistics as the trough region length scales are larger than the tip. While the low frequency length scales are close to or below the baseline values the high frequencies are significantly increased. This difference from the traditional statistics could again be explained if they are dominated by the larger turbulence scales. The 4° nozzle agrees with the traditional statistics as the trough region length scales are larger than the tip region. The trough region length scales are increased over the baseline for all frequencies reflecting the increase in the traditional statistics where as the tip region length scales show a high frequency reduction not seen in the traditional statistics.



(a)



(b)

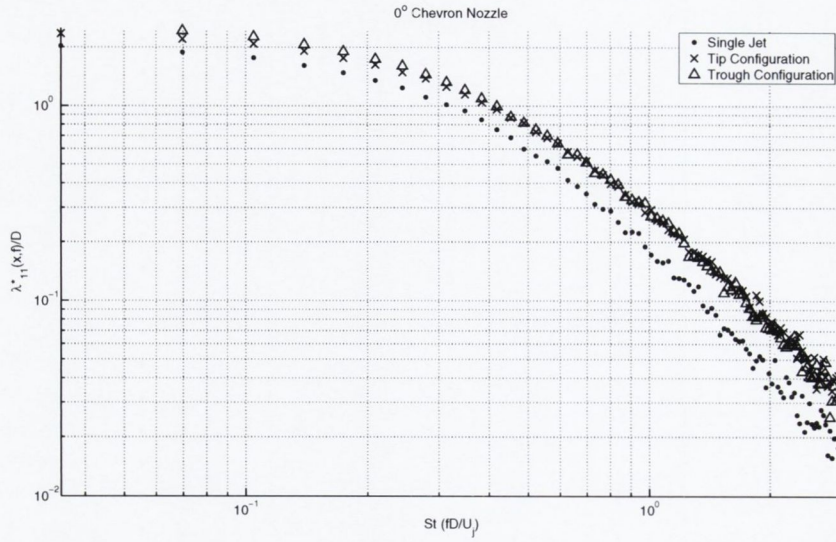


(c)

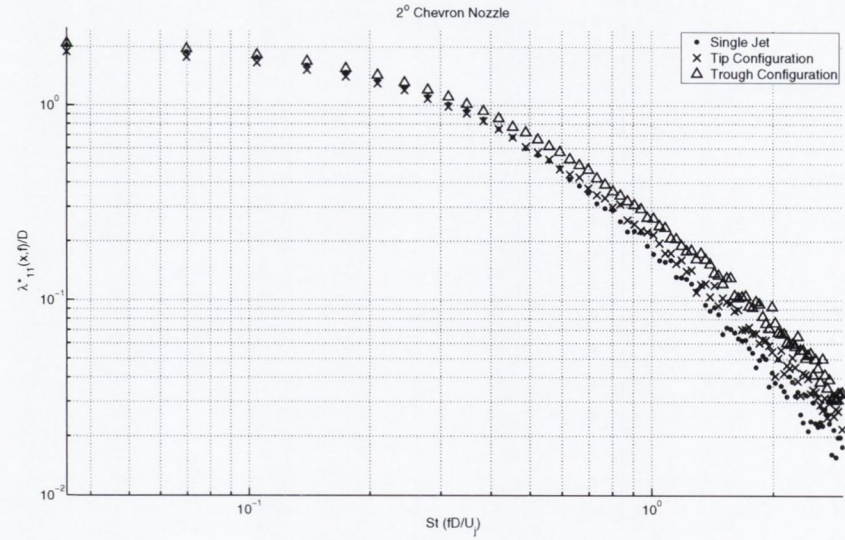
$0.5L_c$	L_c	Fixed Axis (mm)	Moving Axis (mm)	Convection Speed (m/s)
SJ	4.92D	7.96	27.06	41.95
N0 Tip	4.64D	10.10	38.90	44.36
N0 Trough	4.64D	9.36	35.24	41.11
N2 Tip	3.80D	8.41	27.01	41.67
N2 Trough	3.80D	7.66	26.82	40.60
N4 Tip	4.13D	8.71	28.06	40.92
N4 Trough	4.64D	7.43	26.09	38.94

(d)

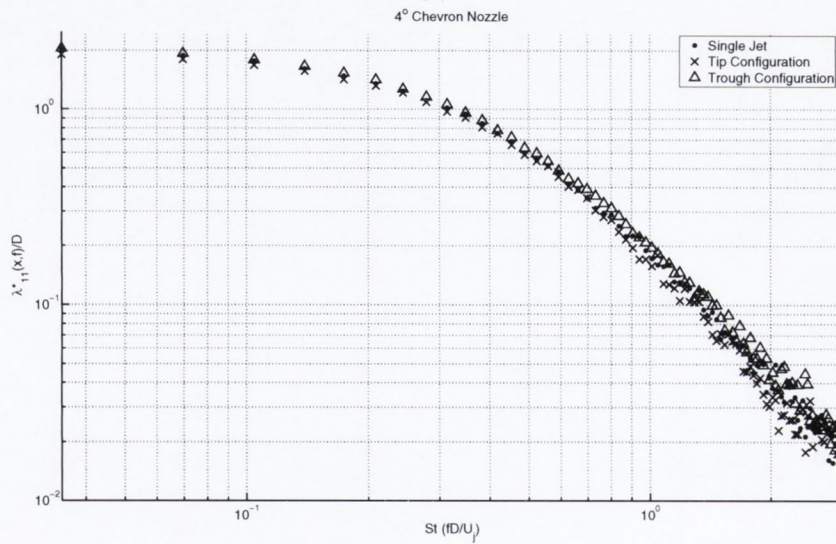
Figure 7.2: Frequency Dependent Moving Axis Length Scale $u' = 50\%L_c$



(a)



(b)



(c)

$1.0L_c$	L_c	Fixed Axis (mm)	Moving Axis (mm)	Convection Speed (m/s)
SJ	4.92D	13.60	47.06	39.73
N0 Tip	4.64D	15.45	55.92	41.44
N0 Trough	4.64D	15.86	56.20	40.18
N2 Tip	3.80D	13.13	46.13	38.48
N2 Trough	3.80D	12.06	43.57	38.64
N4 Tip	4.13D	13.64	48.05	37.40
N4 Trough	4.64D	13.81	49.78	38.74

(d)

Figure 7.3: Frequency Dependent Moving Axis Length Scale $u' 100\%L_c$

7.2.2 v' Moving Axis Length Scale

Figures 7.4 and 7.5 show the frequency dependent moving axis length scale for the v' component in the axial direction. Figure 7.4 (a) shows the 0° nozzle in comparison to the baseline jet at $50\%L_c$. This nozzle globally increases the length scale for all frequencies. The effect is less significant than for the u' component which showed increases of up to 100% for the higher frequencies. However the increase seen in the length scales of the lower frequencies is larger than that seen for the same u' length scales. The tip and trough regions are relatively equal for this nozzle in this position.

Figure 7.4 (b) shows the 2° nozzle in comparison to the baseline jet at $50\%L_c$. The baseline case falls between the tip and trough regions for this nozzle. The tip regions have slightly lower length scales than the baseline over all frequencies and the trough regions have slightly increased length scales particularly above a Strouhal number of 0.8.

Figure 7.4 (c) shows the 4° nozzle in comparison to the baseline jet at $50\%L_c$. Similarly to the 2° nozzle the baseline case falls between the tip and trough regions for this nozzle in this position. The trough region has a slightly increased length scale and the tip region shows a slight decrease in comparison to the baseline values.

Figure 7.5 (a) shows the 0° nozzle in comparison to the baseline jet at $100\%L_c$. The length scales are still increased over the baseline values for all frequencies but the increase is significantly less than for the previous position.

Figure 7.5 (b) shows the 2° nozzle in comparison to the baseline jet at $100\%L_c$. There is a significant reduction in the length scales below a Strouhal number of 0.7 and above this Strouhal number the length scales are equal to the baseline. The tip region has a larger decrease than the trough region. Tip to trough region differences have also increased in comparison to the previous position.

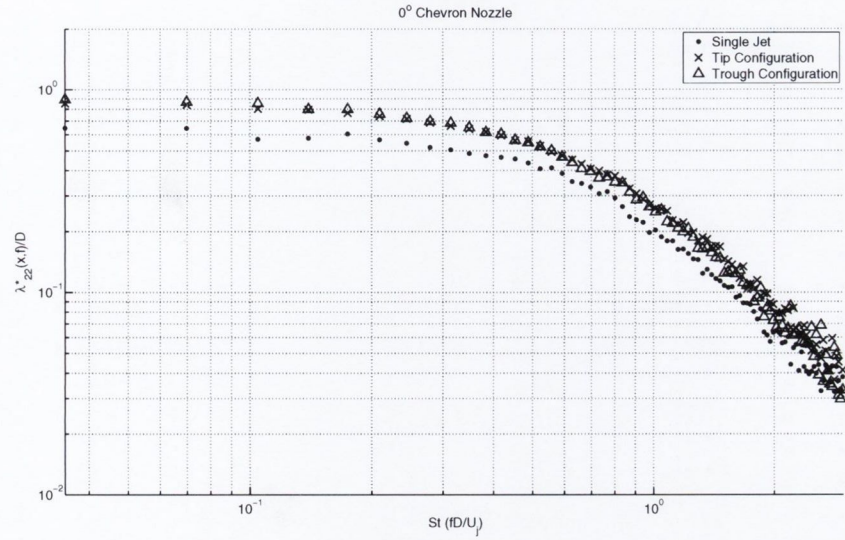
Figure 7.5 (c) shows the 4° nozzle in comparison to the baseline jet at $100\%L_c$. Length scales above a Strouhal number of 0.8 are equal to the baseline values for both tip and trough regions. Below this Strouhal number the tip and trough region have slightly decreased length scales.

The frequency dependent statistics for the 0° nozzle agree with what was observed

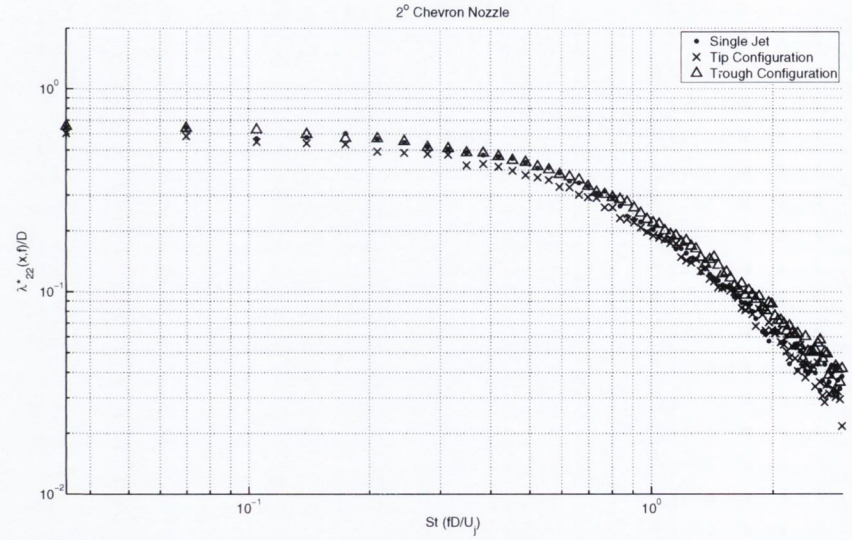
7.2. FREQUENCY DEPENDENT LENGTH SCALES

in the traditional statistics and show a global increase at $50\%L_c$. A point of note is that the increase in the high frequency v' length scales is significantly less than the increase observed for the u' high frequency length scales while the traditional statistics would indicate that the v' length scales are more strongly affected. The low frequency length scales of the 2° nozzle at $50\%L_c$ show a slight reduction from the baseline as was found in the traditional statistics but at high frequencies the trough region in particular shows increased length scales. The 4° nozzle was closest to the baseline in the traditional statistics and this nozzle also matches the baseline length scales for all frequencies.

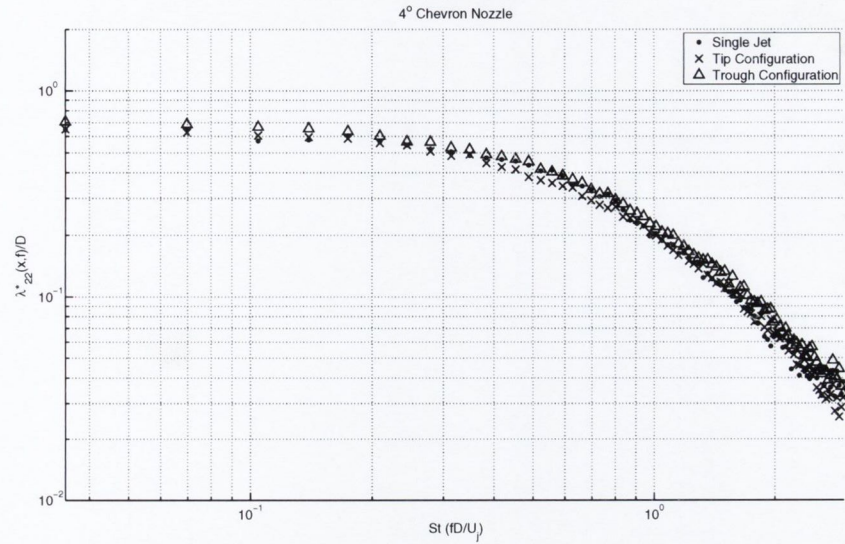
At $100\%L_c$ the 0° nozzle still shows a slight increase over the baseline in the traditional statistics and the frequency dependent statistics show that the increase is still more significant for higher frequencies. The 2° nozzle length scales for this position clearly point to the traditional statistics being driven by the lower frequencies as it is these scales of the turbulence that show the significant decrease observed in the traditional statistics. The higher frequency turbulent length scales are in fact equal to the baseline nozzle values. A very similar result is observed for the 4° nozzle as the reduction in length scale observed in the traditional statistics is only found for the lower frequency length scales.



(a)



(b)

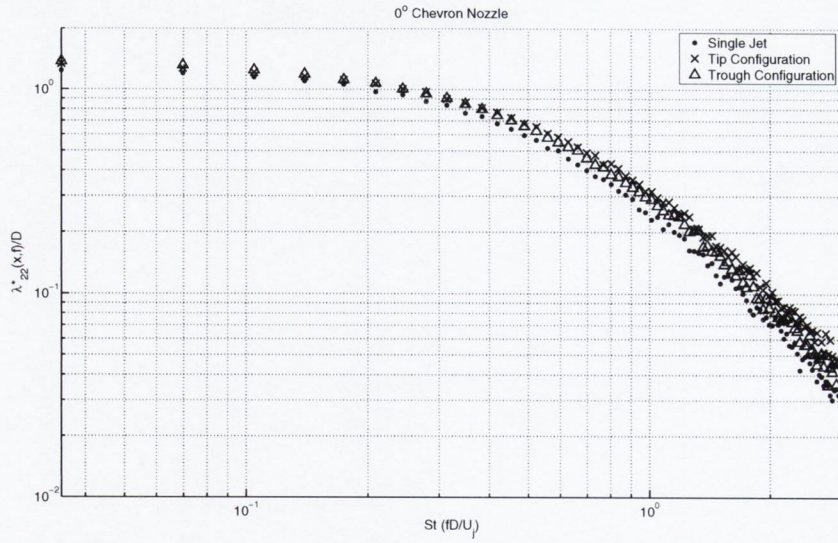


(c)

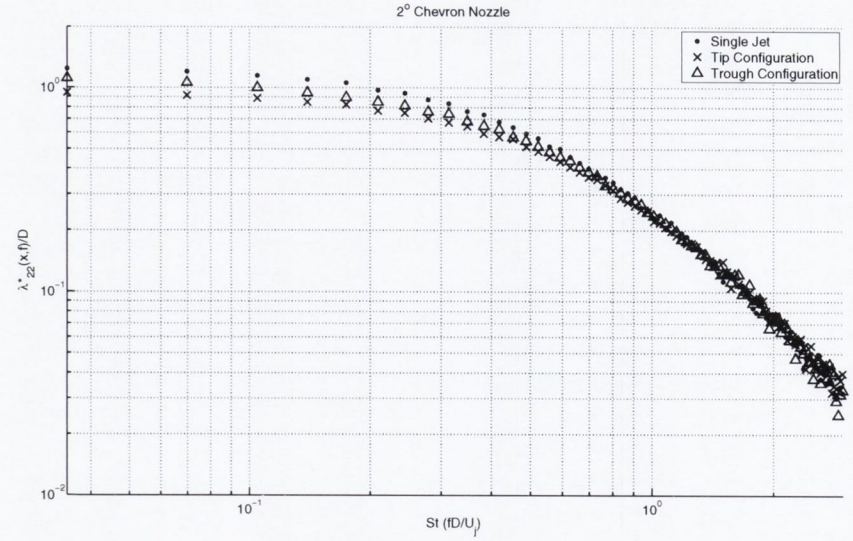
$0.5L_c$	L_c	Fixed Axis (mm)	Moving Axis (mm)	Convection Speed (m/s)
SJ	4.92D	4.54	19.60	52.63
N0 Tip	4.64D	6.18	25.18	50.49
N0 Trough	4.64D	5.63	22.68	43.25
N2 Tip	3.80D	4.00	16.94	51.19
N2 Trough	3.80D	4.34	17.88	41.60
N4 Tip	4.13D	4.48	20.28	41.67
N4 Trough	4.13D	4.69	18.10	36.68

(d)

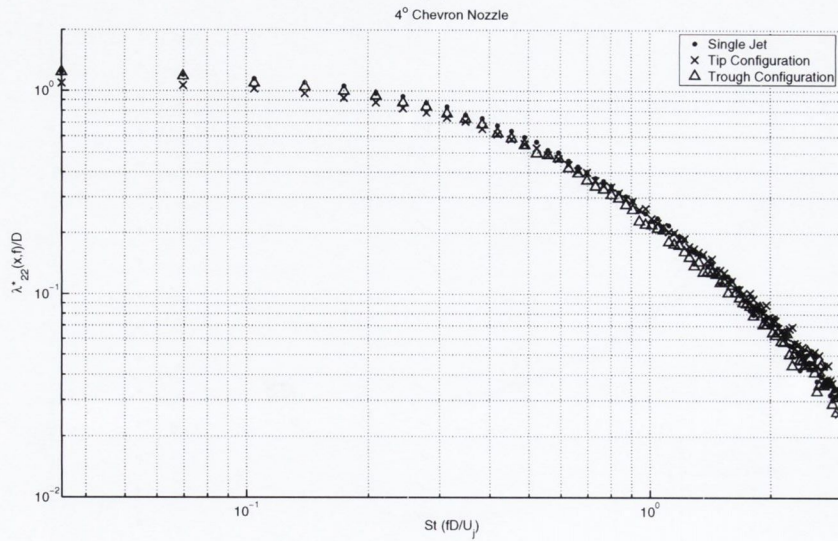
Figure 7.4: Frequency Dependent Moving Axis Length Scale $v' 50\%L_c$



(a)



(b)



(c)

$1.0L_c$	L_c	Fixed Axis (mm)	Moving Axis (mm)	Convection Speed (m/s)
SJ	4.92D	7.19	27.14	40.16
N0 Tip	4.64D	7.88	31.04	43.58
N0 Trough	4.64D	7.72	30.62	40.95
N2 Tip	3.80D	5.91	22.29	39.45
N2 Trough	3.80D	6.09	22.74	40.28
N4 Tip	4.13D	6.55	25.03	37.19
N4 Trough	4.13D	6.67	23.96	38.87

(d)

Figure 7.5: Frequency Dependent Moving Axis Length Scale $v' 100\%L_c$

7.2.3 u'^2 Moving Axis Length Scale

Figures 7.6 and 7.7 show the frequency dependent moving axis length scale for the u'^2 component in the axial direction. Figure 7.6 (a) shows the 0° nozzle in comparison to the baseline jet at $50\%L_c$. This nozzle increases the length scales over the baseline values for all frequencies in both tip and trough regions. The tip region has a larger increase than the trough region.

Figure 7.6 (b) shows the 2° nozzle in comparison to the baseline jet at $50\%L_c$. The trough region is equal to the baseline for all frequencies in this position. The tip region shows decreased length scales below a Strouhal number of 0.5. Above this Strouhal number the tip region length scales are also equal to the baseline.

Figure 7.6 (c) shows the 4° nozzle in comparison to the baseline jet at $50\%L_c$. Below a Strouhal number of 0.4 the baseline values fall between the tip and trough region with the trough region being larger than the baseline. Above this Strouhal number both regions show an equal increase in the length scales over the baseline.

Figure 7.7 (a) shows the 0° nozzle in comparison to the baseline jet at $100\%L_c$. The length scales for both tip and trough regions are increased over the baseline values. The tip region length scales are larger below a Strouhal number of 1.

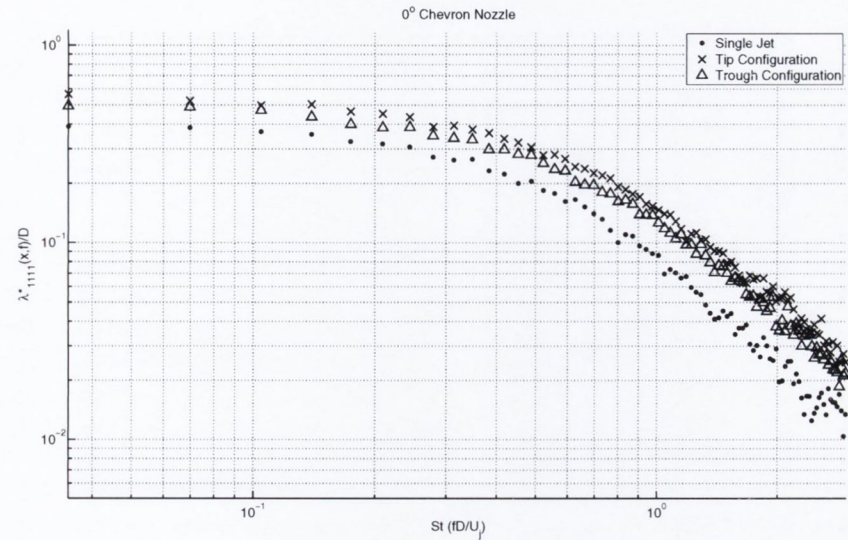
Figure 7.7 (b) shows the 2° nozzle in comparison to the baseline jet at $100\%L_c$. Below a Strouhal number of 0.5 the tip and trough region length scales are equal to the baseline values. Above this Strouhal number the length scales are increased with the trough region having larger length scales.

Figure 7.7 (c) shows the 4° nozzle in comparison to the baseline jet at $100\%L_c$. The tip and trough region length scales are approximately equal to the baseline values for all frequencies at this position.

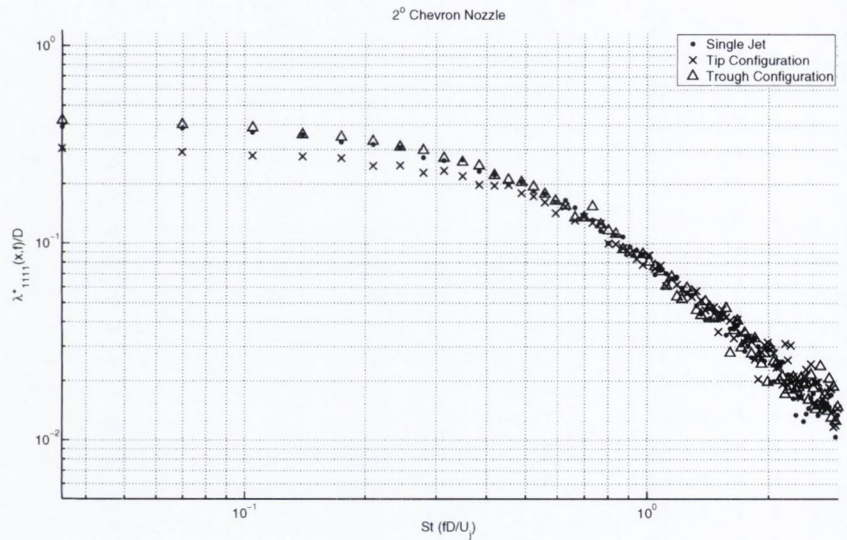
The 0° nozzle frequency dependent statistics agree with the traditional statistics at $50\%L_c$ and show an increase in both tip and trough regions over the baseline with a more significant effect in the tip region. The 2° nozzle shows another interesting result as the decrease in the length scales of the tip region found in the traditional statistics is shown in the frequency dependent statistics below a Strouhal number of 0.5. Beyond this Strouhal number the length scales are equal to the baseline. The trough

region length scales are approximately equal to the baseline as were the traditional statistics. The tip region of the 4° nozzle is interesting as the frequency dependent statistics show a low frequency decrease and a high frequency increase compared to the baseline. This difference in behaviour between turbulent scales is not captured in the traditional statistics which show a slight increase for both tip and trough regions.

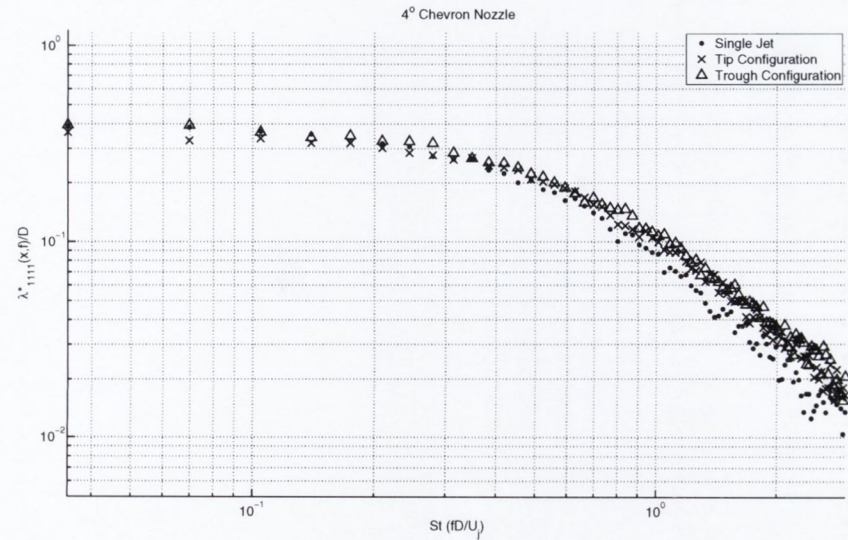
The 0° nozzle shows good agreement with the traditional statistics at $100\%L_c$ as all turbulence scales show an increased length scale with a larger increase in the tip region particularly at low frequencies. The traditional statistics for the 2° nozzle in this position are very close to the baseline and are generally slightly reduced. In contrast the frequency dependent statistics show significant increases to the length scales of both tip and trough regions beyond a Strouhal number of 0.5 with a larger increase in the trough region. The lower frequency turbulent scales are very similar to the baseline. The traditional statistics for the 4° nozzle show a slight increase which is possibly reflected in the frequency dependent statistics at low frequencies but the values are very close to the baseline.



(a)



(b)

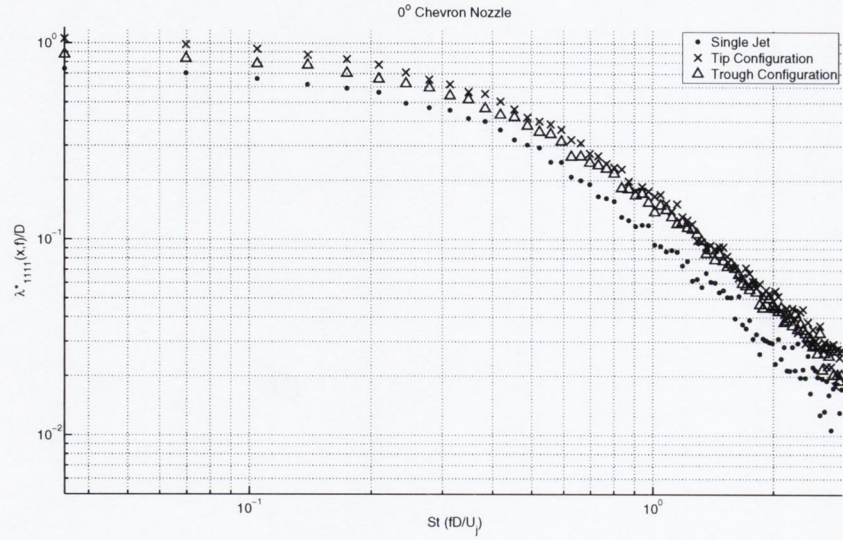


(c)

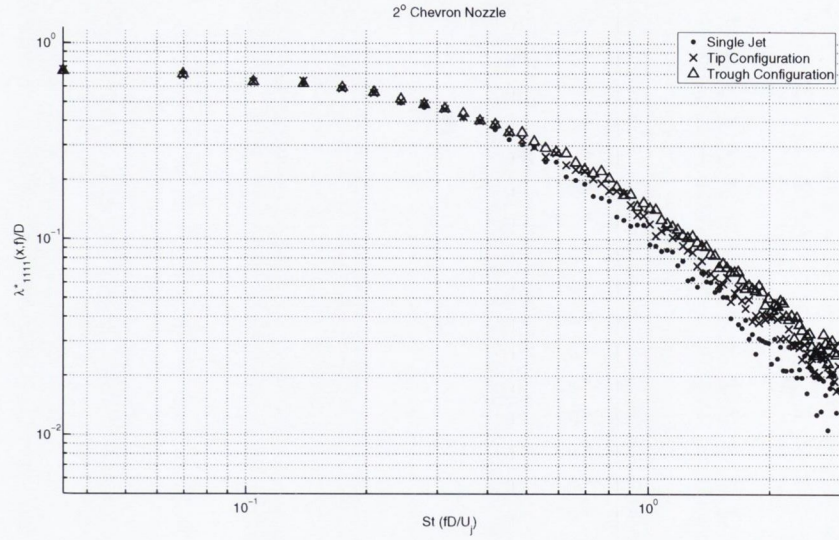
$0.5L_c$	L_c	Fixed Axis (mm)	Moving Axis (mm)	Convection Speed (m/s)
SJ	4.92D	4.05	9.25	37.31
N0 Tip	4.64D	4.80	13.49	37.21
N0 Trough	4.64D	4.54	11.92	27.93
N2 Tip	3.80D	3.72	8.83	48.54
N2 Trough	3.80D	3.84	9.01	21.32
N4 Tip	4.13D	4.00	10.48	45.08
N4 Trough	4.13D	3.75	9.67	27.13

(d)

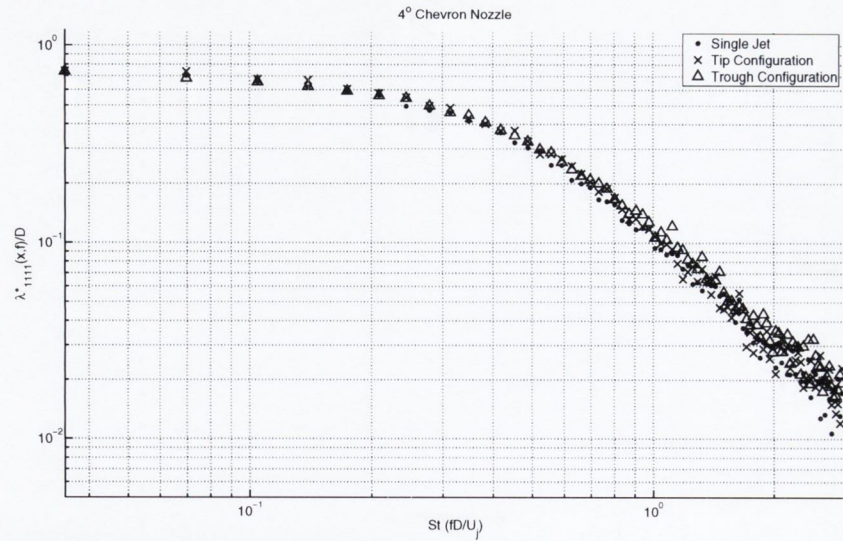
Figure 7.6: Frequency Dependent Moving Axis Length Scale u'^2 50% L_c



(a)



(b)



(c)

$1.0L_c$	L_c	Fixed Axis (mm)	Moving Axis (mm)	Convection Speed (m/s)
SJ	4.92D	6.53	16.52	47.36
N0 Tip	4.64D	7.16	20.84	44.69
N0 Trough	4.64D	7.19	19.93	44.52
N2 Tip	3.80D	6.33	16.76	44.63
N2 Trough	3.80D	5.49	15.50	44.57
N4 Tip	4.13D	6.66	17.87	44.04
N4 Trough	4.13D	6.78	18.01	45.71

(d)

Figure 7.7: Frequency Dependent Moving Axis Length Scale $u'^2 \ 100\%L_c$

7.2.4 v'^2 Moving Axis Length Scales

Figures 7.8 and 7.9 show the frequency dependent moving axis length scale for the v'^2 component in the axial direction. Figure 7.8 (a) shows the 0° nozzle in comparison to the baseline jet at $50\%L_c$. This nozzle shows an increase to the length scales for both tip and trough regions with a clearer increase below a Strouhal number of 1. The trough region length scales are larger than the tip regions below a Strouhal number of 0.5.

Figure 7.8 (b) shows the 2° nozzle in comparison to the baseline jet at $50\%L_c$. The trough region length scales are approximately equal to the baseline values in this position with a slight increase in the tip region.

Figure 7.8 (c) shows the 4° nozzle in comparison to the baseline jet at $50\%L_c$. The tip region length scales are increased above the baseline values for all frequencies. The trough region length scales are equal to the baseline values above a Strouhal number of 0.8 but are increased below this Strouhal number.

Figure 7.9 (a) shows the 0° nozzle in comparison to the baseline jet at $100\%L_c$. The tip and trough region length scales show an equal increase over the baseline values for all frequencies. The increase is less significant than for the previous position.

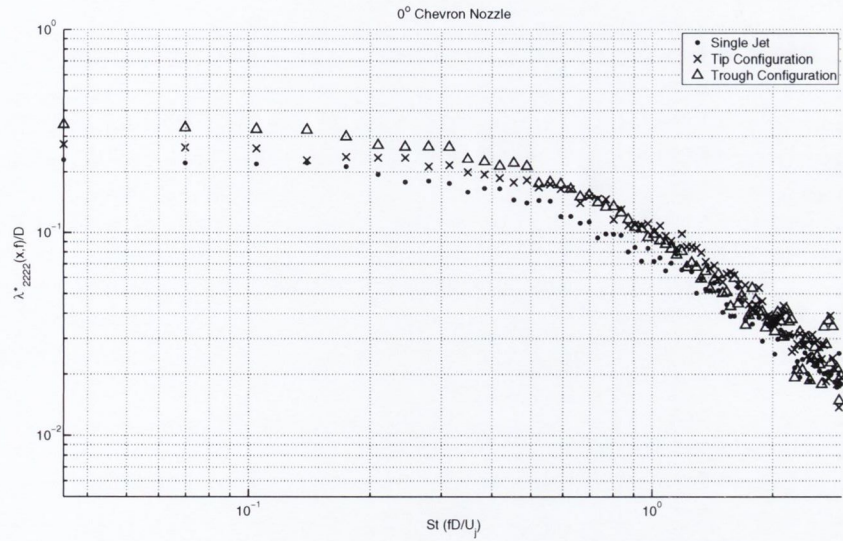
Figure 7.9 (b) shows the 2° nozzle in comparison to the baseline jet at $100\%L_c$. Above a Strouhal number of 1 both tip and trough region length scales are equal to the baseline values. Below this Strouhal number both regions have decreased length scales. The trough region shows a larger decrease than the tip region.

Figure 7.9 (c) shows the 4° nozzle in comparison to the baseline jet at $100\%L_c$. Tip and trough region length scales show a slight decrease from the baseline values for all frequencies.

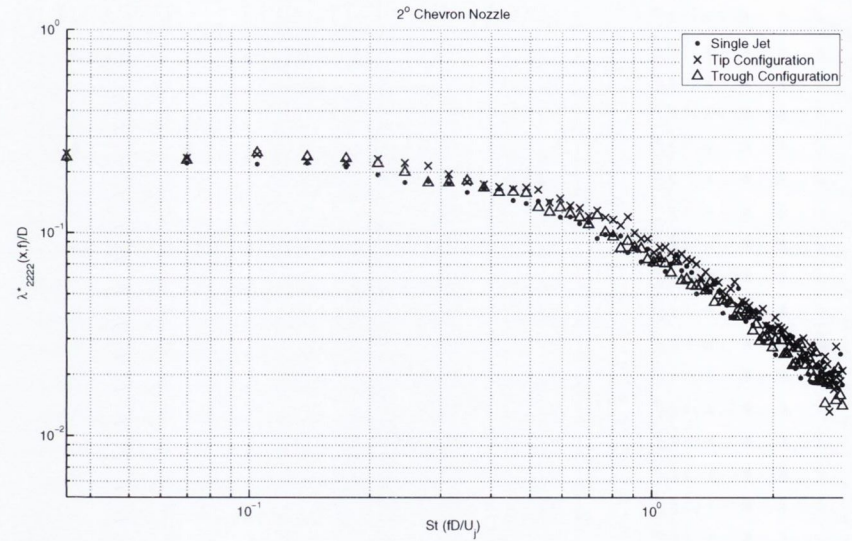
The 0° nozzle shows good agreement with the traditional statistics at $50\%L_c$ as both tip and trough region length scales show a significant increase. The traditional statistics show a larger tip region length scale and this is reflected in the frequency dependent statistics below a Strouhal number of 0.5. The 2° nozzle trough region is very similar to the baseline nozzle in both the traditional and frequency dependent statistics. The tip region shows a slight increase in the length scale over the baseline

and this is visible in the frequency dependent statistics particularly in a Strouhal number range of 0.2 – 1.5. The 4° nozzle tip region shows a significant increase to the length scales at 50% L_c for both frequency dependent and traditional statistics. The frequency dependent length scales for the trough region are equal to the baseline above a Strouhal number of 0.5 but the increase for lower frequencies than this is not seen in the traditional statistics.

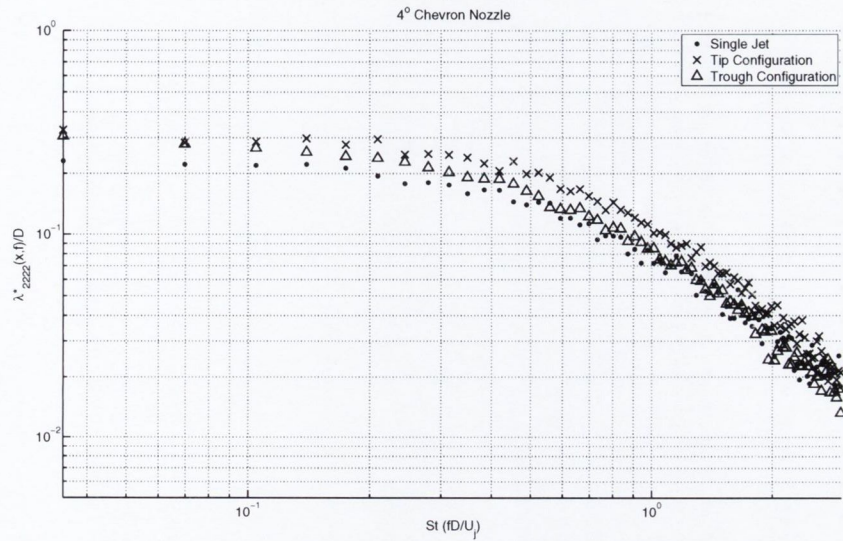
The frequency dependent statistics for the 0° nozzle at 100% L_c are still increased but the increase is less significant than in the previous position and this is reflected in the traditional statistics. The scales above a Strouhal number of 1 are closest to the baseline and there are minimal tip to trough region differences found in either traditional or frequency dependent statistics. The 2° nozzle shows a decrease in the traditional length scales from the baseline for both tip and trough regions. This is seen in the frequency dependent length scales below a Strouhal number of 0.6. Above this Strouhal number both tip and trough region length scales are equal to the baseline. The traditional statistics for the 4° nozzle show a less significant decrease from the baseline than for the 2° nozzle. However the frequency dependent statistics show that the decrease is for a wider range of frequencies than for the 2° nozzle.



(a)



(b)

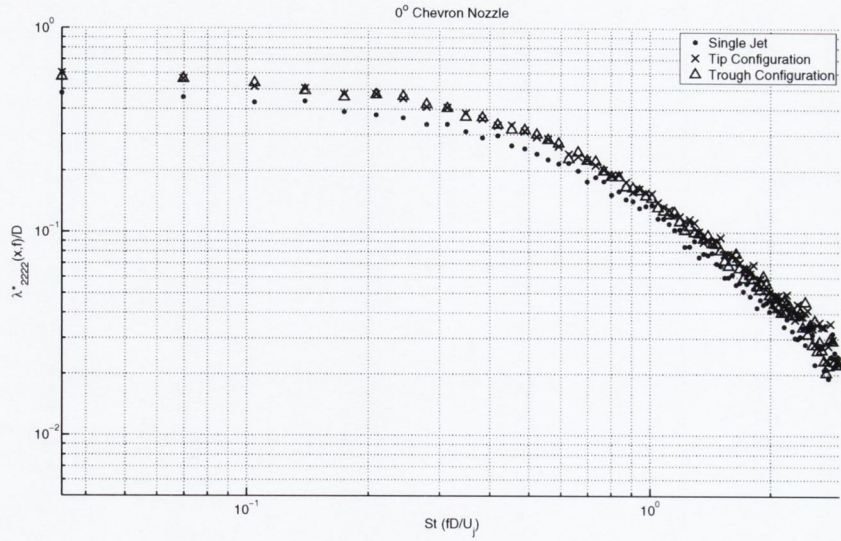


(c)

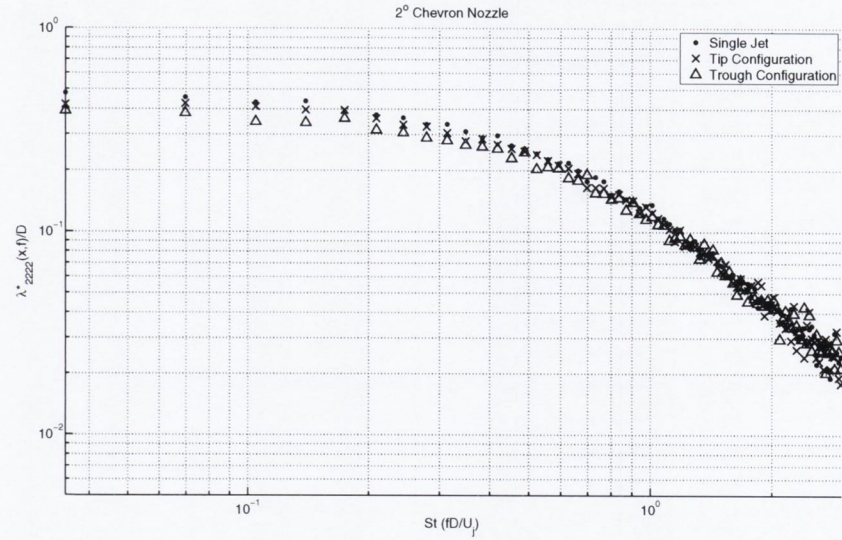
$0.5L_c$	L_c	Fixed Axis (mm)	Moving Axis (mm)	Convection Speed (m/s)
SJ	4.92D	2.66	5.79	53.76
N0 Tip	4.64D	3.37	8.28	56.65
N0 Trough	4.64D	3.37	7.26	58.16
N2 Tip	3.80D	2.49	6.39	50.07
N2 Trough	3.80D	2.42	5.72	28.61
N4 Tip	4.13D	2.77	7.67	41.83
N4 Trough	4.13D	2.53	5.76	28.71

(d)

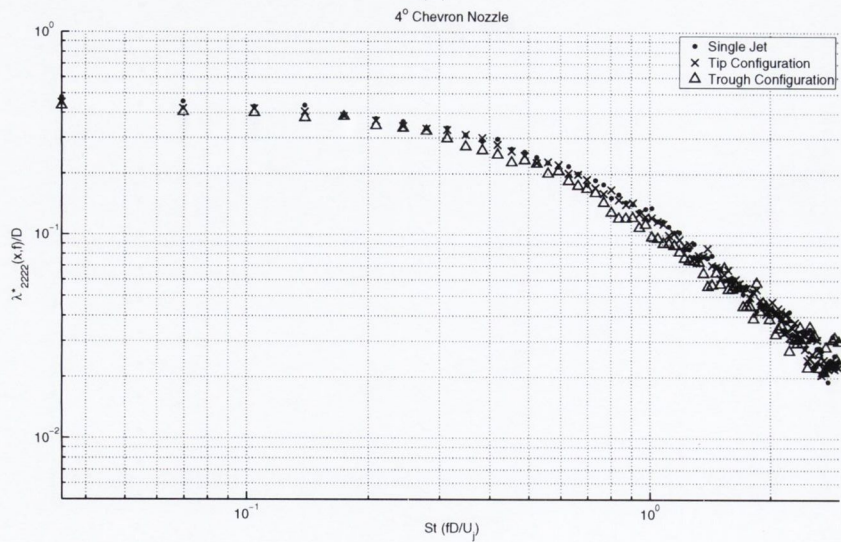
Figure 7.8: Frequency Dependent Moving Axis Length Scale $v'^2 \ 50\%L_c$



(a)



(b)



(c)

$1.0L_c$	L_c	Fixed Axis (mm)	Moving Axis (mm)	Convection Speed (m/s)
SJ	4.92D	4.40	10.00	50.15
N0 Tip	4.64D	4.69	11.88	51.04
N0 Trough	4.64D	4.77	11.95	48.71
N2 Tip	3.80D	3.60	8.79	50.41
N2 Trough	3.80D	3.66	8.79	50.83
N4 Tip	4.13D	3.96	9.98	49.81
N4 Trough	4.13D	4.01	9.47	46.65

(d)

Figure 7.9: Frequency Dependent Moving Axis Length Scale $v'^2 \ 100\%L_c$

7.2.5 $u'v'$ Moving Axis Length Scale

Figures 7.10 and 7.11 show the frequency dependent moving axis length scale for the $u'v'$ component in the axial direction. Figure 7.10 (a) shows the 0° nozzle in comparison to the baseline jet at $50\%L_c$. Tip and trough regions show an equal increase to the length scales over the baseline values. The increase is more significant for higher frequencies.

Figure 7.10 (b) shows the 2° nozzle in comparison to the baseline jet at $50\%L_c$. Tip and trough regions are equal to the baseline length scales below a Strouhal of 1. Above this Strouhal number both tip and trough regions show a slight increase to the length scales.

Figure 7.10 (c) shows the 4° nozzle in comparison to the baseline jet at $50\%L_c$. Tip and trough region length scales are both increased above the baseline values. Below a Strouhal number of 0.4 the trough region length scales are larger than the tip region. However above a Strouhal number of 0.8 this reverses and the tip region length scales are larger.

Figure 7.11 (a) shows the 0° nozzle in comparison to the baseline jet at $100\%L_c$. Tip and trough regions are equal and show increased length scales over the baseline values at all frequencies.

Figure 7.11 (b) shows the 2° nozzle in comparison to the baseline jet at $100\%L_c$. Below a Strouhal number of 0.7 tip and trough regions show decreased length scales compared to the baseline but above this Strouhal number both regions show slightly increased length scales.

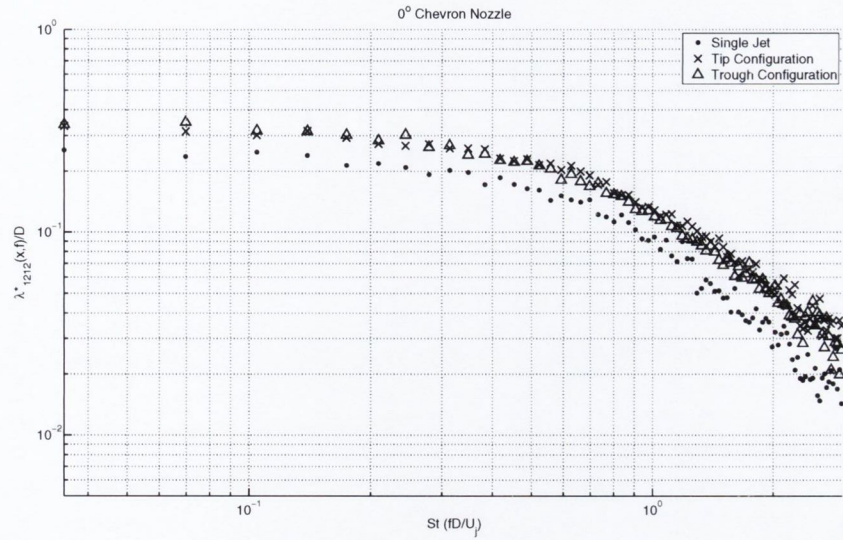
Figure 7.11 (c) shows the 4° nozzle in comparison to the baseline jet at $100\%L_c$. Tip and trough regions are approximately equal to the baseline values for all frequencies in this positions.

The traditional statistics for the 0° nozzle at $50\%L_c$ show increased length scales in the tip and trough regions over the baseline with a larger increase in the trough region. The frequency dependent length scales also show this increase with a slight indication of larger tip region length scales beyond a Strouhal number of 0.7. The 2° nozzle shows a slight increase in the traditional length scales with a larger increase

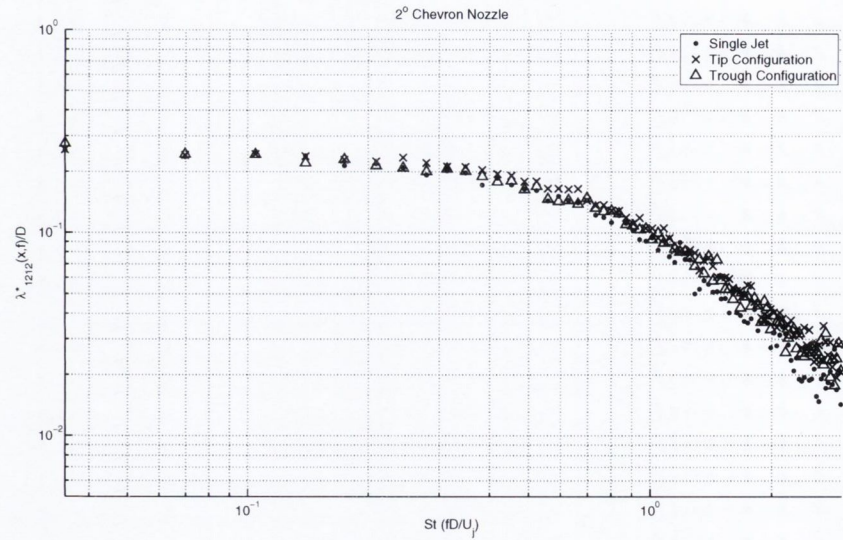
7.2. FREQUENCY DEPENDENT LENGTH SCALES

over the baseline found in the tip region. This increase is shown in the frequency dependent statistics for the higher frequencies where the tip region shows an increase beyond a Strouhal number of 0.5 and the trough region beyond a Strouhal number of 0.7. The traditional length scales for the 4° nozzle show an increase over the baseline with a larger increase in the tip region. While both tip and trough region length scales are increased in the frequency dependent statistics it is the trough region that shows a larger increase at lower scales and the tip region has a slightly larger increase at higher frequencies.

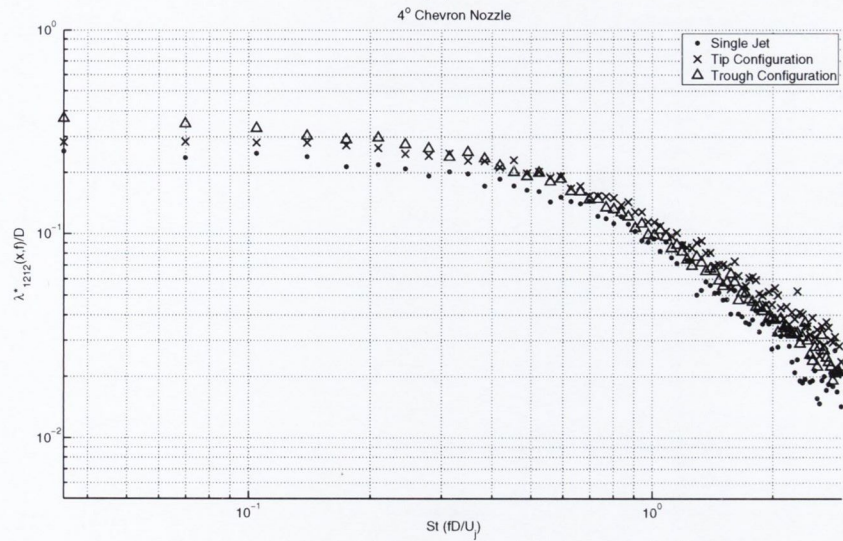
The traditional statistics for the 0° nozzle at $100\%L_c$ show increased length scales in the tip and trough regions over the baseline and the frequency dependent length scales also show this increase. The traditional statistics for the 2° nozzle show decreased length scales in the tip and trough regions from the baseline values. This decrease is seen in the frequency dependent length scales below a Strouhal number of 0.7. Above this Strouhal number the length scales for both regions are increased above the baseline values. The traditional length scales for the 4° nozzle at $100\%L_c$ show a very slight increase over the baseline and the frequency dependent length scales are approximately equal to the baseline at all frequencies.



(a)



(b)

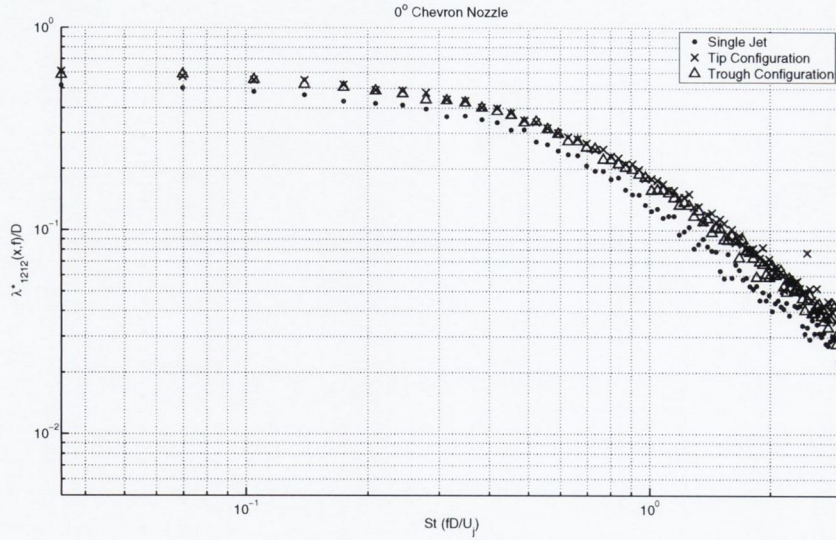


(c)

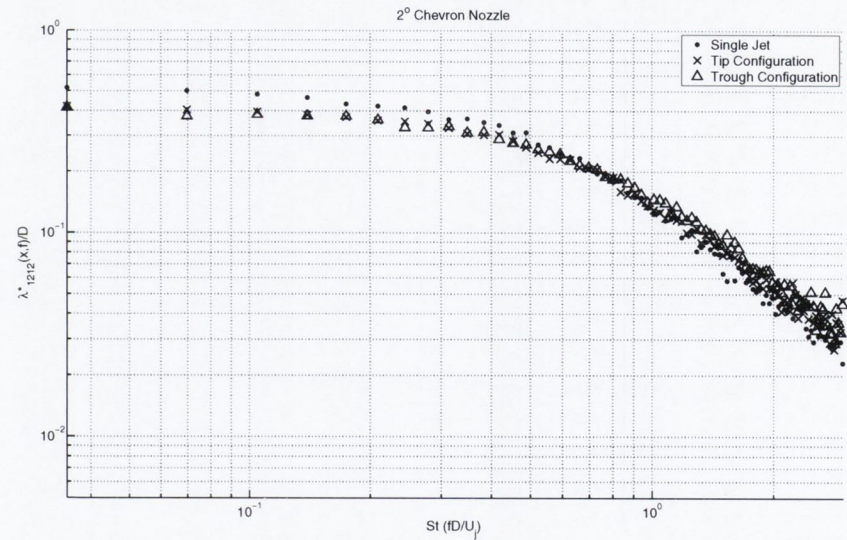
$0.5L_c$	L_c	Fixed Axis (mm)	Moving Axis (mm)	Convection Speed (m/s)
SJ	4.92D	2.55	7.22	50.08
N0 Tip	4.64D	3.21	9.66	49.27
N0 Trough	4.64D	3.04	8.87	46.88
N2 Tip	3.80D	2.78	8.10	48.06
N2 Trough	3.80D	2.71	7.40	45.68
N4 Tip	4.13D	3.00	8.71	46.93
N4 Trough	4.13D	2.96	8.01	42.56

(d)

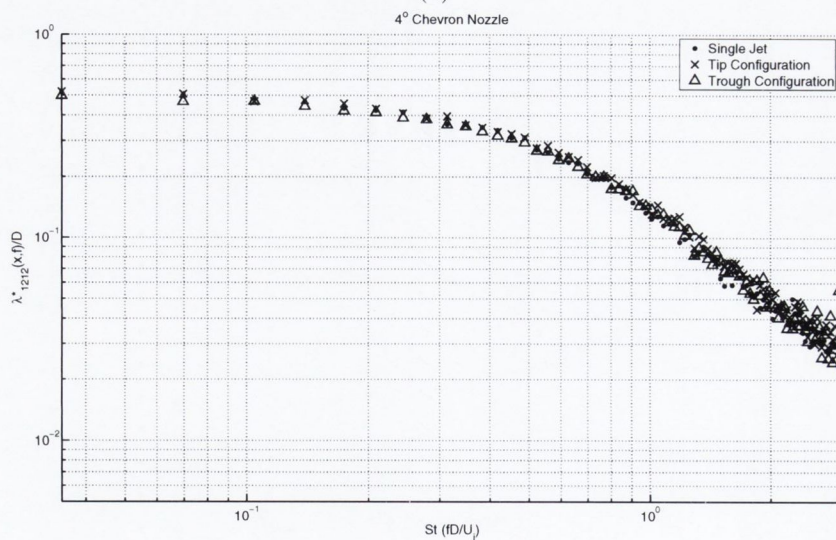
Figure 7.10: Frequency Dependent Moving Axis Length Scale $u'v'$ 50% L_c



(a)



(b)



(c)

$1.0L_c$	L_c	Fixed Axis (mm)	Moving Axis (mm)	Convection Speed (m/s)
SJ	4.92D	4.43	12.25	46.50
N0 Tip	4.64D	4.72	14.51	47.22
N0 Trough	4.64D	4.76	14.36	46.30
N2 Tip	3.80D	3.89	11.36	46.58
N2 Trough	3.80D	3.63	10.62	46.39
N4 Tip	4.13D	4.38	12.43	43.07
N4 Trough	4.13D	4.49	12.66	46.13

(d)

Figure 7.11: Frequency Dependent Moving Axis Length Scale $u'v'$ 100% L_c

7.2.6 u' Fixed Axis Length Scale

Figures 7.12 and 7.13 show the frequency dependent fixed axis length scale for the u' component in the axial direction. Figure 7.12 (a) shows the 0° nozzle in comparison to the baseline jet at $50\%L_c$. Tip and trough regions are equal and show an increase in the length scales above the baseline values for all frequencies. Above a Strouhal number of 0.8 the length scales show a more significant increase from the baseline.

Figure 7.12 (b) shows the 2° nozzle in comparison to the baseline jet at $50\%L_c$. The tip and trough region length scales are roughly equal to the baseline values in this position.

Figure 7.12 (c) shows the 4° nozzle in comparison to the baseline jet at $50\%L_c$. The tip and trough region length scales are roughly equal to the baseline values below a Strouhal number of 1. Above this Strouhal number both regions show increased length scales with a more significant increase in the trough region.

Figure 7.13 (a) shows the 0° nozzle in comparison to the baseline jet at $100\%L_c$. Tip and trough region length scales are still increased above a Strouhal number of 0.7 but the increase is less significant than in previous positions. Below this Strouhal number the length scales are equal to the baseline.

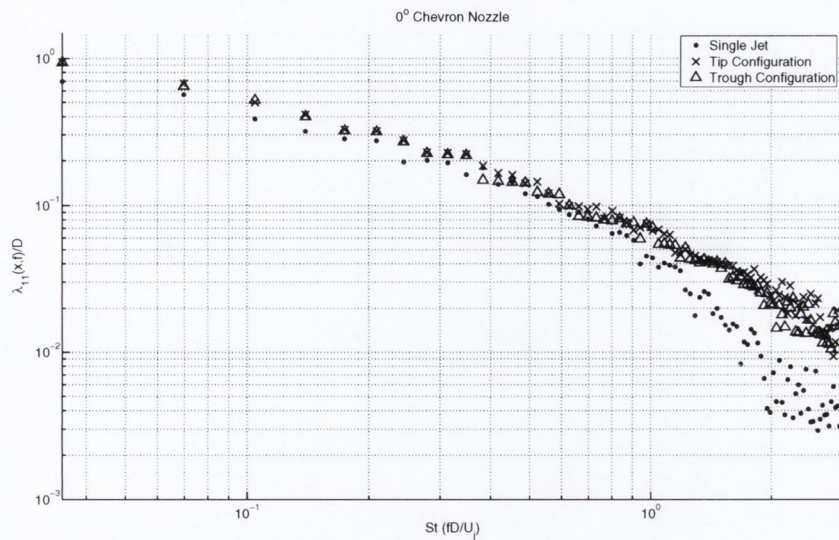
Figure 7.13 (b) shows the 2° nozzle in comparison to the baseline jet at $100\%L_c$. Below a Strouhal number of 0.7 tip and trough region length scales are equal to the baseline values. Above this Strouhal number both regions have increased length scales with a larger increase in the trough region.

Figure 7.13 (c) shows the 4° nozzle in comparison to the baseline jet at $100\%L_c$. Below a Strouhal number of 0.8 the tip region length scales are equal to the baseline but above this Strouhal number the tip region length scales are decreased. These are the only high frequency length scales to show a decrease from the baseline. The trough region remains roughly equal to the baseline for all frequencies.

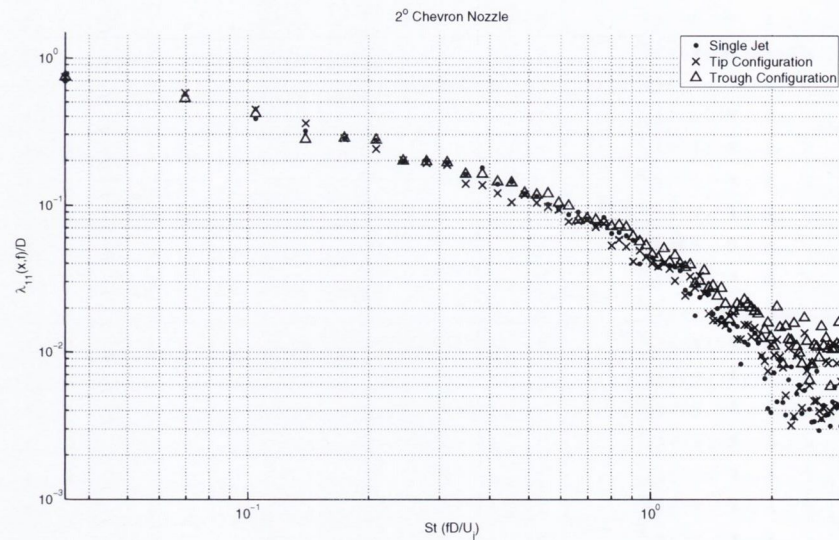
The tip and trough region traditional length scales for the 0° nozzle at $50\%L_c$ are increased above the baseline value by approximately the same amount as the lower scales of the frequency dependent length scales. However the length scales above a Strouhal number of 1 show a 100% increase above the baseline values not seen in the

traditional statistics. The frequency dependent statistics for the 2° nozzle are very close to the baseline and the slight increase found in the traditional statistics may be seen in the length scales above a Strouhal number of 1. The traditional statistics for the 4° nozzle show an increase in the tip region and a decrease in the trough region. This is not reflected in the frequency dependent statistics as both regions are increased at high frequencies above a Strouhal number of 1 and the trough region shows a larger increase. Below this Strouhal number the scatter in the data make both regions appear approximately equal to the baseline value.

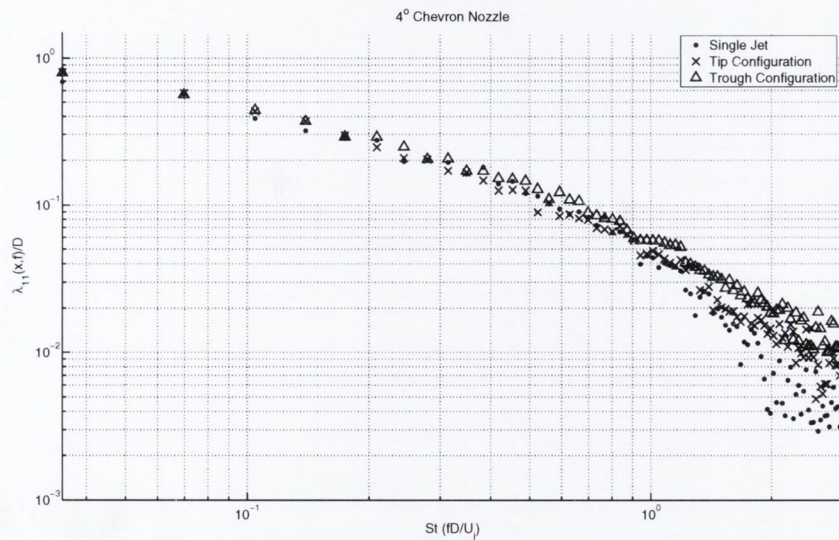
The traditional length scales for the 0° nozzle at $100\%L_c$ are increased above the baseline for both tip and trough regions. The frequency dependent length scales also show an increase for both regions at all frequencies. The 2° nozzle traditional length scales show a decrease for both tip and trough regions. While there is some indication of a decrease at lower Strouhal numbers there is a clear increase in the length scales for both regions at high frequencies. The traditional length scales for the 4° nozzle are very close to the baseline with both regions showing a very slight increase. The frequency dependent length scales for the trough region are very close to the baseline at all frequencies but the tip region length scales are decreased from the baseline values above a Strouhal number of 1.



(a)



(b)

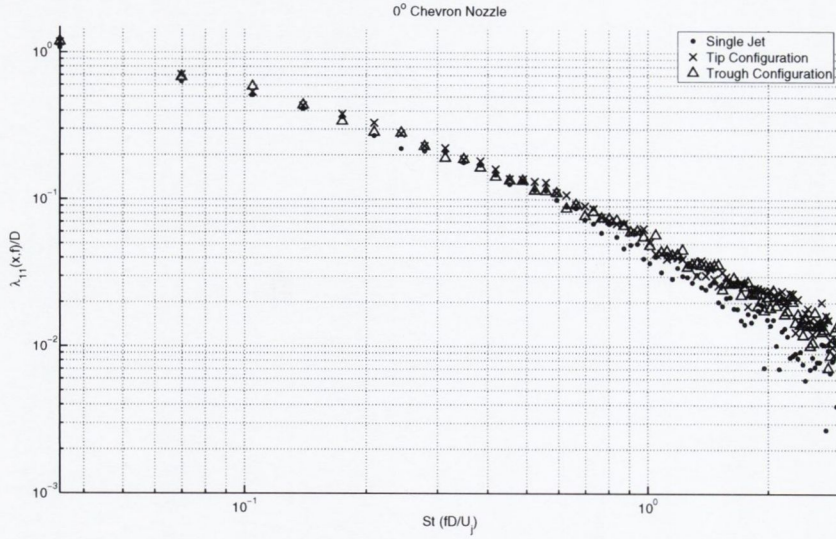


(c)

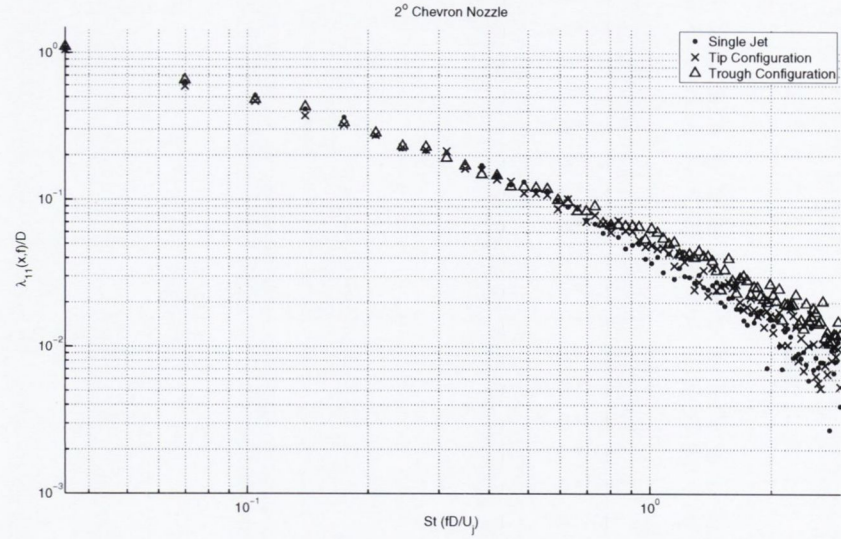
$0.5L_c$	L_c	Fixed Axis (mm)	Moving Axis (mm)	Convection Speed (m/s)
SJ	4.92D	7.96	27.06	41.95
N0 Tip	4.64D	10.10	38.90	44.36
N0 Trough	4.64D	9.36	35.24	41.11
N2 Tip	3.80D	8.41	27.01	41.67
N2 Trough	3.80D	7.66	26.82	40.60
N4 Tip	4.13D	8.71	28.06	40.92
N4 Trough	4.13D	7.43	26.09	38.94

(d)

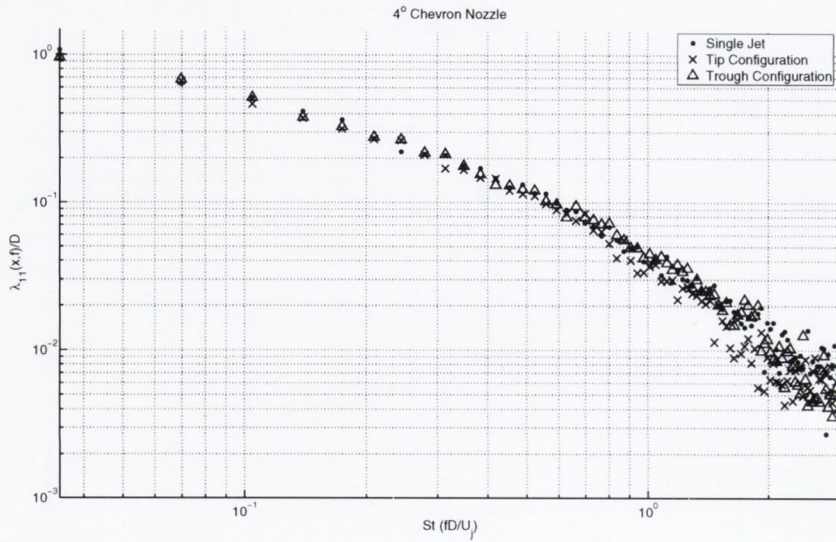
Figure 7.12: Frequency Dependent Fixed Axis Length Scale $u' 50\%L_c$



(a)



(b)



(c)

$1.0L_c$	L_c	Fixed Axis (mm)	Moving Axis (mm)	Convection Speed (m/s)
SJ	4.92D	13.60	47.06	39.73
N0 Tip	4.64D	15.45	55.92	41.44
N0 Trough	4.64D	15.86	56.20	40.18
N2 Tip	3.80D	13.13	46.13	38.48
N2 Trough	3.80D	12.06	43.57	38.64
N4 Tip	4.13D	13.64	48.05	37.40
N4 Trough	4.13D	13.81	49.78	38.74

(d)

Figure 7.13: Frequency Dependent Fixed Axis Length Scale $u' 100\%L_c$

7.2.7 v' Fixed Axis Length Scale

Figures 7.14 and 7.15 show the frequency dependent fixed axis length scale for the v' component in the axial direction. Figure 7.14 (a) shows the 0° nozzle in comparison to the baseline jet at $50\%L_c$. Tip and trough region length scales are increased over the baseline values for all frequencies in this position.

Figure 7.14 (b) shows the 2° nozzle in comparison to the baseline jet at $50\%L_c$. Tip and trough region length scales are increased above the baseline values beyond a Strouhal number of 1. Below this value they are approximately equal to the baseline.

Figure 7.14 (c) shows the 4° nozzle in comparison to the baseline jet at $50\%L_c$. Tip region length scales are slightly increased compared with the baseline values for all frequencies. The trough region also shows an increase for all frequencies but they are significantly increased beyond a Strouhal number of 1.

Figure 7.15 (a) shows the results for the 0° nozzle at $100\%L_c$ there is a slight increase to the length scales for all frequencies for both tip and trough regions.

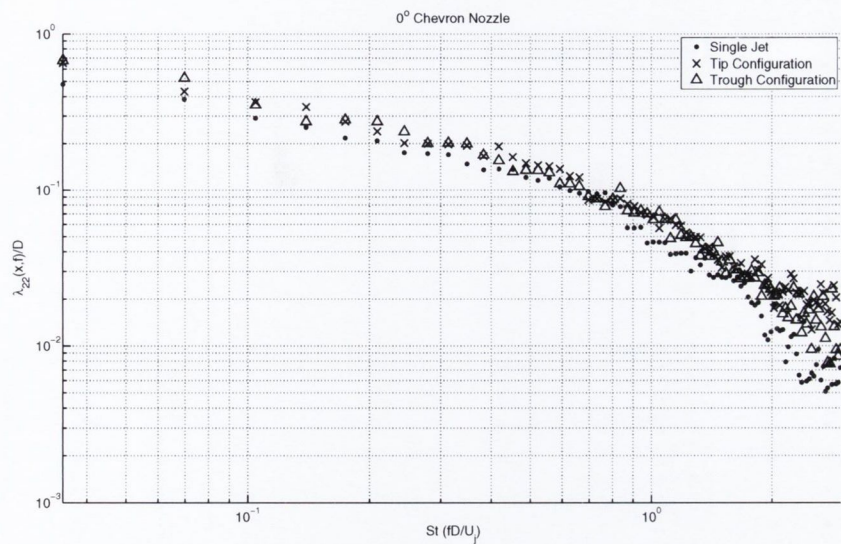
Figure 7.15 (b) shows the 2° nozzle in comparison to the baseline jet at $100\%L_c$. The frequency dependent length scales for both tip and trough regions are approximately equal to the baseline for all frequencies.

Figure 7.15 (c) shows the 4° nozzle in comparison to the baseline jet at $50\%L_c$. This nozzle shows a slight decrease to the length scales beyond a Strouhal number of 1 otherwise the length scales for both tip and trough regions are approximately equal to the baseline.

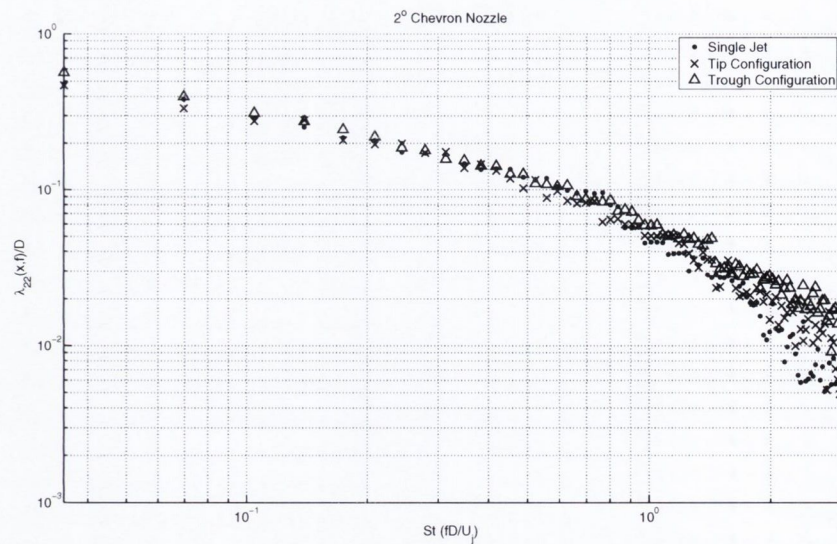
The traditional statistics for the 0° nozzle at $50\%L_c$ show an increase in the length scales of both tip and trough regions with a larger increase in the tip region. The frequency dependent statistics also show increased length scales at all frequencies for both regions but the increase is approximately equal in both regions. The traditional length scales for the 2° nozzle are slightly decreased from the baseline values with a larger decrease in the trough region. The frequency dependent statistics show there is a decrease in the lower frequency length scales for the tip region but both regions show increased length scales above a Strouhal number of 1. The traditional length scales for the 4° nozzle are very close to the baseline values with a slight decrease in

the tip region and a slight increase in the trough region. The frequency dependent statistics are also very close to the baseline below a Strouhal number of 1 with a slight indication of a decrease in the tip region length scales. However above this Strouhal number both regions show an increased length scales with a significant increase in the trough region.

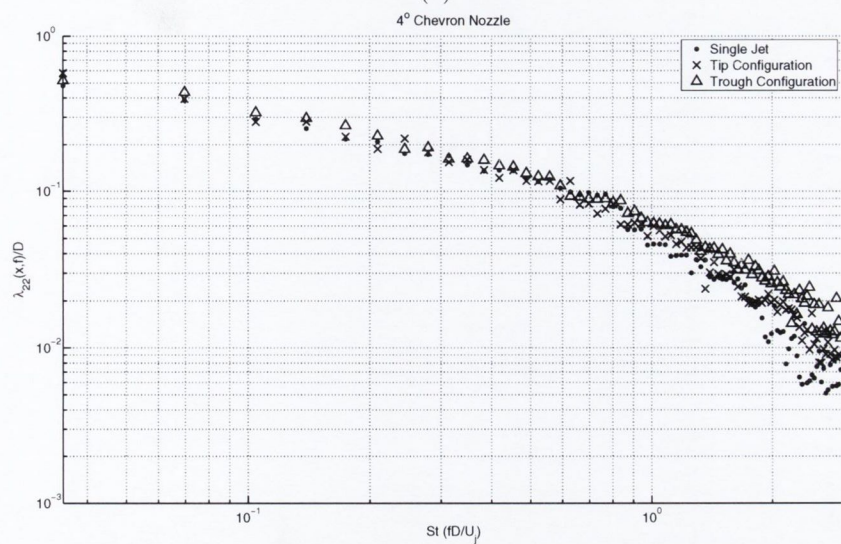
The 0° nozzle frequency dependent length scales show a slight increase for tip and trough regions for all frequencies at $100\%L_c$ which is in agreement with the traditional statistics. The traditional length scales for the 2° nozzle at this position show a decrease however the frequency dependent length scales are approximately equal to the baseline values. The traditional length scales for the 4° nozzle in this position also show a decrease from the baseline. There is a decrease in the frequency dependent length scales for this nozzle at high frequencies.



(a)



(b)

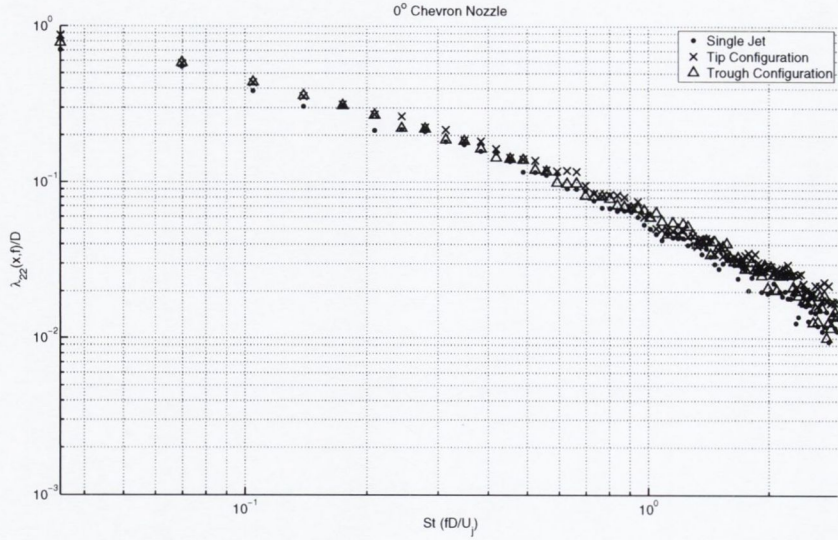


(c)

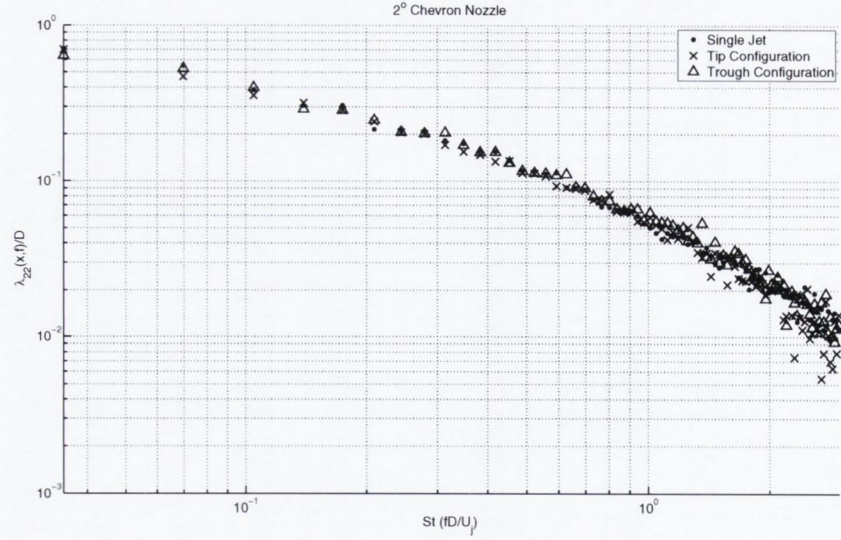
$0.5L_c$	L_c	Fixed Axis (mm)	Moving Axis (mm)	Convection Speed (m/s)
SJ	4.92D	4.54	19.60	52.63
N0 Tip	4.64D	6.18	25.18	50.49
N0 Trough	4.64D	5.63	22.68	43.25
N2 Tip	3.80D	4.00	16.94	51.19
N2 Trough	3.80D	4.34	17.88	41.60
N4 Tip	4.13D	4.48	20.28	41.67
N4 Trough	4.13D	4.69	18.10	36.68

(d)

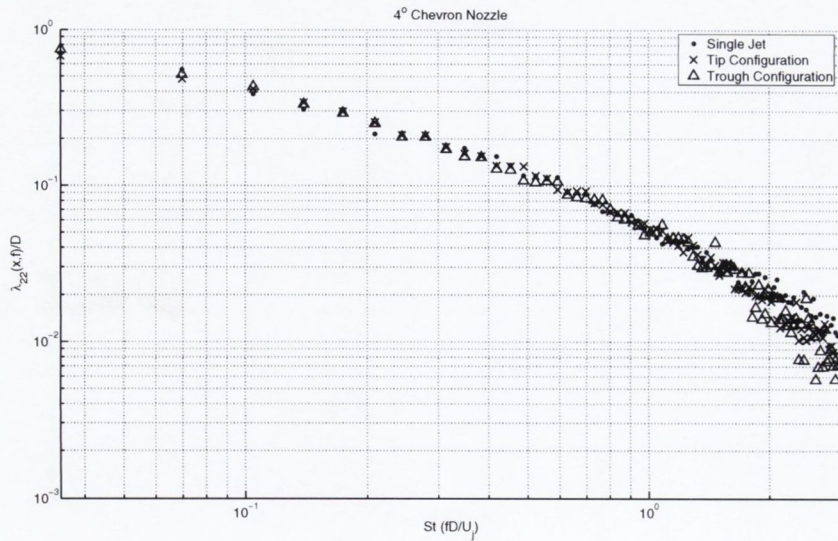
Figure 7.14: Frequency Dependent Fixed Axis Length Scale $v' 50\%L_c$



(a)



(b)



(c)

$1.0L_c$	L_c	Fixed Axis (mm)	Moving Axis (mm)	Convection Speed (m/s)
SJ	4.92D	7.19	27.14	40.16
N0 Tip	4.64D	7.88	31.04	43.58
N0 Trough	4.64D	7.72	30.62	40.95
N2 Tip	3.80D	5.91	22.29	39.45
N2 Trough	3.80D	6.09	22.74	40.28
N4 Tip	4.13D	6.55	25.03	37.19
N4 Trough	4.13D	6.67	23.96	38.87

(d)

Figure 7.15: Frequency Dependent Fixed Axis Length Scale $v' 100\%L_c$

7.2.8 u'^2 Fixed Axis Length Scale

Figures 7.16 and 7.17 show the frequency dependent fixed axis length scale for the u'^2 component in the axial direction. Figure 7.16 (a) shows the 0° nozzle in comparison to the baseline jet at $50\%L_c$. Tip and trough region length scales are increased above the baseline values for all frequencies in this position. A more significant increase is observed above a Strouhal number of 1.

Figure 7.16 (b) shows the 2° nozzle in comparison to the baseline jet at $50\%L_c$. Tip and trough region length scales are approximately equal to the baseline below a Strouhal number of 1.5. Above this Strouhal number there is a slight increase observed.

Figure 7.16 (c) shows the 4° nozzle in comparison to the baseline jet at $50\%L_c$. Below a Strouhal number of 1 both tip and trough region length scales are equal to the baseline. Above this Strouhal number both regions show an increase in the length scales with a more significant increase found in the trough region.

Figure 7.17 (a) shows the 0° nozzle in comparison to the baseline jet at $100\%L_c$. Tip and trough region length scales are increased above the baseline values for all frequencies in this position. A more significant increase is observed above a Strouhal number of 1.

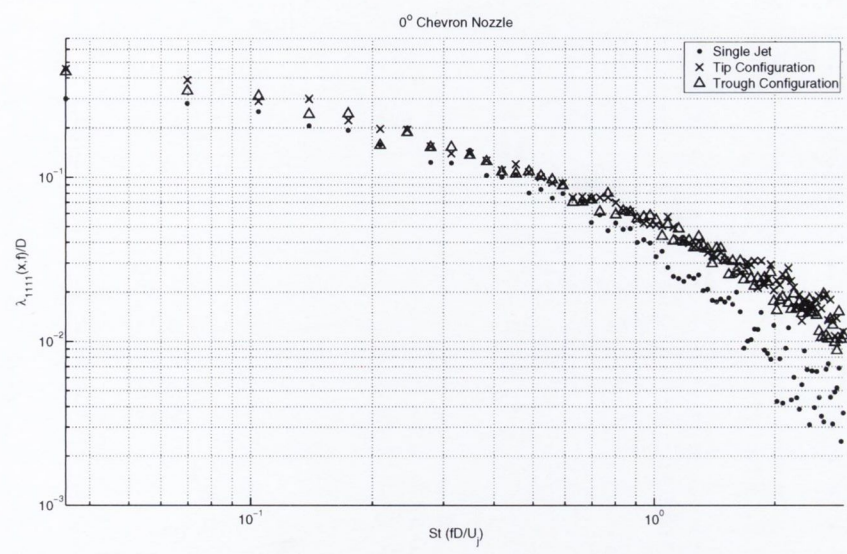
Figure 7.17 (b) shows the 2° nozzle in comparison to the baseline jet at $100\%L_c$. Tip and trough region length scales are equal to the baseline values below a Strouhal number of 1. Above this Strouhal number trough region length scales show a significant increase and tip region length scales show a slight increase.

Figure 7.17 (c) shows the 4° nozzle in comparison to the baseline jet at $100\%L_c$. Tip and trough region length scales are equal to the baseline values below a Strouhal number of 1. Beyond this Strouhal number the tip region length scales are decreased and the trough region length scales remain equal to the baseline.

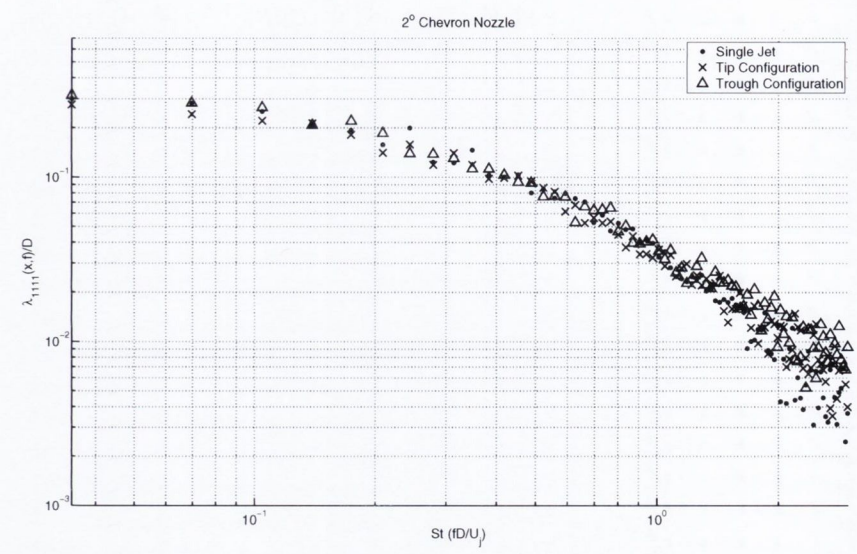
The traditional length scales for the 0° nozzle show an increase over the baseline at $50\%L_c$. This increase is reflected in the frequency dependent statistics however the large increase of almost 100% for Strouhal numbers above 1 is not seen in the traditional statistics. The traditional length scales for the 2° nozzle are decreased from the baseline. While no clear decrease in the frequency dependent length scales is

observed there is an indication of an increased length scale for very high frequencies. The traditional length scale for the 4° nozzle also shows a slight decrease. While no clear decrease in the frequency dependent length scales is observed there is a definite increase in the length scales of the tip and trough region beyond a Strouhal number of 1.

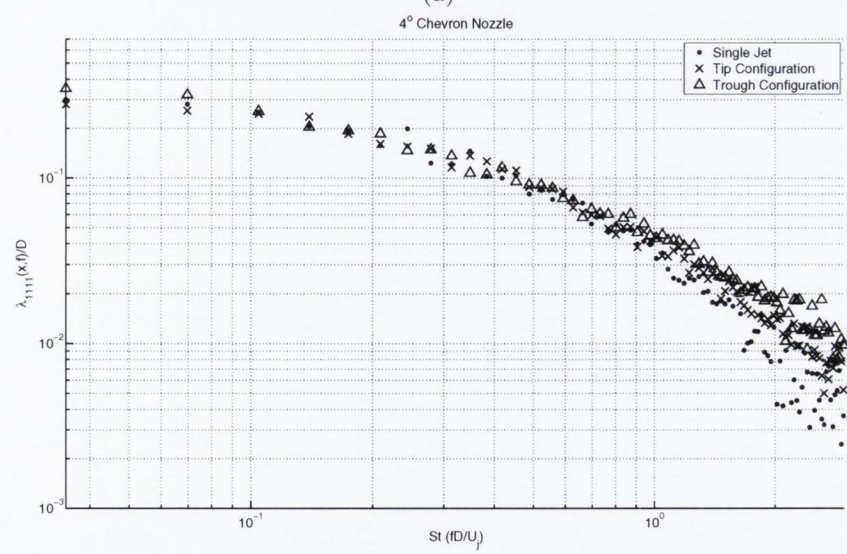
The frequency dependent length scales for the 0° nozzle at $100\%L_c$ show an increase for all frequencies with a more significant effect above a Strouhal number of 1. The traditional statistics also show an increase over the baseline value but the magnitude of the increase corresponds to the increase of the low frequency length scales. The traditional length scales for the 2° nozzle are decreased from the baseline. There is a no clear decrease in the frequency dependent length scales at low frequencies where the values are approximately equal to the baseline and the high frequency length scales show a significant increase. The traditional length scales for the 4° nozzle are slightly increased. The frequency dependent length scales for the trough region are approximately equal to the baseline for all frequencies while the tip region length scales above a Strouhal number of 1 are decreased from the baseline values.



(a)



(b)

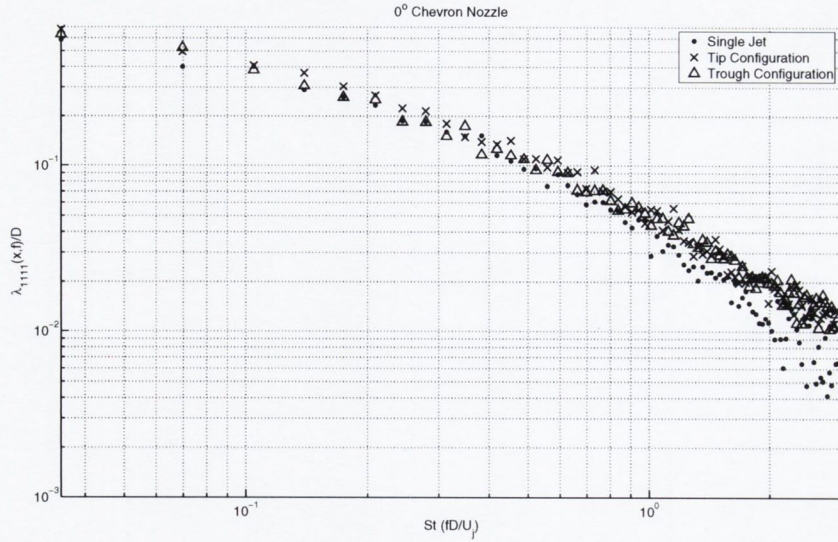


(c)

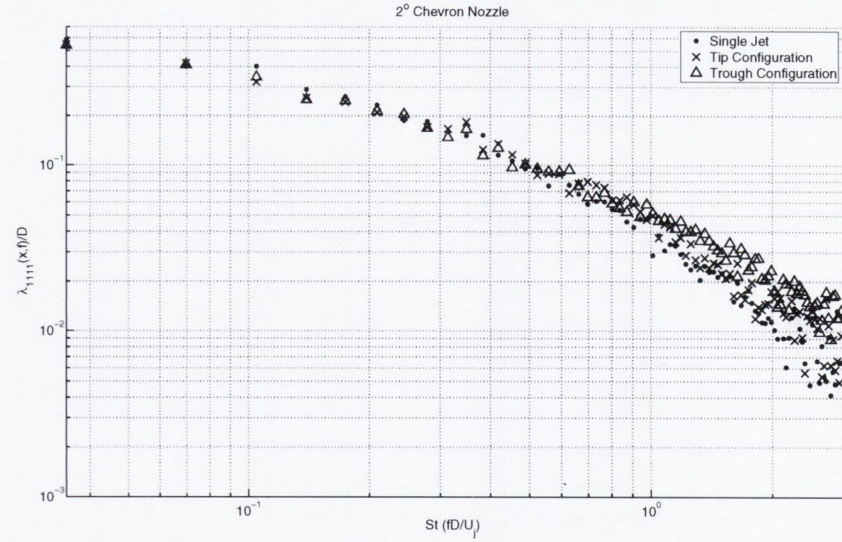
$0.5L_c$	L_c	Fixed Axis (mm)	Moving Axis (mm)	Convection Speed (m/s)
SJ	4.92D	4.05	9.25	37.31
N0 Tip	4.64D	4.80	13.49	37.21
N0 Trough	4.64D	4.54	11.92	27.93
N2 Tip	3.80D	3.72	8.83	48.54
N2 Trough	3.80D	3.84	9.01	21.32
N4 Tip	4.13D	4.00	10.48	45.08
N4 Trough	4.13D	3.75	9.67	27.13

(d)

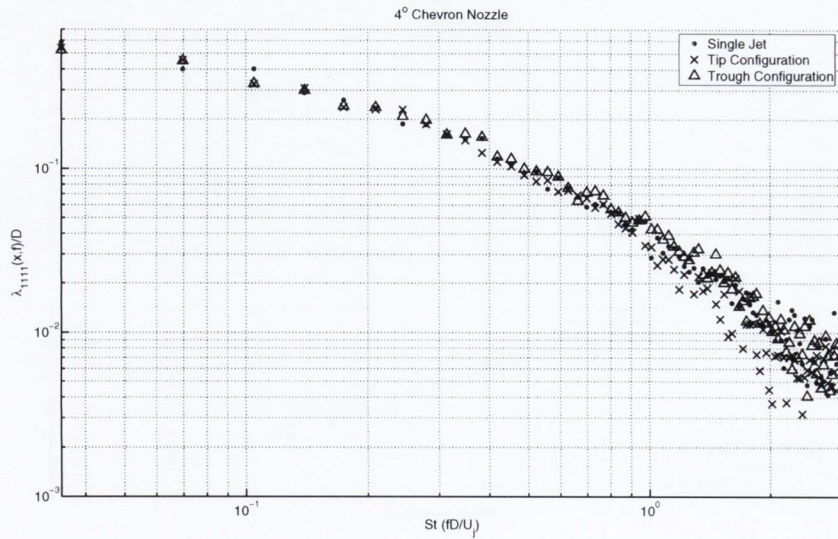
Figure 7.16: Frequency Dependent Fixed Axis Length Scale u'^2 50% L_c



(a)



(b)



(c)

$1.0L_c$	L_c	Fixed Axis (mm)	Moving Axis (mm)	Convection Speed (m/s)
SJ	4.92D	6.53	16.52	47.36
N0 Tip	4.64D	7.16	20.84	44.69
N0 Trough	4.64D	7.19	19.93	44.52
N2 Tip	3.80D	6.33	16.76	44.63
N2 Trough	3.80D	5.49	15.50	44.57
N4 Tip	4.13D	6.66	17.87	44.04
N4 Trough	4.13D	6.78	18.01	45.71

(d)

Figure 7.17: Frequency Dependent Fixed Axis Length Scale $u'^2 \approx 100\%L_c$

7.2.9 v'^2 Fixed Axis Length Scale

Figures 7.18 and 7.19 show the frequency dependent fixed axis length scale for the v'^2 component in the axial direction. Figure 7.18 (a) shows the 0° nozzle in comparison to the baseline jet at $50\%L_c$. Tip and trough region length scales show an increase above the baseline values for all frequencies in this position.

Figure 7.18 (b) shows the 2° nozzle in comparison to the baseline jet at $50\%L_c$. Both tip and trough region length scales are approximately equal to the baseline values in this position.

Figure 7.18 (c) shows the 4° nozzle in comparison to the baseline jet at $50\%L_c$. At this position there is a slight increase to the length scales for all frequencies in both tip and trough regions.

Figure 7.19 (a) shows the 0° nozzle in comparison to the baseline jet at $100\%L_c$. Tip and trough region length scales are increased above the baseline values at all frequencies but the effect is less than in the previous position.

Figure 7.19 (b) shows the 2° nozzle in comparison to the baseline jet at $100\%L_c$. There is a slight decrease in the length scales below a Strouhal number of 0.4 at this position. At all other frequencies the length scales are approximately equal to the baseline.

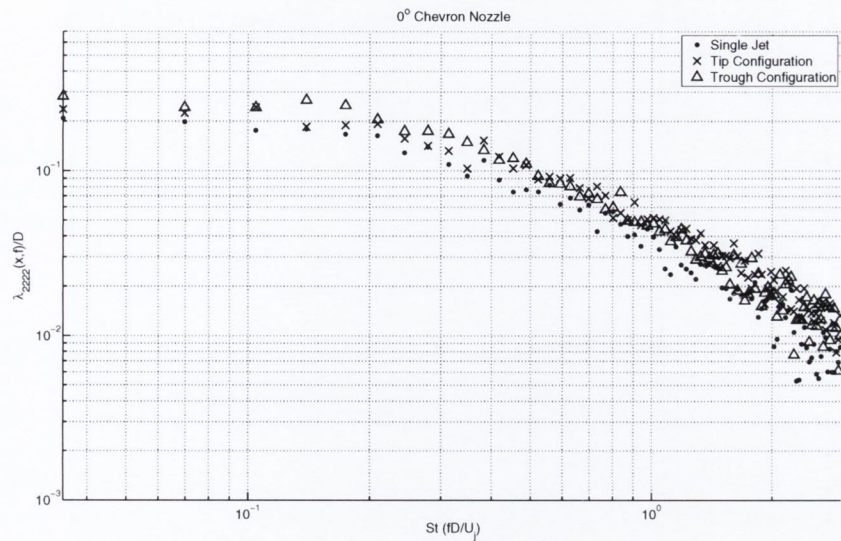
Figure 7.19 (c) shows the 4° nozzle in comparison to the baseline jet at $100\%L_c$. A slight decrease in the length scales below the baseline values is observed for all frequencies.

The traditional statistics for the 0° nozzle show an equal increase over the baseline for both tip and trough regions at $50\%L_c$. A similar increase is observed for both regions in the frequency dependent statistics. The traditional length scales for the 2° nozzle show only a slight decrease from the baseline value. The frequency dependent length scales are also approximately equal to the baseline values. The traditional length scales for the 4° nozzle are closest to the baseline and the frequency dependent length scales are also very close to the baseline values.

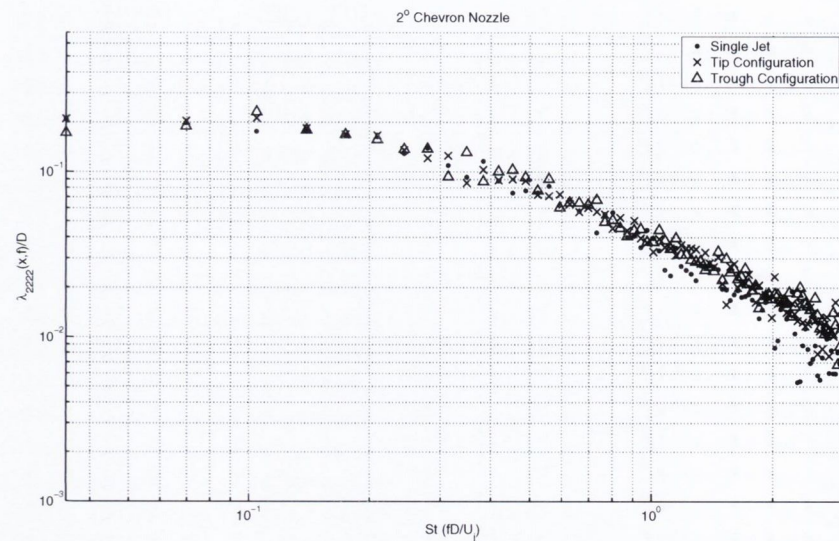
The traditional length scales for the 0° nozzle at $100\%L_c$ are slightly increased over the baseline value and a slight increase is also observed for all frequencies in

7.2. FREQUENCY DEPENDENT LENGTH SCALES

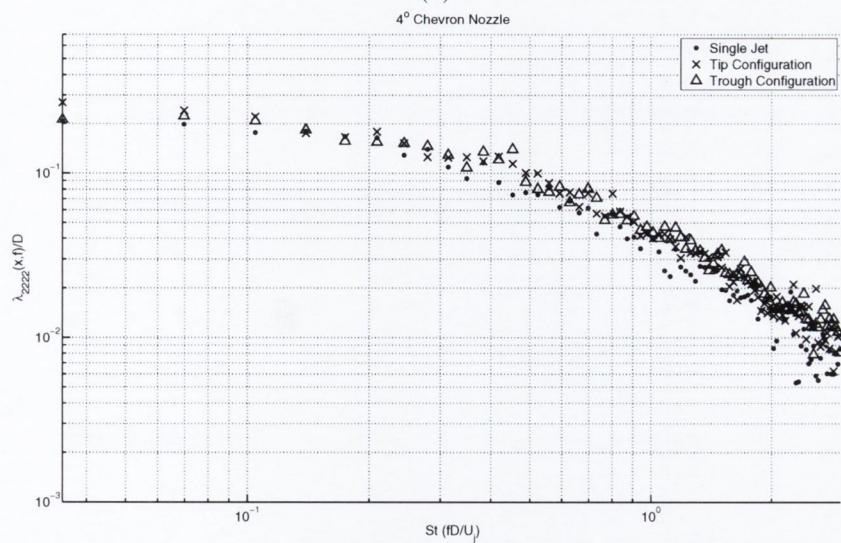
the frequency dependent statistics. The traditional length scales for the 2° nozzle are furthest from the baseline value in this position and are decreased. While there is a slight decrease in the frequency dependent statistics for low Strouhal numbers higher frequencies are approximately equal to the baseline values. The traditional statistics for the 4° nozzle at $100\%L_c$ are slightly decreased and a slight decrease is also observed for all frequencies of the frequency dependent length scales.



(a)



(b)

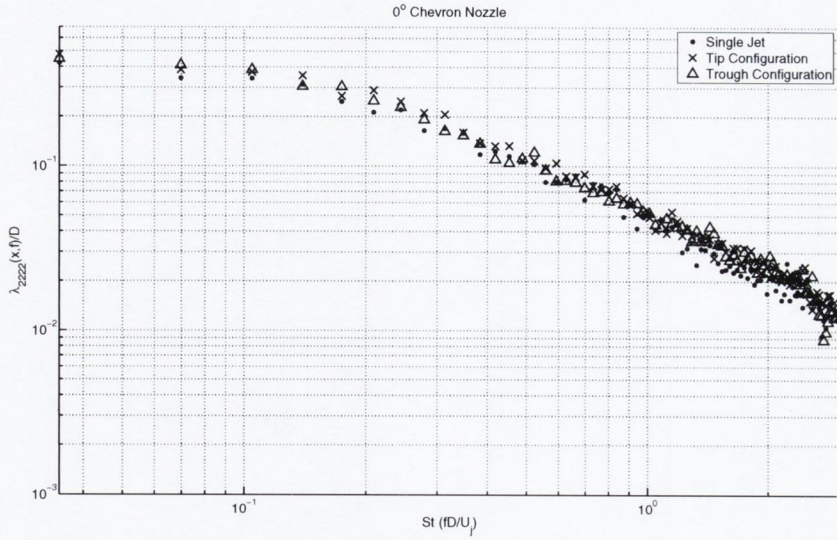


(c)

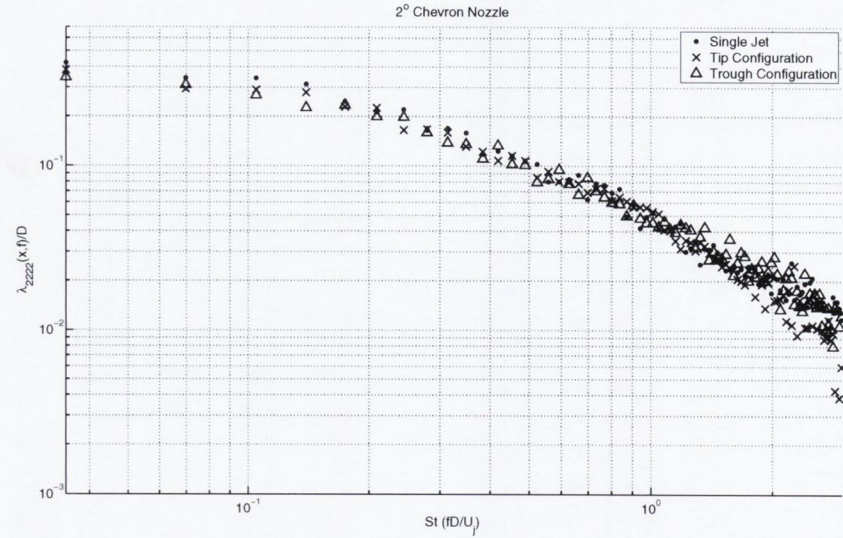
$0.5L_c$	L_c	Fixed Axis (mm)	Moving Axis (mm)	Convection Speed (m/s)
SJ	4.92D	2.66	5.79	53.76
N0 Tip	4.64D	3.37	8.28	56.65
N0 Trough	4.64D	3.37	7.26	58.16
N2 Tip	3.80D	2.49	6.39	50.07
N2 Trough	3.80D	2.42	5.72	28.61
N4 Tip	4.13D	2.77	7.67	41.83
N4 Trough	4.13D	2.53	5.76	28.71

(d)

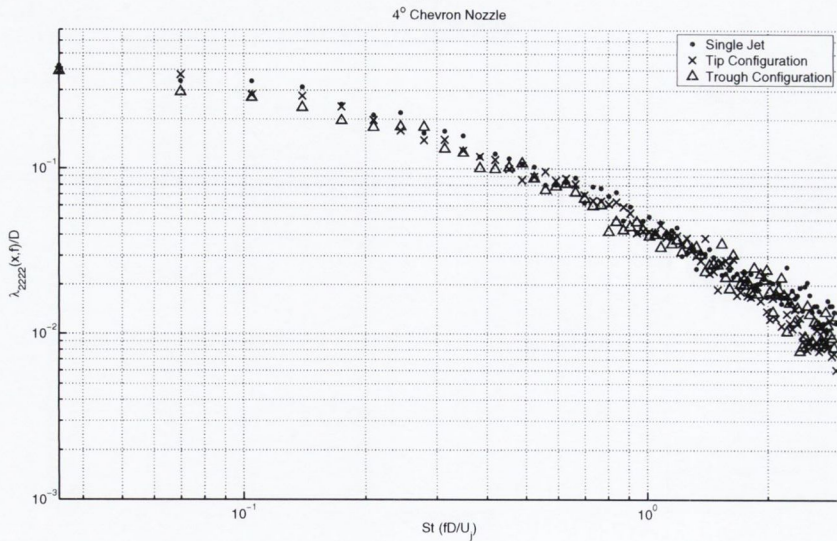
Figure 7.18: Frequency Dependent Fixed Axis Length Scale $v'^2 50\%L_c$



(a)



(b)



(c)

$1.0L_c$	L_c	Fixed Axis (mm)	Moving Axis (mm)	Convection Speed (m/s)
SJ	4.92D	4.40	10.00	50.15
N0 Tip	4.64D	4.69	11.88	51.04
N0 Trough	4.64D	4.77	11.95	48.71
N2 Tip	3.80D	3.60	8.79	50.41
N2 Trough	3.80D	3.66	8.79	50.83
N4 Tip	4.13D	3.96	9.98	49.81
N4 Trough	4.13D	4.01	9.47	46.65

(d)

Figure 7.19: Frequency Dependent Fixed Axis Length Scale $v'^2 \ 100\%L_c$

7.2.10 $u'v'$ Fixed Axis Length Scale

Figures 7.20 and 7.21 show the frequency dependent fixed axis length scale for the $u'v'$ component in the axial direction. Figure 7.20 (a) shows the 0° nozzle in comparison to the baseline jet at $50\%L_c$. Tip and trough region length scales are increased above the baseline values for all frequencies. A more significant increase is observed above a Strouhal number of 1.

Figure 7.20 (b) shows the 2° nozzle in comparison to the baseline jet at $50\%L_c$. Tip and trough regions show a slight increase to the length scales above the baseline values at all frequencies.

Figure 7.20 (c) shows the 4° nozzle in comparison to the baseline jet at $50\%L_c$. Both tip and trough region length scales show an increase above the baseline values at all frequencies.

Figure 7.21 (a) shows the 0° nozzle in comparison to the baseline jet at $100\%L_c$. Tip and trough regions show increased length scales for all frequencies. The increase is less significant than for the previous position.

Figure 7.21 (b) shows the 2° nozzle in comparison to the baseline jet at $100\%L_c$. Both tip and trough region length scales are approximately equal to the baseline for all frequencies.

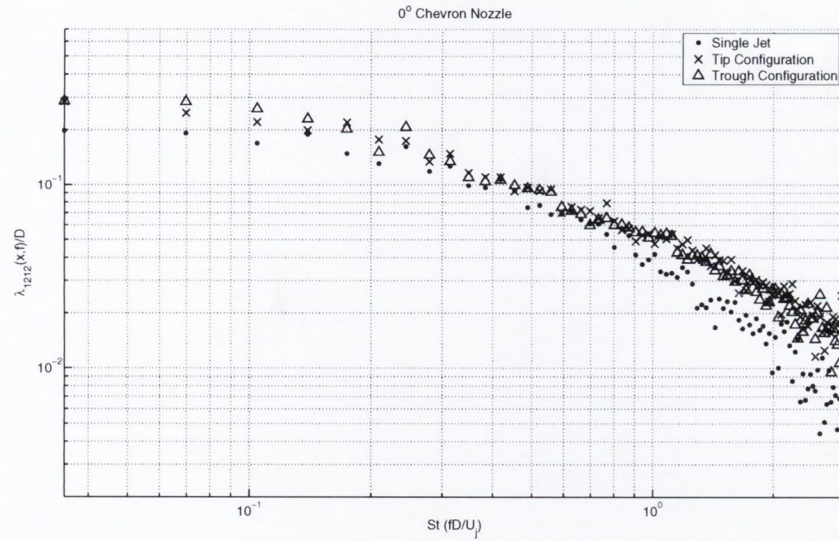
Figure 7.21 (c) shows the 4° nozzle in comparison to the baseline jet at $100\%L_c$. Both tip and trough region length scales are approximately equal to the baseline below a Strouhal number of 1 and there is a slight decrease in the tip region length scales beyond this Strouhal number.

An interesting point to note is that all of the traditional $u'v'$ length scales for the chevron nozzles at $50\%L_c$ are increased over the baseline value. This is also true for the frequency dependent statistics as all chevron nozzles show increased length scales at all frequencies. The largest increases are for the 0° nozzle with the second largest increases for the 4° nozzle and the 2° nozzle having the lowest increases above the baseline value. This is true for both the traditional and frequency dependent statistics.

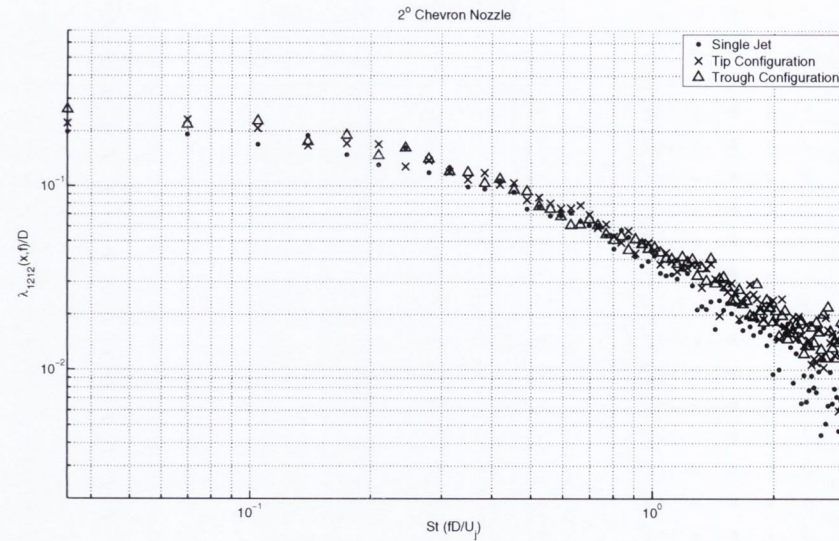
The situation has changed significantly at $100\%L_c$ as the traditional length scales

7.2. FREQUENCY DEPENDENT LENGTH SCALES

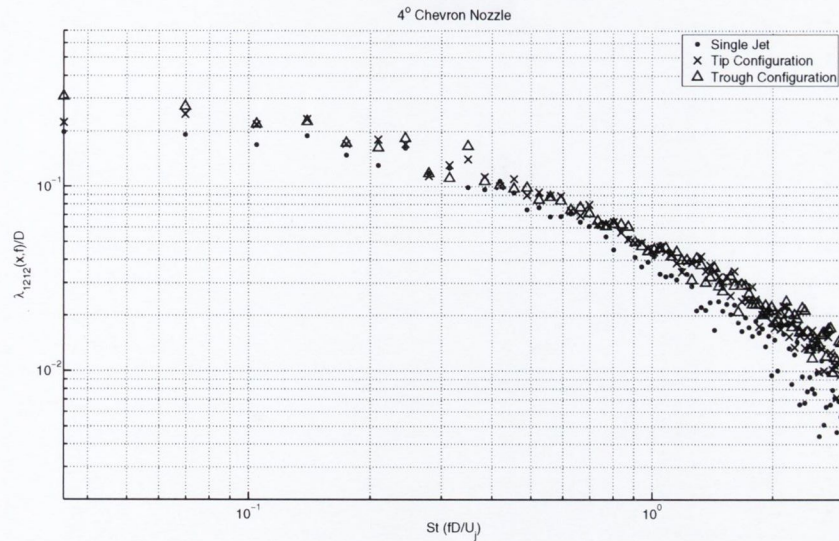
for the 2° nozzle are significantly decreased from the baseline and the 4° nozzle tip region shows a slight decrease. The 0° nozzle frequency dependent length scales are still increased at all frequencies. The 2° nozzle frequency dependent length scales show no clear decrease due to the scatter in the data but there is a slight indication of a decrease for low frequencies. The traditional statistics for the 4° nozzle are very close to the baseline values. There is a slight decrease in the frequency dependent length scales for the tip region beyond a Strouhal number of 1 but otherwise the length scales are very close to the baseline values.



(a)



(b)

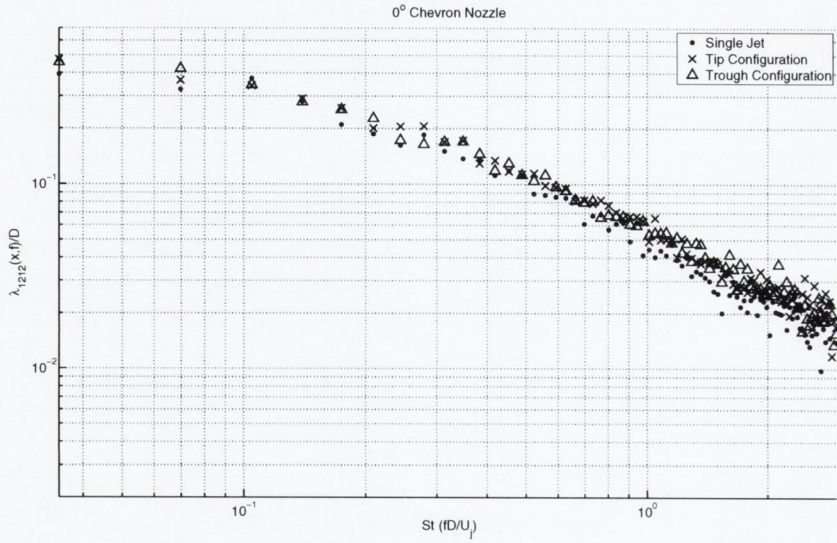


(c)

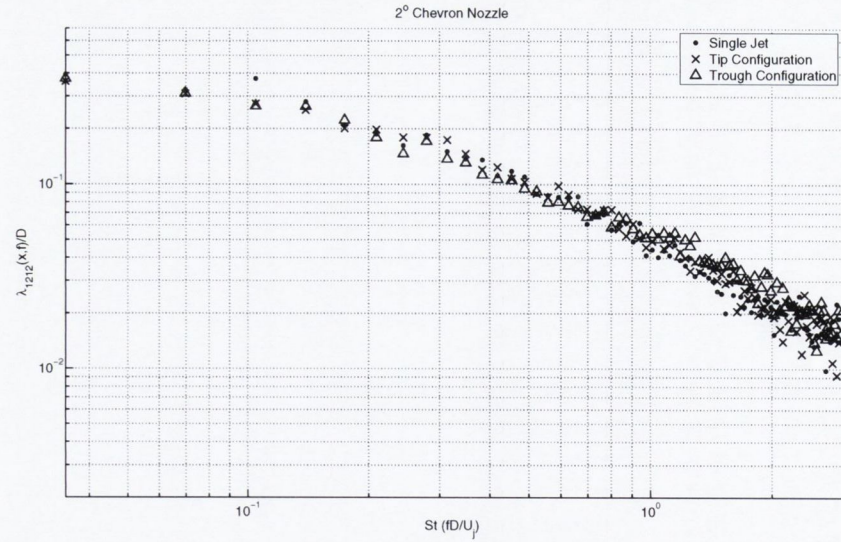
$0.5L_c$	L_c	Fixed Axis (mm)	Moving Axis (mm)	Convection Speed (m/s)
SJ	4.92D	2.55	7.22	50.08
N0 Tip	4.64D	3.21	9.66	49.27
N0 Trough	4.64D	3.04	8.87	46.88
N2 Tip	3.80D	2.78	8.10	48.06
N2 Trough	3.80D	2.71	7.40	45.68
N4 Tip	4.13D	3.00	8.71	46.93
N4 Trough	4.13D	2.96	8.01	42.56

(d)

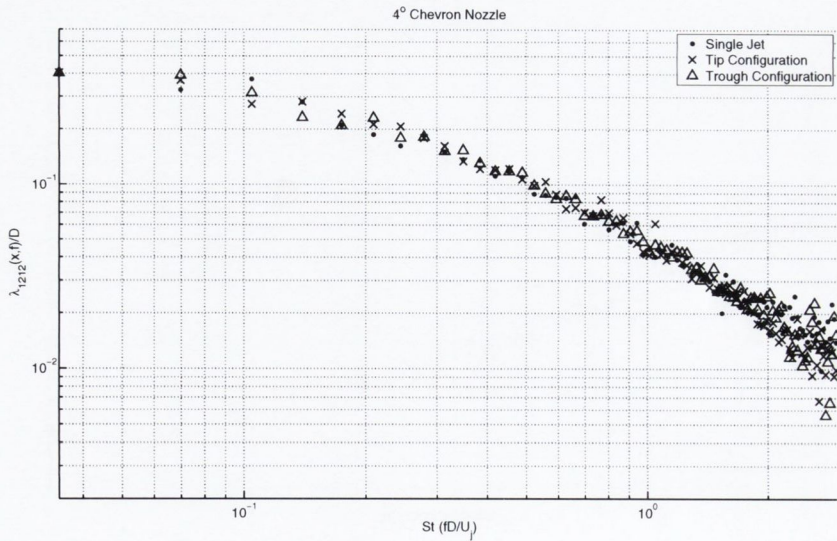
Figure 7.20: Frequency Dependent Fixed Axis Length Scale $u'v'$ $50\%L_c$



(a)



(b)



(c)

$1.0L_c$	L_c	Fixed Axis (mm)	Moving Axis (mm)	Convection Speed (m/s)
SJ	4.92D	4.43	12.25	46.50
N0 Tip	4.64D	4.72	14.51	47.22
N0 Trough	4.64D	4.76	14.36	46.30
N2 Tip	3.80D	3.89	11.36	46.58
N2 Trough	3.80D	3.63	10.62	46.39
N4 Tip	4.13D	4.38	12.43	43.07
N4 Trough	4.13D	4.49	12.66	46.13

(d)

Figure 7.21: Frequency Dependent Fixed Axis Length Scale $u'v'$ 100% L_c

7.3 Comparison of u' and v' Length Scales

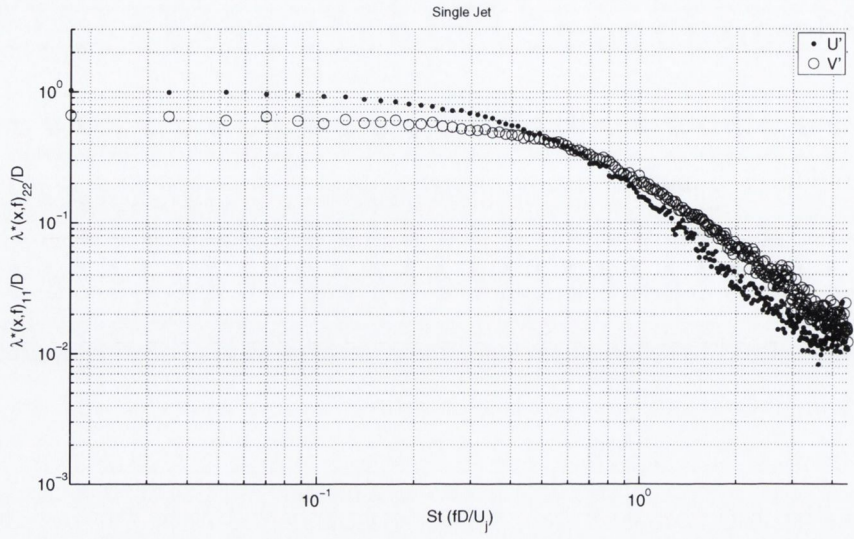
A significant result of the PIV investigation was the change in the ratio of the u' to v' turbulence. This change was investigated along the nozzle lip line and it was found to be most significant in the nozzle region of $0 - 2D$ downstream. Beyond $4D$ the ratio was approximately equal to the values in the baseline case. In order to further understand these changes the length scales of the u' and v' turbulence are also compared in figures 7.22 and 7.23. Due to the large number of nozzle configurations only the 0° nozzle is presented here and compared against the baseline as this nozzle showed the largest change in the ratio of the turbulence in the PIV investigation. The frequency dependent moving axis length scale was chosen over the fixed axis length scale as there was less scatter in the data than for the fixed axis length scales.

Figure 7.22 shows the frequency dependent moving axis length scales for u' and v' for the baseline jet at the three measurement positions of $50\%L_c$, $75\%L_c$ and $100\%L_c$. There is a clear transitional point at a Strouhal number of 0.6 for all positions beyond which the v' length scales are larger than the u' length scales.

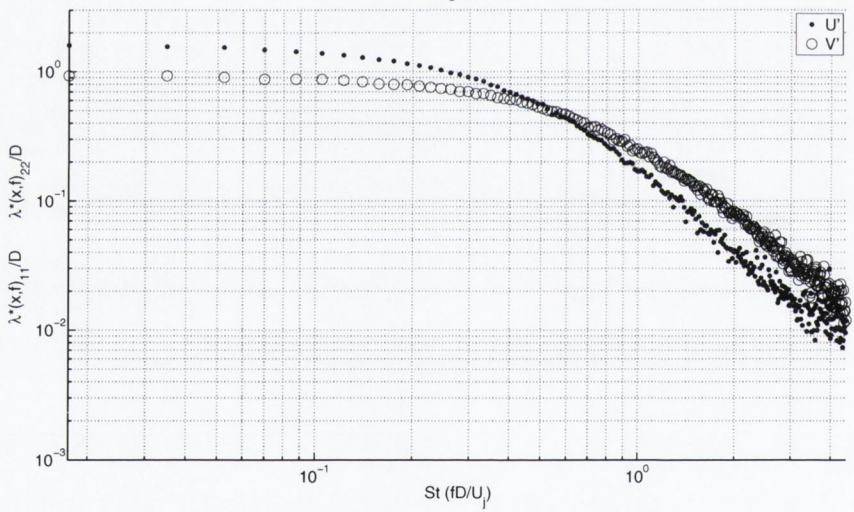
Figure 7.23 shows the same comparison for the 0° nozzle. There is a significant difference to the baseline nozzle as for the $50\%L_c$ and $75\%L_c$ positions the u' length scales remains larger than the v' length scales up to a Strouhal number of 1 and beyond this Strouhal number the length scales are equal. For the $100\%L_c$ position the u' length scale drops below the v' length scale at a Strouhal number of 0.7 but the difference between the two is still significantly less than the baseline nozzle.

The PIV study indicated that chevron nozzles produced more isotropic turbulence especially in the nozzle region. These results also indicate that the axial length scales of the two turbulence quantities are equal for the smaller turbulence scales in chevron nozzles. The fact that the u' length scales are smaller for the $100\%L_c$ position indicates that the turbulence is beginning to recover from the effects of the nozzle by this position. This is in agreement with the PIV results which showed the turbulence ratio reverted to the baseline case by approximately $4D$ downstream.

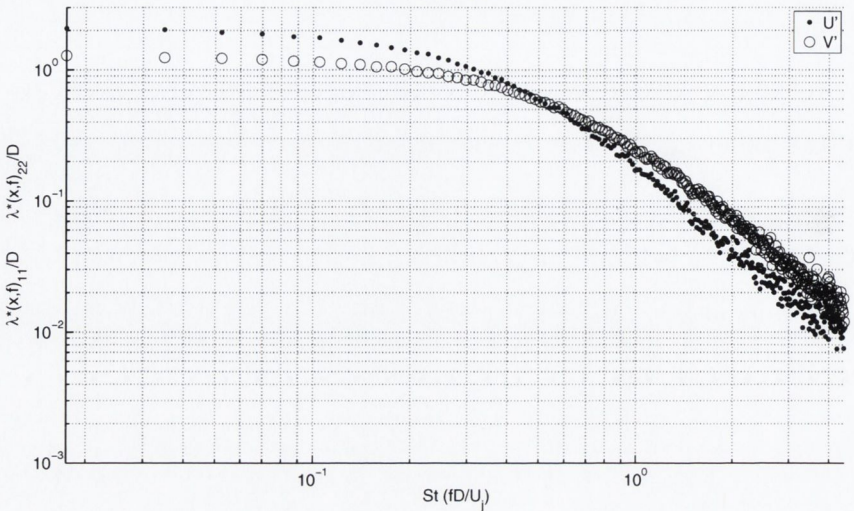
7.3. COMPARISON OF u' AND v' LENGTH SCALES



(a) 50% L_c



(b) 75% L_c



(c) 100% L_c

Figure 7.22: Moving Axis Length Scale u' to v' Comparison: Single Jet

7.3. COMPARISON OF u' AND v' LENGTH SCALES

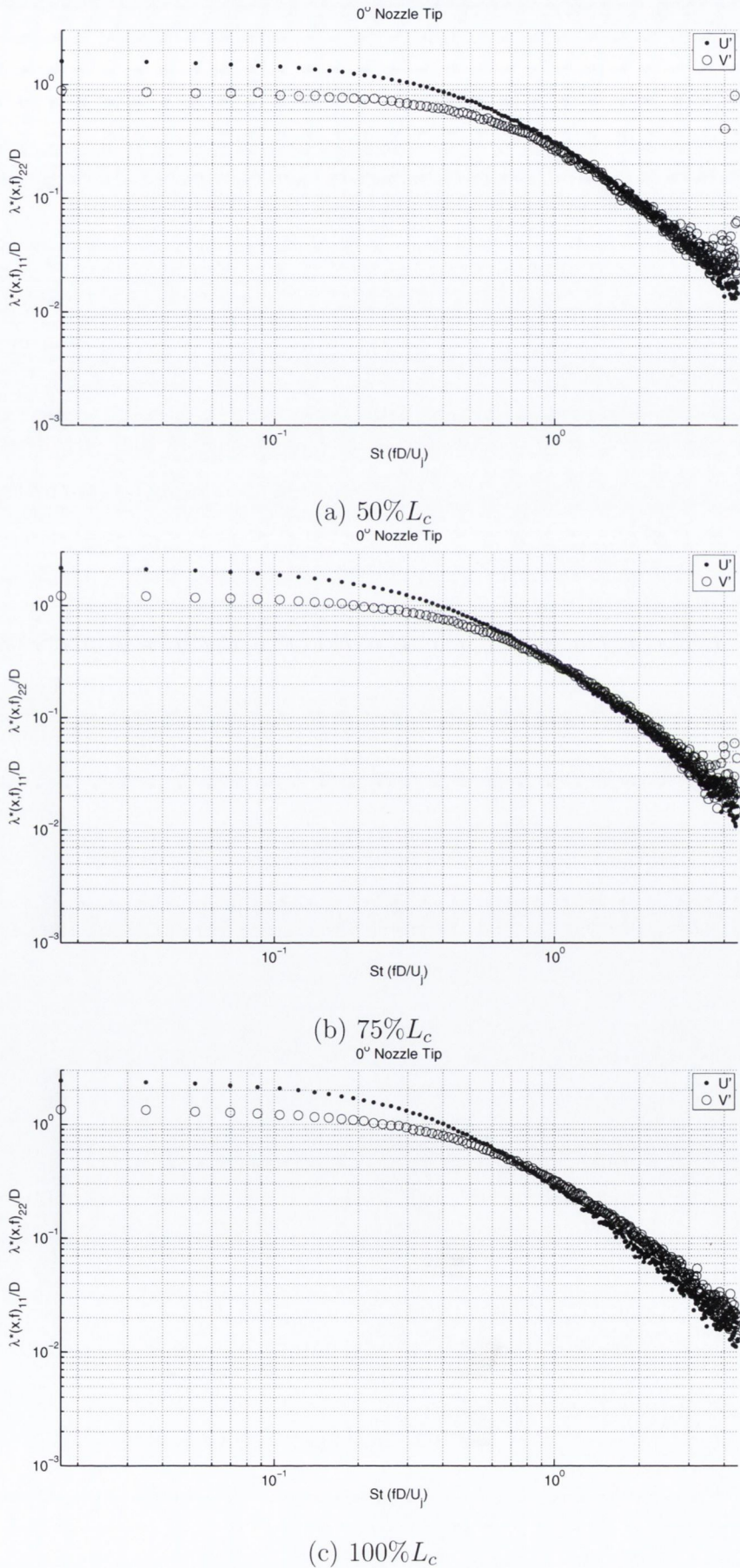


Figure 7.23: Moving Axis Length Scale u' to v' Comparison: 0° Nozzle

7.4 Local Strouhal Number

Aeroacoustic prediction codes require the use of statistical modeling of the turbulence. One of the general assumptions made is the the nature of the turbulence is the same at all locations in the jet. This investigation has revealed that significant differences exist over the potential core region of the jet between the various chevron nozzles and the baseline case. Existing CFD codes can provide values for the local bulk turbulence length scales and this section investigates if there is a common relationship between the bulk statistics and the frequency dependent statistics. If such a relationship exists it would justify many assumptions on the nature of the turbulence. This was attempted by non-dimensionalising the frequency dependent statistics using the local bulk statistics for each nozzle. Figures 7.24 and 7.25 show the fixed and moving axis u' length scales for all nozzles non-dimensionalised using local statistics. The frequency dependent length scales $\lambda_{11}(x, f)$ and $\lambda_{11}^*(x, f)$ are non-dimensionalised using the traditional length scales $\lambda_{11}(x)$ and $\lambda_{11}^*(x)$. In addition the length scales are plotted as a function of a Strouhal number based on the local length scale and convection speed as outlined below

$$St(x, f) = \frac{f \lambda_{11}(x)}{U_c(x)}$$

$$St(x, f) = \frac{f \lambda_{11}^*(x)}{U_c(x)}$$

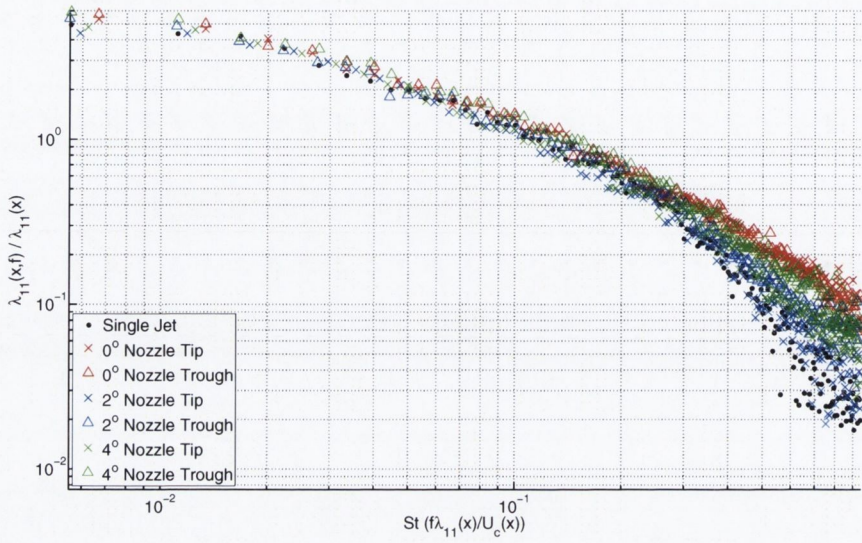
The results for the fixed axis length scales show an excellent collapse of the data for the low frequency turbulent scales and some interesting results for the higher frequencies. Figure 7.24 (a) shows the results at 50% L_c and for this position there is significant variation between nozzles. There are also tip to trough region differences for the 2° and 4° nozzles. Figure 7.24 (b) shows the fixed axis length scales at 75% L_c . For this position the tip to trough region differences have dissipated and all of the chevron nozzles have collapsed to approximately the same values but not onto the baseline case. Figure 7.24 (c) shows the fixed axis length scales at 100% L_c . The 4° nozzle length scales are now equal to the baseline for the entire Strouhal number range. The other two nozzles are equal to the baseline below a Strouhal number of 1 but the

length scales are still larger beyond this Strouhal number.

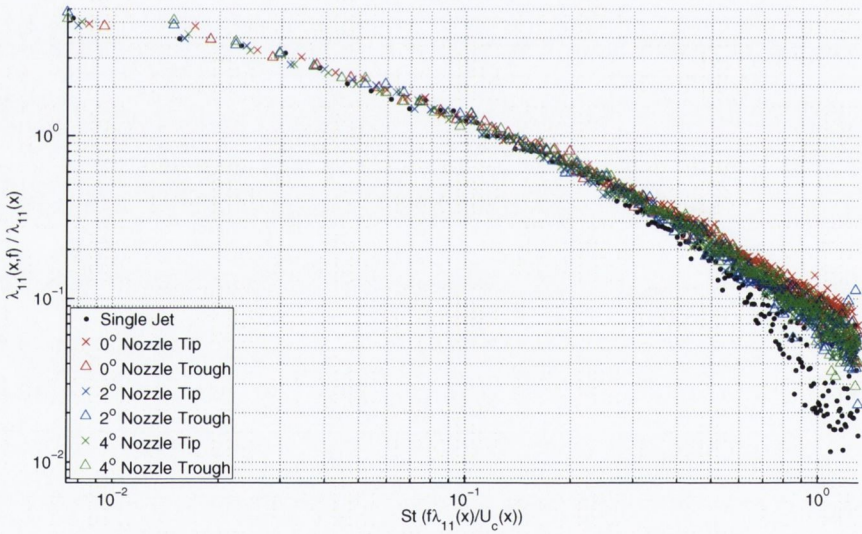
The moving axis length scale shows very similar results to the fixed axis length scale. Figure 7.25 (a) shows the length scales at $50\%L_c$ as was seen previously the data collapses very well for the lower frequencies but there are significant differences between nozzles at this position. The 2° nozzle tip region is very similar to the baseline for the whole Strouhal number range in this position. By the $75\%L_c$ position the tip to trough region differences have disappeared but there is a clearer difference between the nozzles than for the fixed axis length scales. The 2° nozzle is closest to the baseline at higher Strouhal numbers with the 4° nozzle length scales having slightly higher values and the 0° nozzle furthest from the baseline. The 4° nozzle is very close to the baseline at $100\%L_c$ as shown in figure 7.25 (c). The 0° nozzle is furthest from the baseline and the 2° nozzle length scales lie between the other two chevron nozzles. The 4° nozzle had a very fast collapse to the baseline values between the $75\%L_c$ and $100L_c$ positions.

The excellent collapse of the low frequency turbulence scales may be further indication that the traditional statistics are driven by these larger scales. It is therefore not surprising that the use of the bulk statistics was successful at collapsing these scales. However the behavior of the high frequency scales may have some important implications. Several important noise prediction models make assumptions on the nature of the fine scale turbulence. The high frequency length scales initially behave very differently for each nozzle but begin to converge further downstream. The high frequency length scales are increasing for all nozzles further downstream from the nozzle exit and this may be an indication that the fine scale turbulence eventually evolves to a have common structure for all jets. However if this is the case it is clear that the nozzle can have an important impact on how quickly this theoretical structure develops. It may therefore be necessary for models based on assumptions on the nature of the fine scale turbulence to take account of the variations over the potential core length where the turbulence is clearly still evolving towards this theoretical structure.

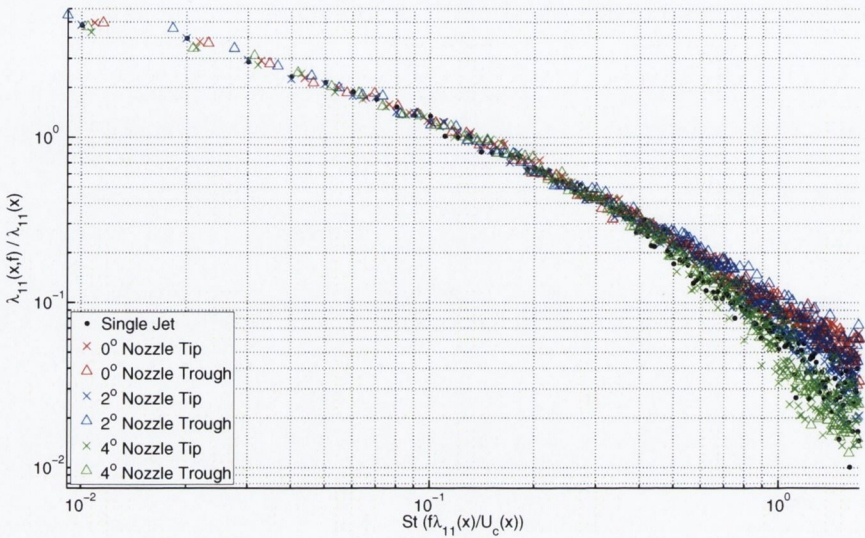
7.4. LOCAL STROUHAL NUMBER



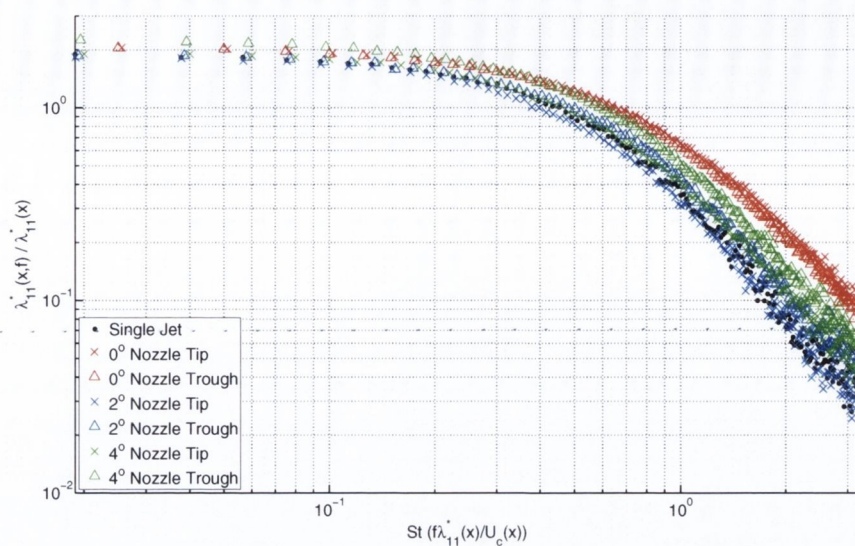
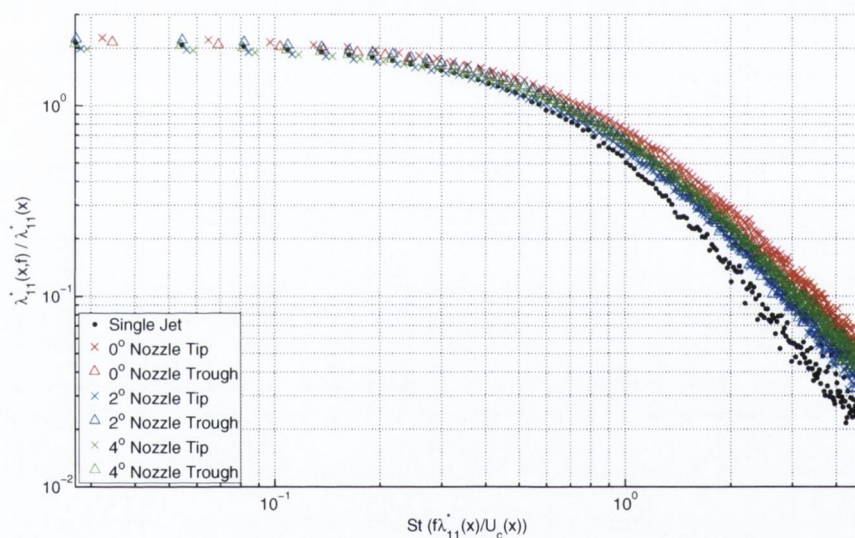
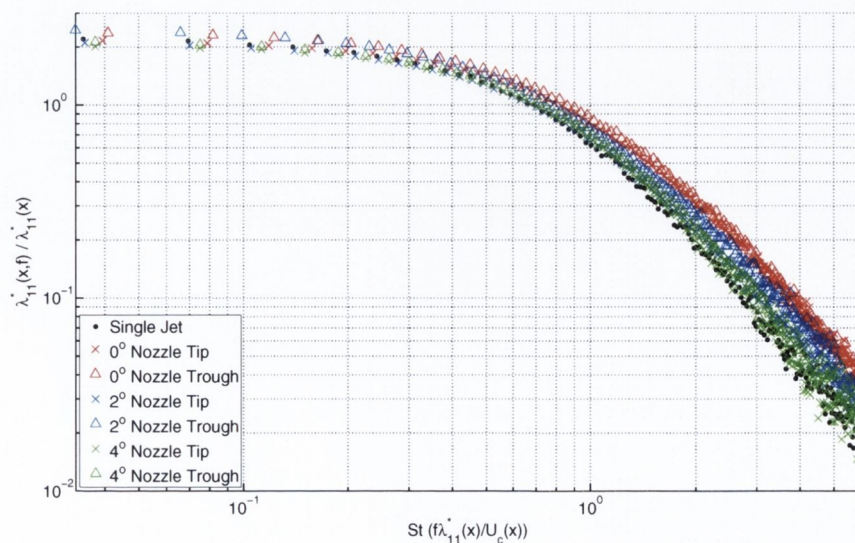
(a) 50% L_c



(b) 75% L_c



(c) 100% L_c

(a) 50% L_c (b) 75% L_c (c) 100% L_c

7.5 Discussion

Significant differences have been identified in the turbulence statistics for the chevron nozzles in comparison to the baseline nozzle. In addition the immersion of chevrons into the flow produces further significant changes to the statistics. The implications for noise source modeling will be discussed in the following chapter and an attempt will be made to draw some conclusions for the method of noise reduction. Firstly an overview of the changes for each nozzle will be given here.

0° Nozzle - This nozzle produced a significant increase in the traditional fixed and moving axis length scales. The effect was more prominent in the v' and v'^2 length scales with showed increases up to 43% from the baseline values. The differences from the baseline values lessened further from the nozzle and while tip to trough region differences existed at $50\%L_c$ these had decayed by the $75\%L_c$ and $100\%L_c$ positions. The frequency dependent statistics showed that this nozzle increased the length scales for all frequencies but that increase was not equal for all scales of the turbulence. The u' and u'^2 length scales showed increases of up to 100% for the higher frequencies but the lower frequencies were less dramatically affected. The v' and v'^2 length scales showed larger increases for the lower frequencies than the higher frequencies. This clearly demonstrates that the traditional statistics are been driven be the larger scales of the turbulence and are hiding the fact than different scales of the turbulence are being affected differently by the chevrons. This nozzle can be characterised by a global increase to all length scales with relatively equal effects in tip and trough regions.

2° Nozzle - This nozzle had values very close to the baseline for the $50\%L_c$ tests in both the traditional and frequency dependent statistics. This is significant as this nozzle had the largest reduction in potential core length which implies than the turbulence has evolved to the levels found in the baseline nozzle much faster. Unlike the 0° nozzle which showed the largest differences to the baseline at $50\%L_c$ this nozzle is most similar to the baseline at $50\%L_c$. Beyond this point the turbulence structures evolve very differently to the baseline. As you

move further from the nozzle the traditional statistics decrease in comparison to the baseline with a more significant reduction for the v' component. This is further evidence that the traditional statistics are being driven by the larger turbulent structures as the frequency dependent length scales show that the higher frequencies are actually increased over the baseline. The tip and trough regions of this nozzle also show significant differences with the tip region length scales generally being larger. This nozzle can be characterised by a decrease in the length scales for low frequencies and an increase in the length scales for high frequencies.

4° Nozzle - The traditional length scales for this nozzle were most similar to the baseline of any chevron nozzle. The tip region length scales were generally larger close to the nozzle and the trough region length scales larger at the end of the potential core but all were very close to the baseline values. The frequency dependent length scales were also the closest to the baseline values. The v' and v'^2 frequency dependent length scales were in particular extremely close to the baseline values for all positions. The u' and u'^2 length scales show a difference to the baseline at high frequencies where they are increased close to the nozzle and decreased at the end of the potential core. This is the only nozzle to show decreased length scales at high frequencies. There are also tip to trough region differences at many locations for this nozzle. Generally they exist closest to the nozzle and more strongly for the u' component. The trends for this nozzle are less clear than for the other chevron nozzles. This nozzle has shown both increases and decreases to the turbulent length scales at all frequencies in different locations. The PIV investigation showed the largest tip to trough region differences for this nozzle and as a result the two regions may be having separate effects on the turbulent length scales at different locations in the flow. As previously mentioned both the front and back surfaces of the chevrons of this nozzle are immersed into the flow and this may be reducing their effectiveness.

The chevron nozzles behaved significantly differently from each other and from the baseline. Generally they had separate effects on two areas of the turbulence spectra

- The larger turbulent scales below a Strouhal number of $0.7 - 1$
- The small scale turbulence above this Strouhal number

The separate effects on these two regions of the turbulence spectra were further highlighted by the examination of the ratio of the u' and v' length scales and the use of a Strouhal number based on local statistics. The ratio of the u' to v' length scales revealed that the most significant changes occur at high frequencies where the two length scales become equal for the 0° nozzle. These sort of changes are hidden by the traditional statistics which seem to be driven by the larger scales of the turbulence.

The local Strouhal number proved to be very successful at collapsing the low frequency length scales but also highlighted different behavior for each nozzle for the higher frequency length scales. The chevron nozzles were all significantly different at the $50\%L_c$ positions and showed tip to trough region differences. The 2° actually moved further away from the baseline turbulence length scales by the end of the potential core. The 4° nozzle is very similar to the baseline by the end of the potential core and the 0° nozzle moves closer to the baseline in each position. This is perhaps an indication that the high frequency turbulence is being affected differently by each nozzle.

Overall it is clear that the turbulence statistics evolve very differently for each nozzle. The effects on the different turbulent scales vary from nozzle to nozzle and while one nozzle may increase length scales at a certain frequency another may decrease them. While tip and trough region length scales are most different closest to the nozzles these differences often still persists at the end of the potential core. It is likely that these significant changes to the turbulence statistics also have strong effects on the noise sources. The clear and meaningful insight given by these frequency dependent statistics into the multi-scale nature of turbulence is a significant validation of the technique as a tool for understanding turbulence. New complex nozzle geometries provide challenges to both experimental and numerical researchers and the insights provided by new experimental techniques can be of great benefit to all. It is important that this type of information is included in any aeroacoustic prediction code that wishes to capture the physics of the noise source mechanisms accurately.

Recent work by Morris and Zaman [37] has also investigated the frequency dependence of the length scales and indicated that the statistical properties of turbulence are independent of Mach number in the regions of highest turbulence intensity. While this supports the use of existing statistical models in these key noise producing regions this investigation has highlighted that the addition of chevrons to a nozzle can strongly affect how quickly the turbulence evolves to this structure. The use of the local Strouhal number in this investigation provided some evidence that the turbulence can be non-dimensionalised to a common form but only after the differences that exist in the potential core region have decayed. The key question for CAA predictions will now be if it is important to take account of these differences that exist in the initial region of the jet or if it is possible to significantly improve results with just the inclusion of a common form of frequency dependence found in the regions further downstream. The use of simple Gaussian and sine wave fits to the frequency dependent statistics used in this investigation should readily allow their inclusion in CAA codes which can then begin to compare these new predictions to experimental data for far field sound and thus provide some insight to these questions.

Chapter 8

Implications for Noise Source Modeling

This investigation has quantified how the addition of chevrons to a nozzle affects the characteristics of a turbulent jet. These changes include effects on the shear layer thickness, potential core length, turbulence intensities and two point statistics of the turbulence fluctuations. How these quantities are further affected by the immersion of chevrons into the flow has also been quantified. What follows is a brief discussion of the principle results from chapters 6 and 7 that are most pertinent for noise production. In addition comparisons will be drawn with the sound field results attained during the NASA Glenn tests specifically those of Bridges and Brown [28]. Their work comprised of several different parametric studies focusing on flow field and far field sound results. In particular one of these parametric studies which is most comparable to this work focused on chevron penetration using nozzles with 6 chevrons of length 22.6mm and penetration angles of 0° , 2.5° and 8.3° as summarized in table 8.1. The nozzle parameters have been modified from the original paper to match the definitions of nozzle diameter and penetration angle used in this work.

During this investigation the 0° nozzle significantly altered the development of turbulence in the jet. The shear layer thickness of the trough region of this nozzle $0.5D$ downstream of the nozzle exit was 100% larger than the baseline nozzle. The turbulence intensity in the initial shear layer was also significantly higher than the

Nozzle ID	Chevron Count	Chevron Length	Penetration Angle	Penetration	Diameter
SJ	0				50mm
N0	8	30mm	0°	0.0mm	50mm
N2	8	30mm	2°	1.0mm	50mm
N4	8	30mm	4°	2.1mm	50mm
SMC000	0				50.8mm
SMC005	6	22.6mm	0°	-0.005mm	52.8mm
SMC001	6	22.6mm	2.5°	0.985mm	52.8mm
SMC006	6	22.6mm	8.3°	3.525mm	52.8mm

Table 8.1: Nozzle Parameters

baseline nozzle. The v' turbulence was most strongly affected with an increase of approximately 80% over the baseline value $1D$ downstream of the nozzle exit. Beyond the initial region of the jet this nozzle showed the smallest reduction in potential core length, only 6%, and turbulence intensities were equal to the baseline levels by the end of the potential core. It is perhaps surprising that the nozzle with the most significant effects on the initial development of the turbulence is also closest to the baseline further down stream. Furthermore both the traditional and frequency dependent fixed and moving axis length scales show a significant increase over the baseline that persists beyond the potential core. The u' length scales had the largest increase for high frequencies while the v' length scales had the largest increase for low frequencies. Despite these strong effects for the 0° nozzle in this investigation the NASA tests showed that the sound field for their 0° nozzle was not significantly altered from the baseline. A explanation for this may be that the beneficial effects of chevron nozzles on far field sound are linked to the creation of counter rotating vortices formed about the chevron tips which increase mixing and effect the important sound producing regions of the jet. The strength of these vortices increases with chevron penetration so while a clear increase in mixing occurs near the nozzle exit for the 0° nozzle these vortices may quickly die out before reaching the important sound producing regions of the jet.

The 2° and 4° nozzles demonstrated that the effects of chevrons are strongly dependent on their immersion into the flow. The 2° nozzle had the strongest effect on the potential core producing a 22% reduction in length. However the changes to the

shear layer and ratio of the turbulence components were the smallest changes observed for the chevron nozzles. The tip and trough regions of this nozzle appeared to work together to produce the strong change on the jet structure. This is supported by the fact that both regions had very similar profiles for the turbulence properties. The significant reduction in the potential core length will strongly effect the location of sources for CAA predictions of chevron nozzles. The substantial increases observed for the length scales of the 0° nozzle are not seen for this nozzle. The frequency dependent length scales are generally very close to the baseline values at $50\%L_c$. The important changes from the baseline are observed at the end of the potential core where the large scales of the turbulence often have significantly decreased length scales. This reduction is also visible in the traditional statistics but this nozzle also increases the length scales at high frequencies and this is hidden in the traditional statistics. This demonstrates that not only does chevron immersion strongly affect the structure of the jet but also dramatically changes the length scales. The NASA chevron nozzles which penetrated into the flow produced low frequency noise reductions with a high frequency penalty. The high frequency penalty was prehaps associated with new sources near the nozzle exit since this high frequency penalty was most prominent at 90° . The decrease in the low frequency length scales observed at the end of the potential core may be the source of the low frequency noise reductions achieved for this nozzle type and the increased high frequency length scales may also be a contributing factor to the high frequency noise penalty. The design challenge is optimise this penetration angle to achieve the most beneficial noise reduction. While it is difficult to say with certainty which of the chevron nozzles used in this investigation would be most effective for noise reduction without having far field sound data there were some important differnces between the 2° and 4° chevron nozzles.

The 4° nozzle showed the largest differences between the tip and trough regions. There is also evidence to suggest that these two regions are having separate effects on the flow. The tip region of this nozzle produced only a slight increase in shear layer thickness and this growth was inward to the potential core region. In contrast the trough region significantly widened the shear layer outwards to the surrounding medium. This may be evidence that it is the tip region that produced the shorter

potential core seen for this nozzle. The trough region was shown to significantly alter the ratio of the turbulence properties and increase the v' turbulence. As a result this nozzle exhibits features found in both of the other nozzles. The fact that the two regions are having different, and perhaps countering, effects on the turbulence may explain why the length scales of this nozzle are closest to the baseline values. Despite having the lowest magnitude changes from the baseline this nozzle also had the widest variety of effects. For example it was the only nozzle to exhibit decreased high frequency length scales. A possible explanation for this is that the mechanisms involved change once both the front and back surfaces of the chevrons penetrate into the flow. The NASA tests showed that their nozzle with the aggressive penetration angle of 8.3° still achieved low frequency noise reductions but the high frequency penalty was also more significant. This investigation has highlighted the differences that exist between the tip and trough regions of a chevron nozzle and it has also shown that the mechanisms associated with chevrons become increasingly complex when they are significantly immersed into the flow.

Considering that many industrial jet noise predictions are based on statistically modeled turbulence superimposed on a $2D$ axisymmetric RANS calculation these results have several important implications. This investigation has highlighted that the differences in turbulence properties between the tip and trough regions of a chevron nozzle are both significant and persistent over the potential core length. While in principle it may be possible to superimpose these changes onto a $2D$ RANS calculation such a procedure is questionable at best. A fully empirical $3D$ model may now be more sensible for any researcher wishing to perform a fast rough-and-ready noise calculation rather than superimposing turbulence on a steady $2D$ calculation.

As outlined in chapter 2 the turbulence length scale is required for the major noise prediction theories. The majority of researchers use local average values of the length scale with these models. Through use of the frequency dependent length scales this investigation has clearly shown that the different scales of the turbulence respond very differently to the addition of chevrons to a nozzle. A comparison of the frequency dependent length scales with the traditional length scales has revealed that the traditional length scales are often dominated by the larger turbulent scales.

This evidence that the traditional length scales are dominated by the larger turbulence structures may have significant implications for the Tam-Auriault model which is based on fine scale turbulence noise. If the changes to the fine scale turbulence are hidden by the large structures of the flow it may be particularly important to include frequency dependent length scales in these models. Without the use of a frequency dependent length scale no model is capable of capturing all of the changes produced by chevrons. Any model wishing to capture the physics of the noise production must include a frequency dependent length and time scale.

8.1 Future Work

The results of this investigation can be used to direct further experimental and numerical research. In terms of further experimental research:

- The correlation of changes in turbulent statistics with far field sound may shed further insight on how these changes achieve the noise reduction. Such an investigation could directly correlate a decrease in noise at a particular frequency to the change in the associated length and time scales.
- An investigation of the effects of chevrons on radial and azimuthal length scales. The results of this investigation clearly show how chevrons alter the ratio of the u' to v' turbulence intensities and their axial length scales. Similar important changes are likely to occur for the radial and azimuthal length scales.
- Further investigation of the frequency dependent convection speeds and time scales may also be necessary to capture all of the information required to improve jet noise models.
- The application of similar analysis techniques to microjets. Microjets are a technology which provide similar noise reduction abilities to chevrons and studies have shown that the combination of these technologies can lead to further reductions. There has been little research into how the mechanisms for the two technologies are related or how their combination provides further benefits.

In terms of numerical research:

- The capturing of altered frequency dependent length and times scales by a LES or DNS simulation would be a clear indication that CFD codes can handle the new physics of chevrons.
- The implementation of a new frequency dependent correlation tensor in a noise source model would hopefully capture the noise reduction abilities of chevrons more accurately.
- A comparison of the improved prediction methodology with far field sound measurements would demonstrate if the inclusion of frequency dependence in turbulence models is enough to capture the effects of chevrons on the far field sound or if further work is required to improve the models.

Bibliography

- [1] F. Calkins and G. Butler. Variable geometry chevrons for jet noise reduction. In *12th AIAA/CEAS Aeroacoustics Conference Proceedings*, Cambridge, Massachusetts, 2006.
- [2] R. H. Self. Jet noise prediction using the lighthill acoustic analogy. *Journal of Sound and Vibration*, 275(3-5):757–768, 2004.
- [3] G. K. Batchelor. *The Theory of Homogeneous Turbulence*. Cambridge Science Classics, 1953.
- [4] D. J. J. Leclercq and X. Bohineust. Investigation and modelling of the wall pressure field beneath a turbulent boundary layer at low and medium frequencies. *Journal of Sound and Vibration*, 257(3):477–501, 2002.
- [5] M. J. Lighthill. The bakerian lecture 1961 sound generated aerodynamically. *Proceedings of the Royal Society of London Series A, Mathematical and Physical Sciences*, 267(1329):147–182, 1962.
- [6] M. Billson. Computational techniques for turbulence generated noise. *Ph. D. Thesis, Division of Thermo and Fluid Dynamics, Chalmers University of Technology*, 2004.
- [7] A. Uzun and M. Y. Hussaini. Simulation of noise generation in near-nozzle region of a chevron nozzle jet. In *13th AIAA/CEAS Aeroacoustics Conference Proceedings*, Rome, Italy, 2007.

- [8] M. J. Lighthill. On sound generated aerodynamically .1. general theory. *Proceedings of the Royal Society of London Series A, Mathematical and Physical Sciences*, 211(1107):564–587, 1952.
- [9] M. J. Lighthill. On sound generated aerodynamically .2. turbulence as a source of sound. *Proceedings of the Royal Society of London Series A, Mathematical and Physical Sciences*, 222(1148):1–32, 1954.
- [10] Herbert S. Ribner. Effects of jet flow on jet noise via an extension to the lighthill model. *Journal of Fluid Mechanics Digital Archive*, 321(-1):1–24, 1996.
- [11] C. K. W. Tam and L. Auriault. Jet noise from fine-scale turbulence. *AIAA Journal*, 37(2):145–153, 1999.
- [12] D. Juv, M. Sunyach, and G. Comte-Bellot. Intermittency of the noise emission in subsonic cold jets. *Journal of Sound and Vibration*, 71(3):319–332, 1980.
- [13] M. Schaffar. Direct measurements of the correlation between axial in-jet velocity fluctuations and far field noise near the axis of a cold jet. *Journal of Sound and Vibration*, 64(1):73–83, 1979.
- [14] M. Schaffar and J. P. Hancy. Investigation of the noise emitting zones of a cold jet via causality correlations. *Journal of Sound and Vibration*, 81(3):377–391, 1982.
- [15] J. Panda and R. G. Seasholtz. Experimental investigation of density fluctuations in high-speed jets and correlation with generated noise. *Journal of Fluid Mechanics*, 450:97–130, 2002.
- [16] P. Jordan, J. A. Fitzpatrick, and C. Meskell. Beampattern control of a microphone array to minimize secondary source contamination. *Journal of the Acoustical Society of America*, 114(4):1920–1925, 2003.
- [17] H. A. Siller, F. Arnold, and U. Michel. Investigation of aero-engine core-noise using a phased microphone array. In *7th AIAA/CEAS Aeroacoustics Conference Proceedings*, Maastricht, Netherlands, 2001.

- [18] C. K. W. Tam and L. Auriault. Mean flow refraction effects on sound radiated from localized sources in a jet. *Journal of Fluid Mechanics*, 370:149–174, 1998.
- [19] J. Ffocs Williams. The noise from turbulence convected at high speed. *Philosophical Transactions of the Royal Society of London Series A, Mathematical and Physical Sciences*, 255(1061), 1963.
- [20] A. A. Townsend. *The Structure of Turbulent Shear Flow*. Cambridge University Press, second edition, 1976.
- [21] F. Kerherve, J. Fitzpatrick, and P. Jordan. The frequency dependence of jet turbulence for noise source modelling. *Journal of Sound and Vibration*, 296(1-2):209–225, 2006.
- [22] C. Gerhold, M. Brown, M. Jones, D. Nark, and B. Howerton. Configuration effects on acoustic performance of a duct liner. In *14th AIAA/CEAS Aeroacoustics Conference*, Vancouver, British Columbia Canada, 2008.
- [23] R. Mani, J. Luedke, and M. Jones. Improved inlet noise attenuation by alteration of boundary layer profiles. *National Aeronautics and Space Administration Technical Report, NASA Langley Research Center*, 2004.
- [24] M. Bahadir Alkisar and G. Butler. Significant improvements on jet noise reduction by chevron-microjet combination. In *13th AIAA/CEAS Aeroacoustics Conference Proceedings*, Rome, Italy, 2007.
- [25] V. Mengle, G. Dalton, J. Bridges, and K. Boyd. Noise reduction with lobed mixers nozzle-length and free-jet speed effects. *National Aeronautics and Space Administration Technical Report, NASA Glenn Research Centre*, 1997.
- [26] N. Saiyed, K. Mikkelsen, and J. Bridges. Acoustics and trust of separate-flow exhaust nozzles with mixing devices for high-bypass-ratio engines. *National Aeronautics and Space Administration Technical Report, NASA Glenn Research Centre*, 2000.

- [27] J. Bridges. Measurements of turbulent flow field in separate flow nozzles with enhanced mixing devices-test report. *National Aeronautics and Space Administration Technical Report, NASA Glenn Research Centre*, 2002.
- [28] J. Bridges and C. Brown. Parametric testing of chevrons on single flow hot jets. In *10th AIAA/CEAS Aeroacoustics Conference Proceedings*, Manchester, United Kingdom, 2004.
- [29] E. Nesbitt, V. Mingle, M. Czech, B. Callander, and R. Thomas. Flight test results for uniquely tailored propulsion-airframe aeroacoustic chevrons: Community noise. In *12th AIAA/CEAS Aeroacoustics Conference Proceedings*, Cambridge, Massachusetts, 2006.
- [30] M. Mihaescu, C. Harris, E. Gutmark, and L. Fuchs. Flow and acoustics characteristics of chevron nozzles in coaxial jets - les acoustic analogy investigation. In *13th AIAA/CEAS Aeroacoustics Conference Proceedings*, Rome, Italy, 2007.
- [31] L. Chatellier and J. Fitzpatrick. Spatio-temporal correlation analysis of turbulent flows using global and single-point measurements. *Experiments in Fluids*, 38(5):563–575, 2005.
- [32] M. Raffel, C. Willert, S. Wereley, and J. Kompenhans. *Particle Image Velocimetry A Practical Guide*. Springer, New York, second edition, 2007.
- [33] J. Westerweel. Efficient detection of spurious vectors in particle image velocimetry data. *Experiments in Fluids*, 16:236–247, 1994.
- [34] L. H. Benedict and H. Nobach. Estimation of turbulent velocity spectra from laser doppler data. *Measurement Science Technology*, 11:1089–1104, 2000.
- [35] L. Simon and J. Fitzpatrick. An improved sample-and-hold reconstruction procedure for estimation of power spectra from lda data. *Experiments in Fluids*, 37(2):272–280, 2004.

- [36] J. Fitzpatrick and L. Simon. Estimation of cross-power spectra using sample-and-hold reconstruction of laser doppler anemometry data. *Experiments in Fluids*, 39(6):954–965, 2005.
- [37] Philip J. Morris and K. B. M. Q. Zaman. Velocity measurements in jets with application to noise source modeling. *Journal of Sound and Vibration*, 329(4):394–414, 2010.

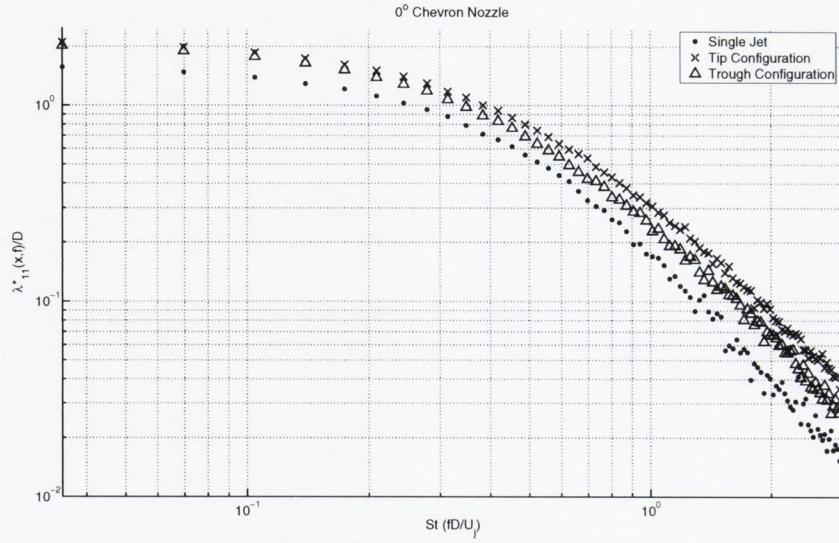
BIBLIOGRAPHY

Appendix A

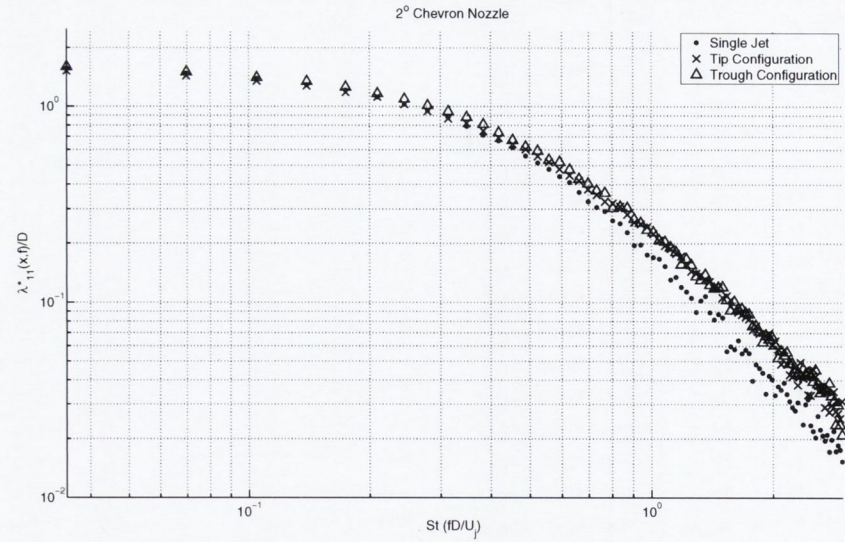
Frequency Dependent Length

Scales $75\%L_c$

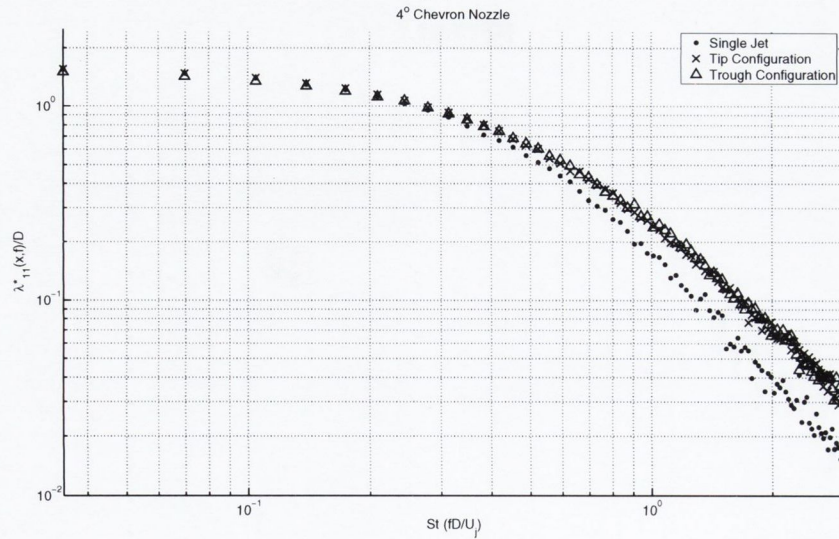
Presented here are the frequency dependent fixed and moving axis length scales for the $75\%L_c$ measurement positions.



(a)



(b)

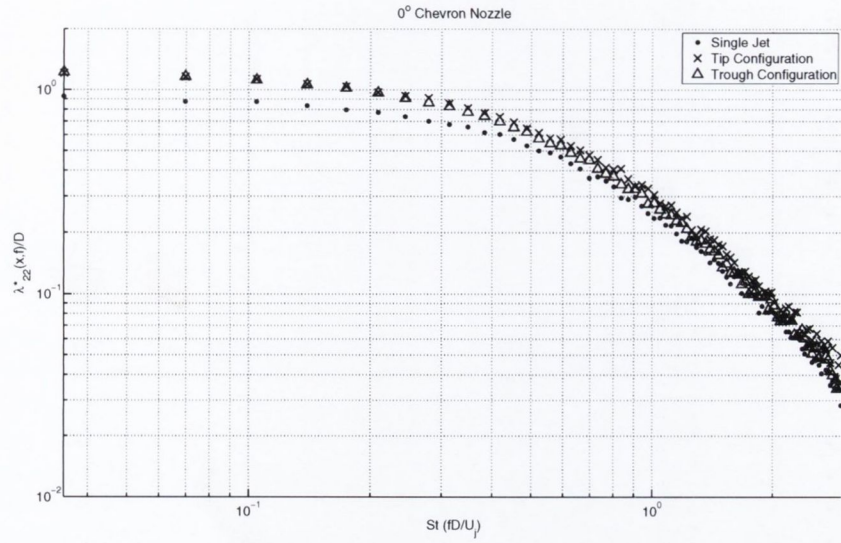


(c)

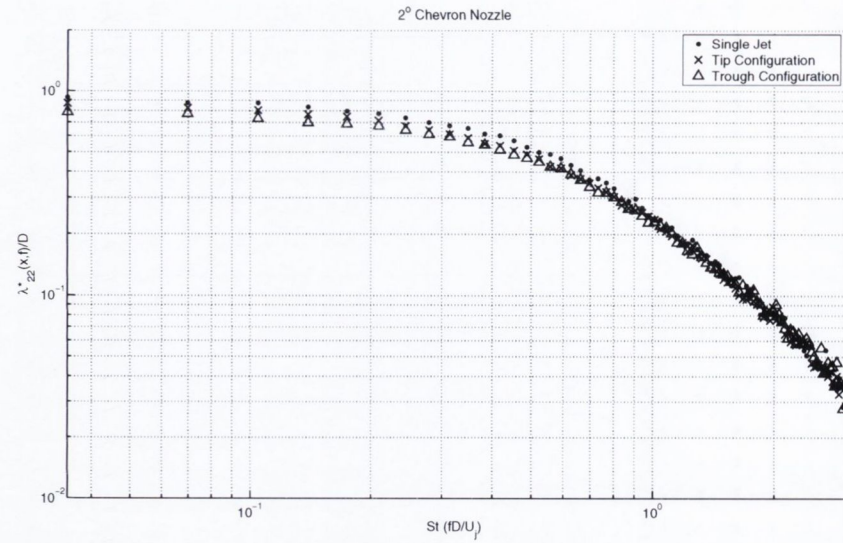
0.75 LC	LC	Fixed Axis (mm)	Moving Axis (mm)	Convection Speed (m/s)
SJ	4.92D	10.60	37.53	40.48
N0 Tip	4.64D	12.48	47.41	42.84
N0 Trough	4.64D	13.12	48.12	40.74
N2 Tip	3.80D	10.90	38.49	40.15
N2 Trough	4.64D	9.74	35.91	38.53
N4 Tip	4.13D	10.96	39.46	39.44
N4 Trough	4.64D	9.84	35.95	38.90

(d)

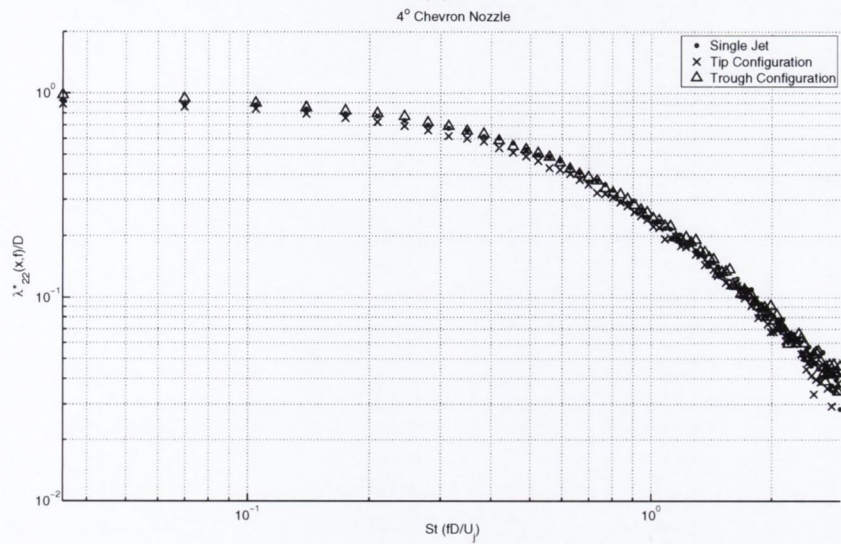
Figure A.1: Frequency Dependent Moving Axis Length Scale $u' 75\%L_c$



(a)



(b)

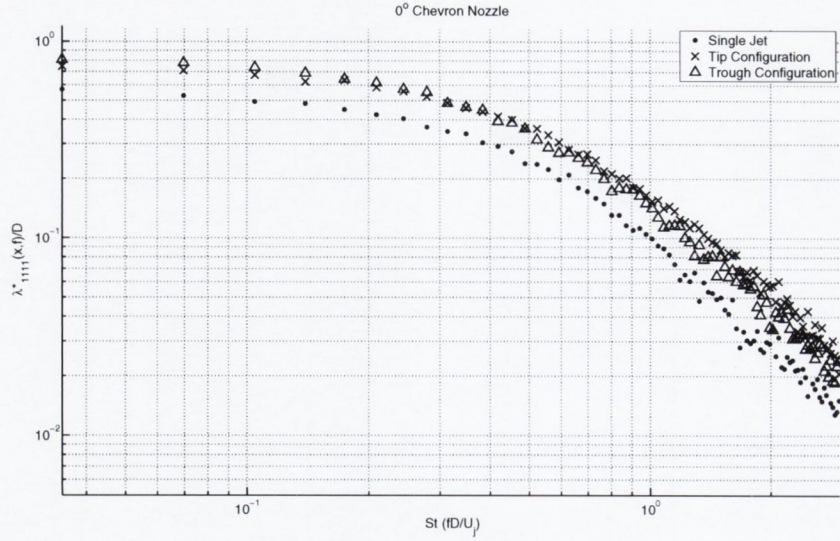


(c)

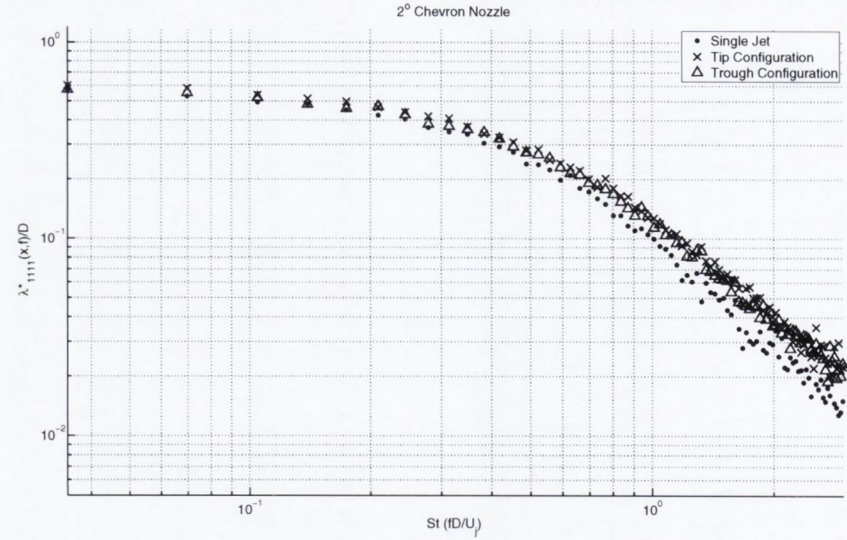
0.75 LC	LC	Fixed Axis (mm)	Moving Axis (mm)	Convection Speed (m/s)
SJ	4.92D	5.82	23.22	43.69
N0 Tip	4.64D	6.91	27.85	44.81
N0 Trough	4.64D	6.92	26.28	43.14
N2 Tip	3.80D	5.28	19.96	41.81
N2 Trough	4.64D	5.13	18.56	41.67
N4 Tip	4.13D	5.88	23.05	37.81
N4 Trough	4.64D	5.43	22.85	39.10

(d)

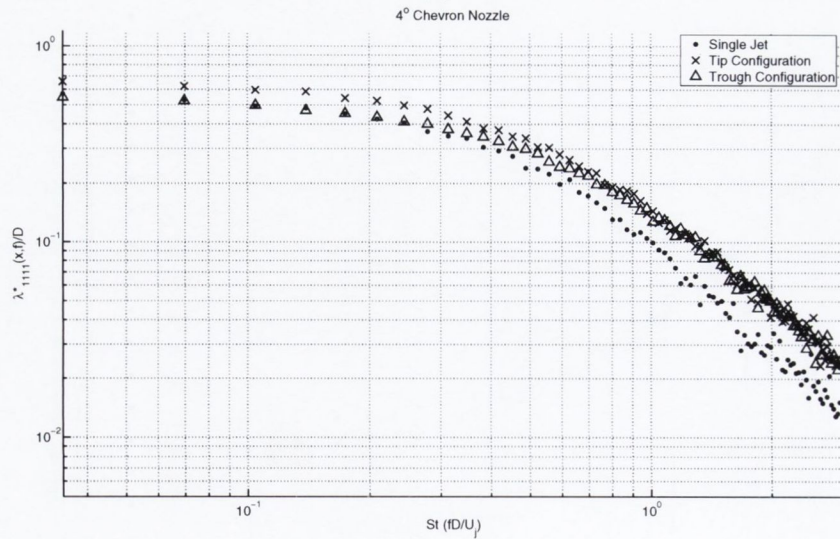
Figure A.2: Frequency Dependent Moving Axis Length Scale $v' 75\%L_c$



(a)



(b)

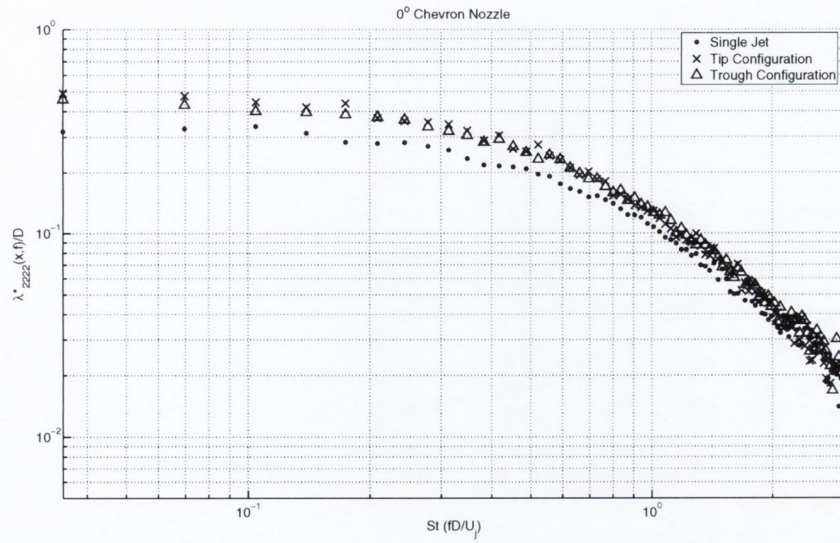


(c)

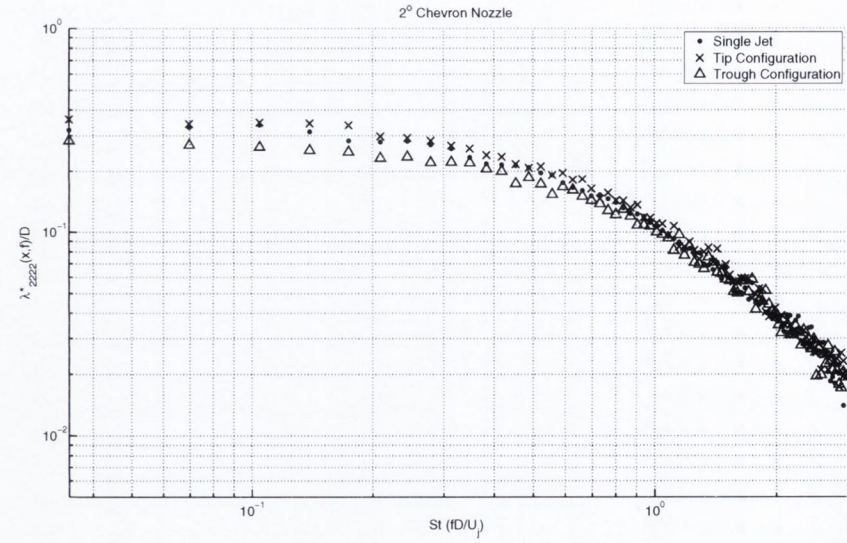
0.75 LC	LC	Fixed Axis (mm)	Moving Axis (mm)	Convection Speed (m/s)
SJ	4.92D	5.23	13.36	49.92
N0 Tip	4.64D	5.80	17.02	40.34
N0 Trough	4.64D	6.01	16.85	47.05
N2 Tip	3.80D	4.97	13.77	41.84
N2 Trough	4.64D	4.67	12.58	31.81
N4 Tip	4.13D	5.04	14.62	36.52
N4 Trough	4.64D	4.67	13.39	34.55

(d)

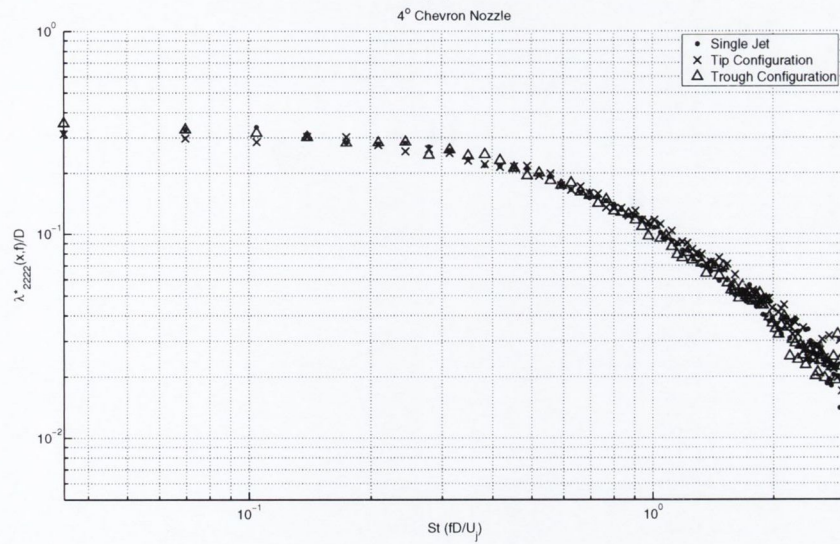
Figure A.3: Frequency Dependent Moving Axis Length Scale u^2 75% L_c



(a)



(b)

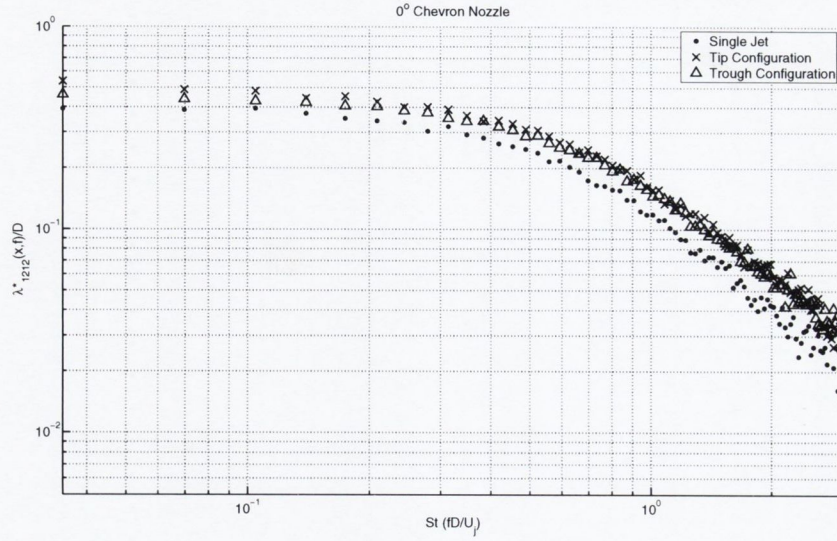


(c)

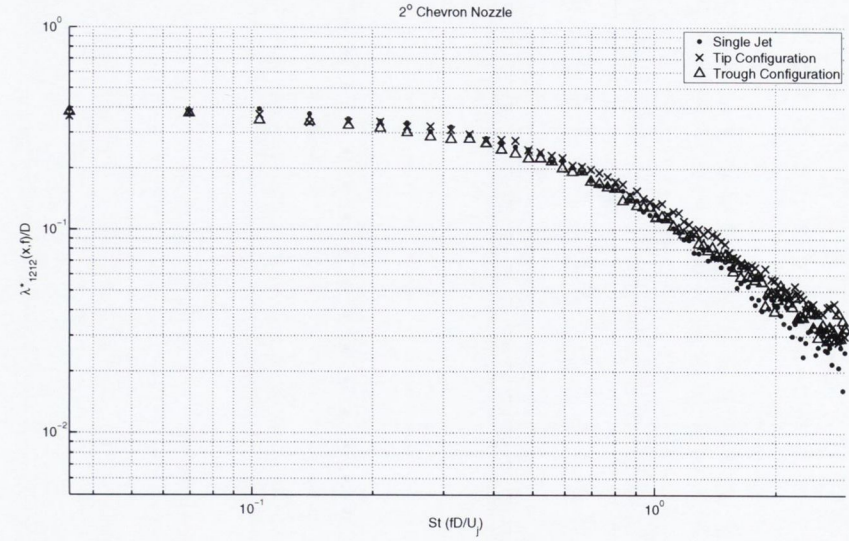
0.75 LC	LC	Fixed Axis (mm)	Axis	Moving Axis (mm)	Convection Speed (m/s)
SJ	4.92D	3.47		8.09	53.34
N0 Tip	4.64D	3.92		10.00	53.17
N0 Trough	4.64D	4.20		10.18	54.99
N2 Tip	3.80D	3.14		8.32	47.16
N2 Trough	4.64D	2.99		7.11	56.16
N4 Tip	4.13D	3.43		8.47	45.84
N4 Trough	4.64D	3.03		7.99	51.84

(d)

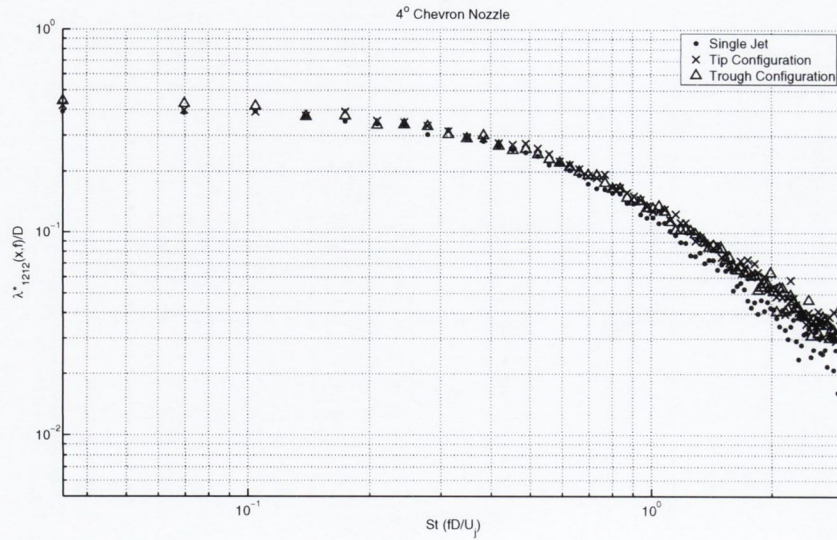
Figure A.4: Frequency Dependent Moving Axis Length Scale $v'^2 75\%L_c$



(a)



(b)

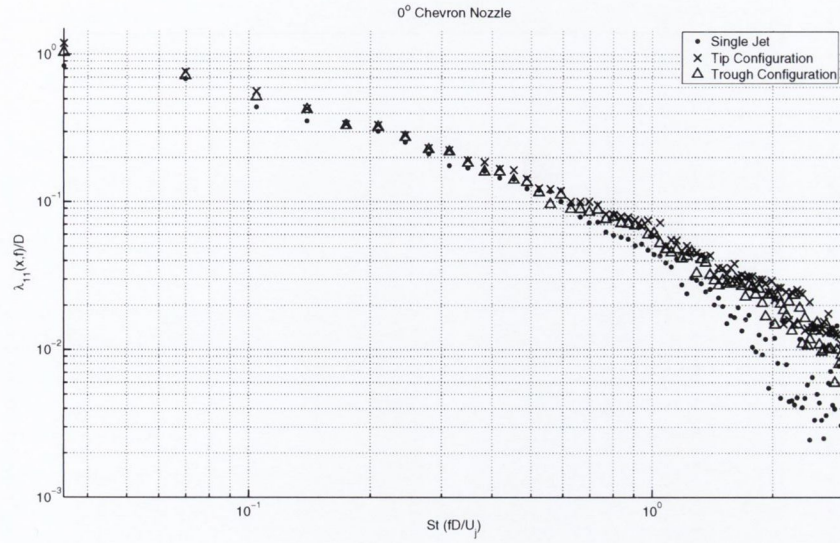


(c)

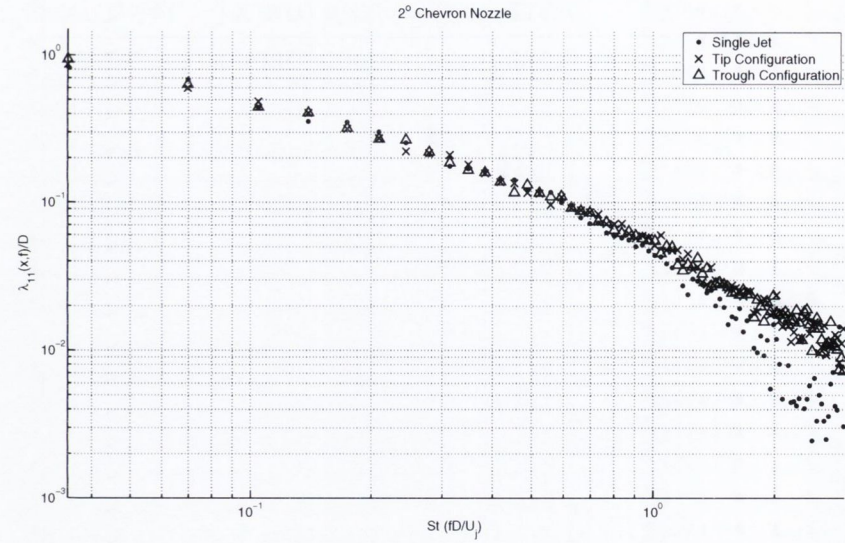
0.75 LC	LC	Fixed Axis (mm)	Moving Axis (mm)	Convection Speed (m/s)
SJ	4.92D	3.50	9.83	48.06
N0 Tip	4.64D	3.91	11.77	49.22
N0 Trough	4.64D	4.08	11.88	46.94
N2 Tip	3.80D	3.27	9.65	47.15
N2 Trough	4.64D	3.22	8.99	48.03
N4 Tip	4.13D	3.60	10.46	46.46
N4 Trough	4.64D	3.38	9.65	46.31

(d)

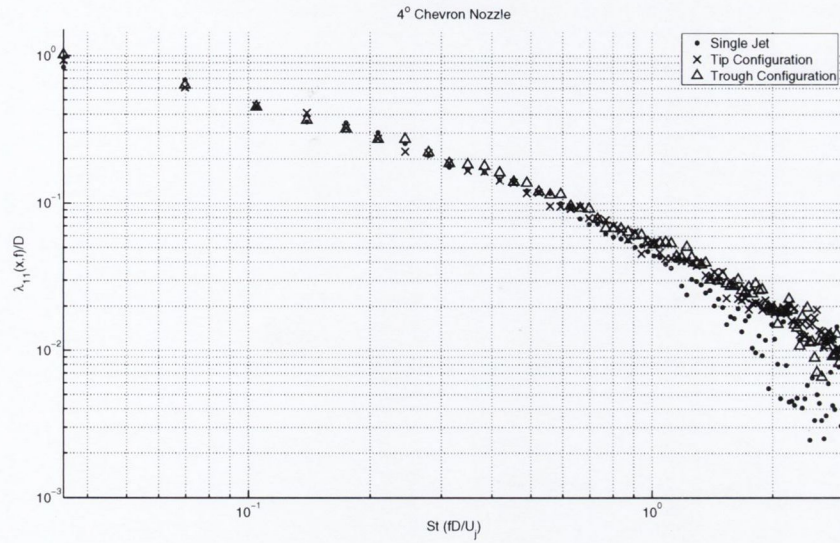
Figure A.5: Frequency Dependent Moving Axis Length Scale $u'v'$ 75% L_c



(a)



(b)

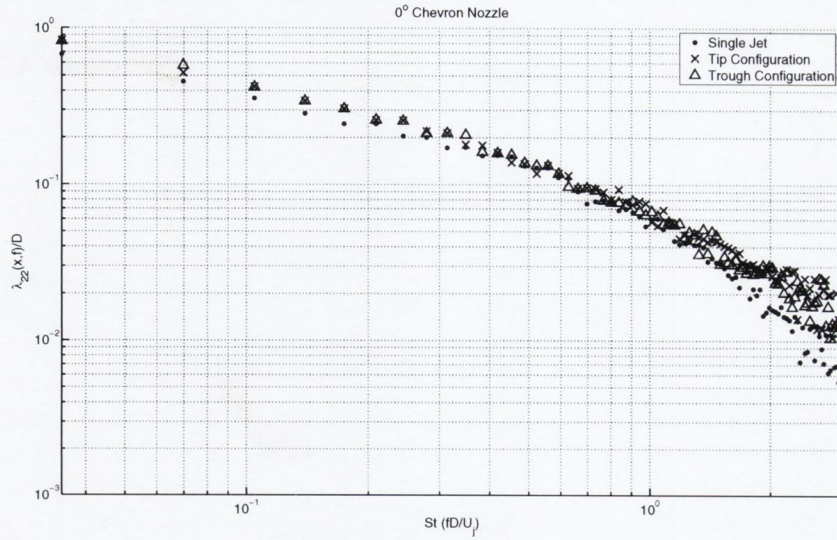


(c)

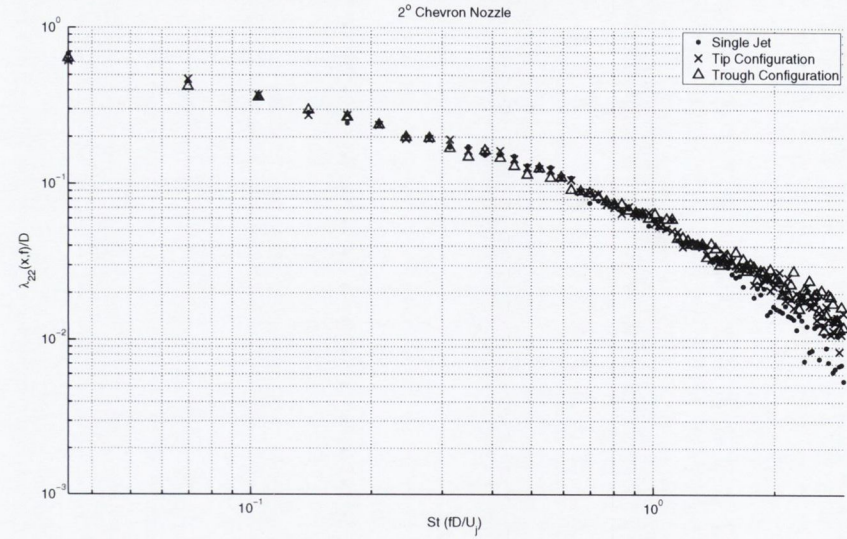
0.75 LC	LC	Fixed Axis (mm)	Moving Axis (mm)	Convection Speed (m/s)
SJ	4.92D	10.60	37.53	40.48
N0 Tip	4.64D	12.48	47.41	42.84
N0 Trough	4.64D	13.12	48.12	40.74
N2 Tip	3.80D	10.90	38.49	40.15
N2 Trough	4.64D	9.74	35.91	38.53
N4 Tip	4.13D	10.96	39.46	39.44
N4 Trough	4.64D	9.84	35.95	38.90

(d)

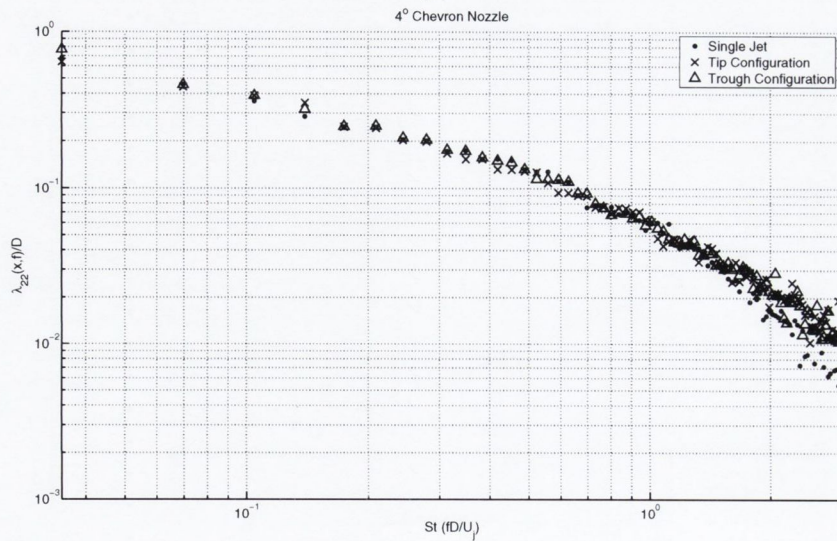
Figure A.6: Frequency Dependent Fixed Axis Length Scale $u' 75\%L_c$



(a)



(b)

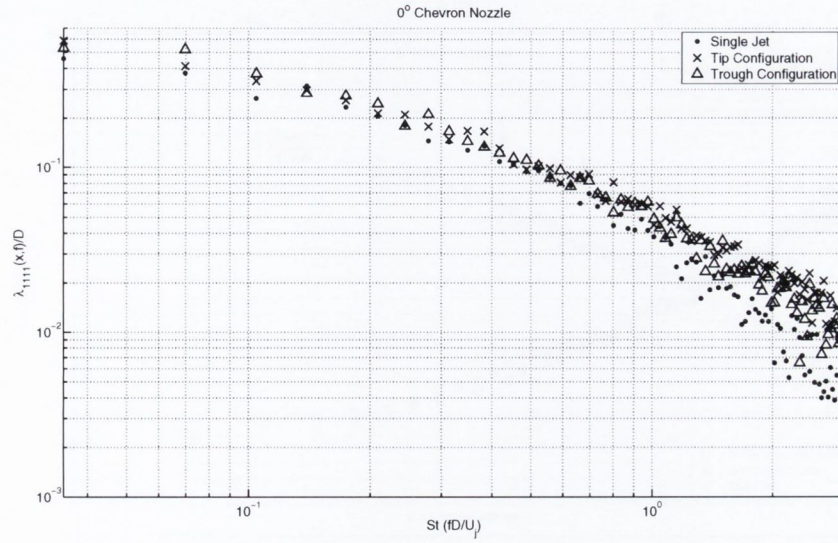


(c)

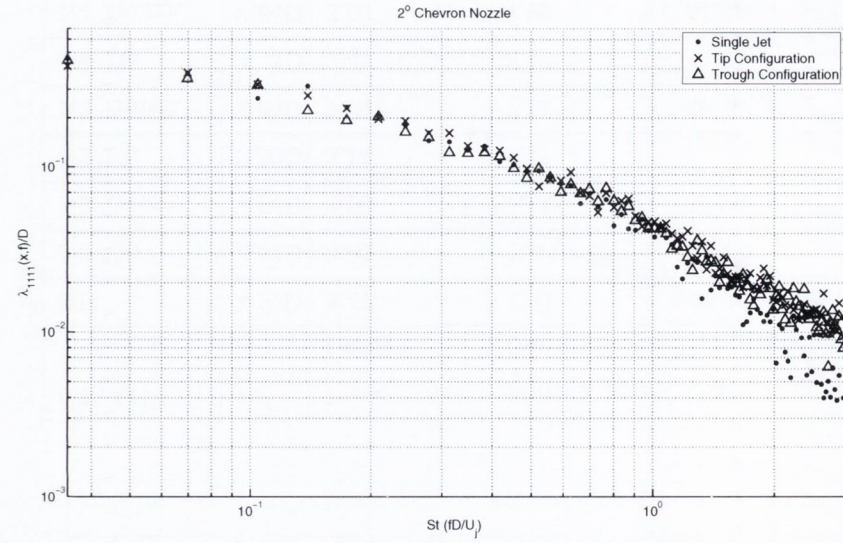
0.75 LC	LC	Fixed Axis (mm)	Moving Axis (mm)	Convection Speed (m/s)
SJ	4.92D	5.82	23.22	43.69
N0 Tip	4.64D	6.91	27.85	44.81
N0 Trough	4.64D	6.92	26.28	43.14
N2 Tip	3.80D	5.28	19.96	41.81
N2 Trough	4.64D	5.13	18.56	41.67
N4 Tip	4.13D	5.88	23.05	37.81
N4 Trough	4.64D	5.43	22.85	39.10

(d)

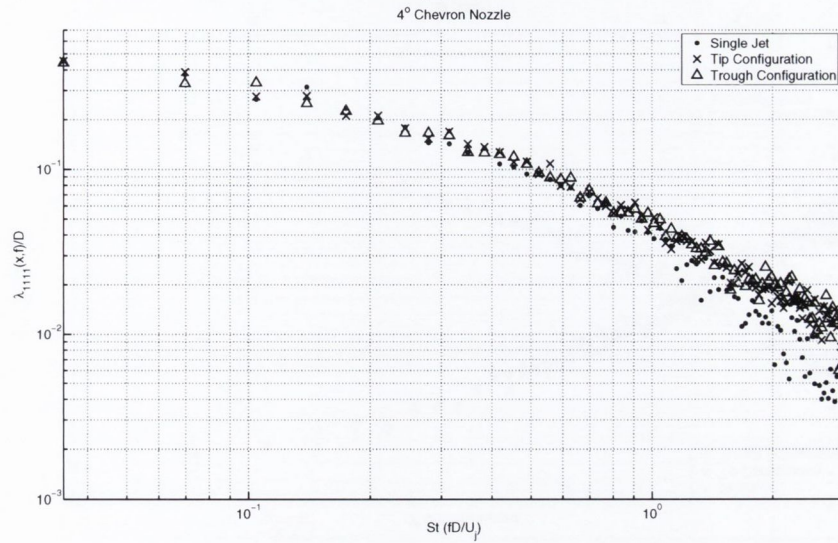
Figure A.7: Frequency Dependent Fixed Axis Length Scale $v' 75\%L_c$



(a)



(b)

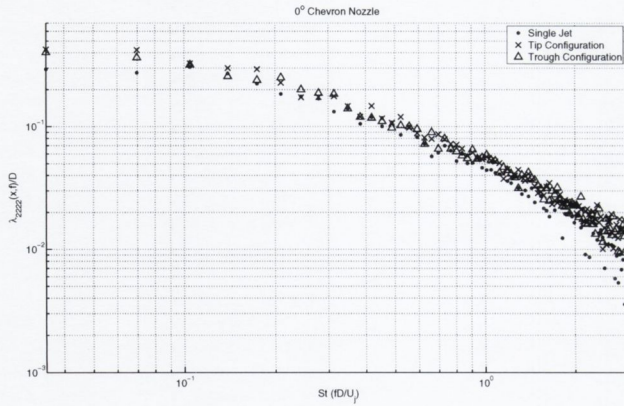


(c)

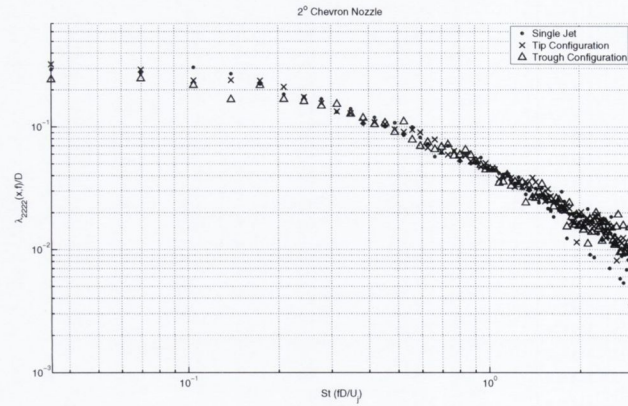
0.75 LC	LC	Fixed Axis (mm)	Moving Axis (mm)	Convection Speed (m/s)
SJ	4.92D	5.23	13.36	49.92
N0 Tip	4.64D	5.80	17.02	40.34
N0 Trough	4.64D	6.01	16.85	47.05
N2 Tip	3.80D	4.97	13.77	41.84
N2 Trough	4.64D	4.67	12.58	31.81
N4 Tip	4.13D	5.04	14.62	36.52
N4 Trough	4.64D	4.67	13.39	34.55

(d)

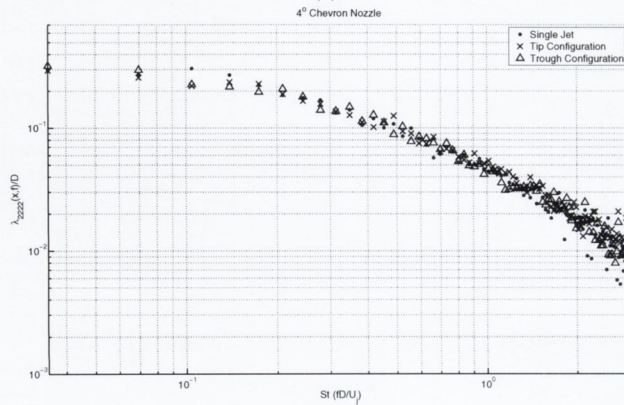
Figure A.8: Frequency Dependent Fixed Axis Length Scale $u'^2 75\%L_c$



(a)



(b)

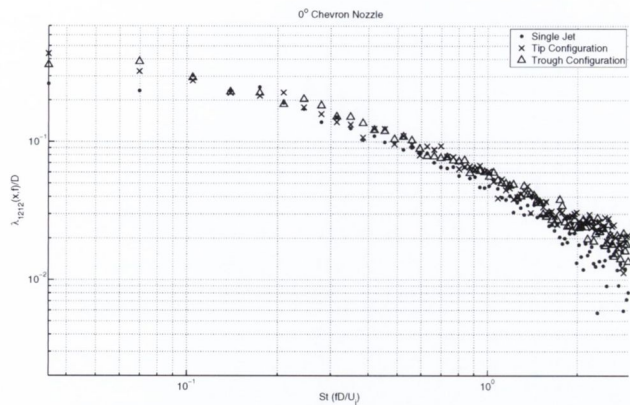


(c)

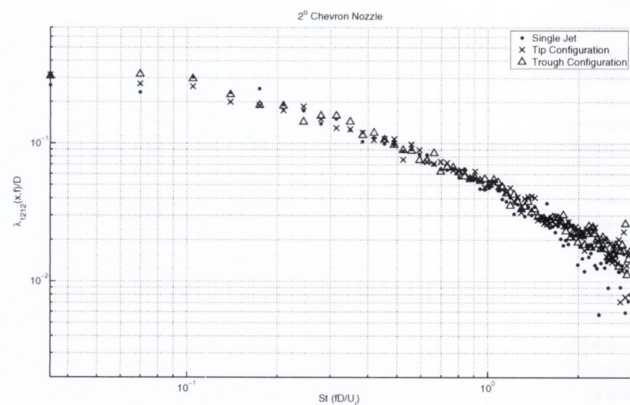
0.75 LC	LC	Fixed Axis (mm)	Moving Axis (mm)	Convection Speed (m/s)
SJ	4.92D	3.47	8.09	53.34
N0 Tip	4.64D	3.92	10.00	53.17
N0 Trough	4.64D	4.20	10.18	54.99
N2 Tip	3.80D	3.14	8.32	47.16
N2 Trough	4.64D	2.99	7.11	56.16
N4 Tip	4.13D	3.43	8.47	45.84
N4 Trough	4.64D	3.03	7.99	51.84

(d)

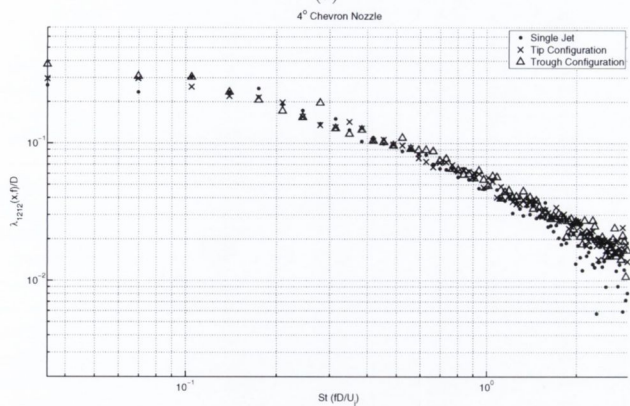
Figure A.9: Frequency Dependent Fixed Axis Length Scale $v'^2 75\%L_c$



(a)



(b)



(c)

0.75 LC	LC	Fixed Axis (mm)	Moving Axis (mm)	Convection Speed (m/s)
SJ	4.92D	3.50	9.83	48.06
N0 Tip	4.64D	3.91	11.77	49.22
N0 Trough	4.64D	4.08	11.88	46.94
N2 Tip	3.80D	3.27	9.65	47.15
N2 Trough	4.64D	3.22	8.99	48.03
N4 Tip	4.13D	3.60	10.46	46.46
N4 Trough	4.64D	3.38	9.65	46.31

(d)

Figure A.10: Frequency Dependent Fixed Axis Length Scale $u'v' 75\%L_c$

